A Precision Measurement of the Weak Mixing Angle in Møller Scattering at Low Q^2

Thesis by

G. Mark Jones

In Partial Fulfillment of the Requirements

for the Degree of

Doctor of Philosophy

California Institute of Technology

Pasadena, California

2004

(Defended May 19, 2004)

Acknowledgements

I am greatly indebted to many people that have provided support, encouragement, insight, and guidance to me over the course of the work presented in this thesis. I would like first to thank my advisor, Emlyn Hughes, for allowing me the opportunity to be a part of his group at Caltech. I was afforded the chance to receive an excellent education in the classroom and in the laboratory, and for that I am truly grateful.

The success of the challenging E158 experiment is due to the many diverse contributions of the collaborators. To each of them I owe a great deal of thanks. In particular, I would like to acknowledge Krishna Kumar, Paul Souder and my advisor for their able leadership at SLAC. Their immense physical insight and experience were crucial to the experiment. I am also grateful for the tireless efforts of Yury Kolomensky and Michael Woods. Without their keen ability, the experiment could not have succeeded. Also, both Yury and Mike were patient teachers, a trait greatly appreciated by the students on the experiment. I am thankful that I got to know Raymond Arnold, who reminded me in the midst of all the chaos of the experiment that I shouldn't forget that the study of physics is an interesting and worthwhile endeavor. Also, I would like to acknowledge Michael Olson "MO" for being an excellent run coordinator and teaching me the importance of the National Football League and the Packers. I am thankful to Zenon Szalata for all the assistance he gave me, especially on those owl shifts where I would inevitiably have to call him at his home for

advice. I would also like to acknowledge John Weisend who did a superb job with the liquid hydrogen target, and who also taught me how to remain calm in the midst of warning bells and flashing lights. I would like to thank Dieter Walz, whose unbounded knowledge about the workings of the laboratory and his interesting tales made many a shift go by quickly.

The construction of the apparatus in End Station A within the time constraints of the experiment proved to be a truly formidable undertaking. I am grateful for the diligent work of Ken Baird that saw the experiment go from an idea on paper to existing in the real world. I would also like to thank Michael Racine and Carl Hudspeth, as well as the rest of the craftsmen who built the experiment, whose skill and expertise in all manners of construction allowed the apparatus to function as designed.

I owe many thanks to my fellow students and the post-docs, who worked with me on the data analysis, and also helped in taking all those shifts. In particular, I want to thank Carlos Arroyo, Klejda Bega, Mark Cooke, Waled Emam, Brian Humensky, Lisa Kaufman, Peter Mastromarino, Kent Paschke, Jaideep Singh, Baris Tonguc, Brock Tweedie, Imran Younus, and Antonin Vacheret. We went through a lot together, and I feel privileged to have worked with each of them.

I am truly grateful for having been able to work with Clive Field on the luminosity monitor. I was always in awe of the combination of his sharp mind and his immense technical ability. He taught me how to systematically approach problems, and he showed me new ways of thinking about things. I would also like to acknowledge the contribution of Gholamali Mazaheri, who worked diligently on the electronics side of the detector.

I was fortunate to also work with many interesting people during my time at Caltech. David Pripstein introduced me to the work in the lab, and he also helped me adjust to life in graduate school in general. His outgoing personality and his taste for fine wines made

my first year at Caltech memorable and enjoyable. It is no exaggeration to say that my interactions with Dave as an undergraduate led me to choose Caltech for graduate school. For that, I am very thankful. Steffen Jensen and Jaideep Singh were always able to make working in the lab more enjoyable with their sense of humor. I want to thank Tina Pavlin for being a good listener and making sure I didn't focus too much on lab work. Also, many thanks to Georgia Frueh for skillfully managing all of the graduate students in our group with a smile.

My experiences at the University of Kentucky as an undergraduate greatly influenced my choice to pursue the study of physics. In particular, Wolfgang Korsch was a very positive influence on me. His love of physics, as well as his patient guidance, gave me great encouragement. The lessons he gave me in the classes he taught and at Jefferson lab proved to be invaluable in graduate school. I would also like to mention Valdis Zeps and Tim Gorringe, two excellent physics professors I had as an undergraduate. Their skillful instruction prepared me for the rigors of graduate school and instilled in me a desire to learn more. I would also like to thank Jian-ping Chen at Jefferson lab, who made my time there both enjoyable and enlightening.

I owe special thanks to my friends and family. Peter Mastromarino, with his sense of humor and genuine good nature, proved to be a true friend throughout graduate school. I feel very fortunate that we ended up on the same experiment together. I am thankful to Ted "Theodore" Corcovilos for his friendship, as well as helping me survive classwork at Caltech and teaching me to "chill." Sean Stave and Aaron Skaggs also provided me with much needed encouragement, probably more than they know. And finally, I would like to give thanks to my family, Gary, Linda, and Chris, to whom I literally owe everything. They have always given me unconditional support and encouragement. I hope they feel they are a

part of the work in this thesis, because I know that I could not have accomplished anything without them.

Abstract

The electroweak theory has been probed to a high level of precision at the mass scale of the Z^0 through the joint contributions of LEP at CERN and the SLC at SLAC. The E158 experiment at SLAC complements these results by measuring the weak mixing angle at a Q^2 of 0.026 $(\mathrm{GeV/c})^2$, far below the weak scale.

The experiment utilizes a 48 GeV longitudinally polarized electron beam on unpolarized atomic electrons in a target of liquid hydrogen to measure the parity-violating asymmetry A^{PV} in Møller scattering.

The tree-level prediction for A^{PV} is proportional to $1 - 4\sin^2\theta_W$. Since $\sin^2\theta_W \approx 0.25$, the effect of radiative corrections is enhanced, allowing the E158 experiment to probe for physics effects beyond the Standard Model at the TeV scale.

This work presents the results from the first two physics runs of the experiment, covering data collected in the year 2002. The parity-violating asymmetry A^{PV} was measured to be

$$A^{PV} = -158 \text{ ppb} \pm 21 \text{ ppb (stat)} \pm 17 \text{ ppb (sys)}. \quad (1)$$

The result represents the first demonstration of parity violation in Møller scattering. The observed value of A^{PV} corresponds to a measurement of the weak mixing angle of

$$\sin^2\theta_W^{eff} = 0.2380 \pm 0.0016 \text{ (stat)} \pm 0.0013 \text{ (sys)}, \quad (2)$$

which is in good agreement with the theoretical prediction of

$$\sin^2 \theta_W^{eff} = 0.2385 \pm 0.0006 \text{ (theory)}. \tag{3}$$

Contents

List of Figures

List of Tables

Chapter 1

Introduction

The E158 experiment is designed to be a precision low-energy test of the electroweak theory, complementing the substantial high-energy results obtained by the SLC and LEP colliders. This introductory chapter provides a background to the experiment by briefly tracing the evolution of the understanding of the weak force and its unification with the electromagnetic interaction in the framework of the Standard Model. In addition, the methodology and timeline of the E158 experiment are outlined.

1.1 Early Study of the Weak Force

The study of the weak force has its beginning in the year 1900 with the discovery of β radiation by Becquerel [1]. The process was understood as the decay of an atom in state X to another state X' through the emission of an electron e^-:

$$X \rightarrow X' + e^-. \tag{1.1}$$

The decay results in only two products, so conservation of energy dictates that all β decays should emit an electron with the same energy.

In 1914, Chadwick made the surprising discovery that the energy of the particles emitted

in β decay was not a single value, but a continuum [2]. To many scientists, the result indicated that β decays simply did not conserve energy. Pauli remedied the situation in 1930 by hypothesizing that there was another particle ν[1] emitted in β decay, along with the electron, carrying off the missing energy [3]:

$$X \rightarrow X' + e^- + \nu. \tag{1.2}$$

The particle had to be very light and weakly interacting to have avoided detection. It was clear that the ν particle could not interact electromagnetically but only through a new force, called the weak force.

Fermi dubbed the new particle the "neutrino" and in 1934 incorporated it into a successful theory describing β decay. Figure 1.1 depicts the diagram representing Fermi's model. The four particles of the decay interact at a single vertex, with a coupling strength denoted as G_F [4].

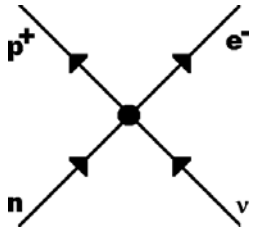

Figure 1.1: Fermi's four-point interaction for β decay.

In 1949, it was realized that G_F was identical for many different weak decay processes. This led Lee, Yang, and Rosenbluth to postulate that all weak interactions are mediated by a massive boson, named the W^- (or its anti-particle, the W^+) [5]. Figure 1.2 represents β decay with the introduction of the W^-. For energy scales below the mass of the W,

[1]Pauli actually named the new particle "neutron," but that name was taken in 1932 with Chadwick's discovery of the neutral partner to the proton in the nucleus. Also, the particle ν is actually called the anti-neutrino $\overline{\nu}$ today.

the process depicted in Figure 1.2 is indistinguishable from Fermi's single-vertex process in Figure 1.1.

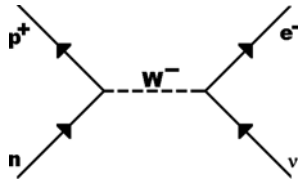

Figure 1.2: The W^- incorporated into β decay.

1.1.1 Parity Violation

In the early 1950's, it was observed that two particles called τ^+ and θ^+ appeared to be identical in all respects, except that they decayed to states of opposite parity. Lee and Yang speculated in 1956 that the τ and θ particles were actually the same particle, with the weak decay mode violating parity [6]. They pointed out that while there was ample evidence that strong and electromagnetic interactions conserve parity, there was no such evidence for weak interactions.

The following year, an experiment by C. S. Wu with polarized ^{60}Co demonstrated unequivocally that indeed the weak force did not respect parity [7]. Since that time, parity violation experiments have been an important probe of the structure of the weak interactions.

1.1.2 Electroweak Unification

In 1961, Glashow presented the first work attempting to unify the weak and electromagnetic interactions into a single framework [8]. In addition to the weak mediators $W^{\pm}$, the theory predicted a weak neutral current, mediated by the Z^0. In 1967, Weinberg and Salam cast the unified electroweak theory in the form of a gauge theory with spontaneous symmetry

breaking to explain the difference in the masses of the weak mediators and the photon [9, 10].

The Glashow-Weinberg-Salam (GWS) theory contains a free parameter, the weak mixing angle θ_W, that determines the relative strengths of the electromagnetic coupling g_e and the weak couplings g_W and g_Z through

$$g_W = \frac{g_e}{\sin\theta_W} \quad \text{and} \quad g_Z = \frac{g_e}{\sin\theta_W \cos\theta_W}.$$

The theory also relates the masses of the weak mediators through

$$M_W = M_Z \cos\theta_W. \tag{1.3}$$

The theory was bolstered in 1973 with the discovery of a weak neutral current event in the Gargamelle bubble chamber at CERN [11]. They observed the interaction

$$\overline{\nu_\mu} + e^- \rightarrow \overline{\nu_\mu} + e^-, \tag{1.4}$$

which could only be mediated by the Z^0 boson.

In 1978, the E122 experiment at SLAC observed the parity-violating asymmetry in polarized electron scattering from a deuterium target. The results were in agreement with the GWS theory, and ruled out competing models [12, 13]. The weak mixing angle was measured to be $\sin^2\theta_W = 0.224 \pm 0.020$.

The knowledge of $\sin^2\theta_W$ and G_F are sufficient to calculate the masses of the W and Z^0 particles in the GWS theory. Using the result of the E122 experiment, it was found that the W particle should have a mass of ≈ 80 GeV/c^2, while the Z^0 should have a mass of ≈ 90 GeV/c^2. In 1983, the $W^\pm$ and Z^0 were found at CERN at the predicted energies, dramatically supporting the GWS electroweak theory [14].

1.1.3 LEP and SLC

The SLC at SLAC and LEP at CERN were e^+e^- colliders that operated in the 1990's to test the Standard Model to high precision near the mass of the Z^0. With few exceptions, the results were in excellent agreement with the theoretical predictions. The precision of the collider results can be appreciated by noting that the weak mixing angle was measured to be

$$\sin^2\theta_W = 0.23113 \pm 0.00015, \tag{1.5}$$

combining all data [15].

1.2 The Role of the E158 Experiment

As with any coupling constant, renormalization causes $\sin^2\theta_W$ to run as a function of the four-momentum transfer Q of an interaction. Figure 1.3 depicts the predicted running of the weak mixing angle with energy. In order to fully explore the Standard Model, measurements must be performed at several different Q values. The E158 experiment complements the work done at the SLC and LEP by operating in an energy range far below the mass of the Z^0. Interference with the dominant electromagnetic diagrams allows low Q^2 experiments unique sensitivity to physics effects beyond the Standard Model.

1.3 E158 Overview

The E158 experiment extracts $\sin^2\theta_W$ at a Q^2 of 0.026 $(\mathrm{GeV/c})^2$ by measuring the parity-violating asymmetry A^{PV} in Møller scattering. The experiment is technically challenging because the asymmetry is expected to be very small, on the order of -150 parts-per-billion. The measurement represents the first time that parity violation has been observed

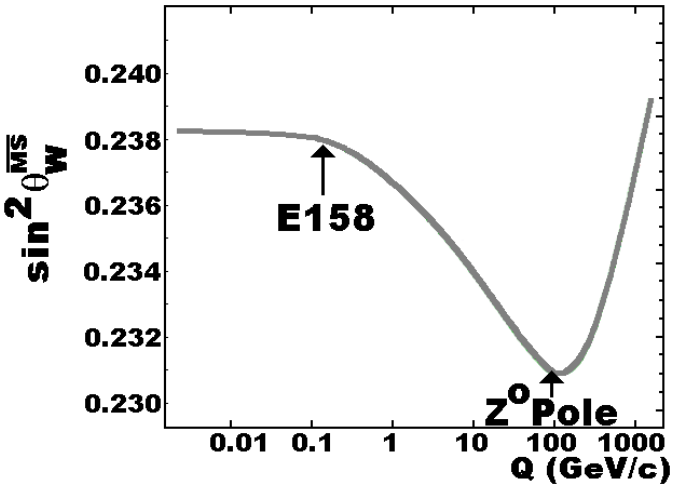

Figure 1.3: The running of $\sin^2\theta_W$ with four-momentum transfer Q.

in electron-electron scattering.

Figure 1.4 presents a general diagram of the E158 apparatus. The experiment utilizes the 48 GeV polarized electron beam provided by the two-mile linear accelerator at SLAC, scattering off of unpolarized atomic electrons in a fixed target of liquid hydrogen. The scattered flux is then integrated with the E158 calorimeter, located in the experimental hall End Station A. The asymmetry A^{PV} is defined as the difference in the scattering rate for each beam helicity, normalized to their sum, given by

$$A^{PV} = \frac{\frac{d\sigma}{d\Omega}^R - \frac{d\sigma}{d\Omega}^L}{\frac{d\sigma}{d\Omega}^R + \frac{d\sigma}{d\Omega}^L}, \tag{1.6}$$

where L and R refer to the helicity of the incident beam.

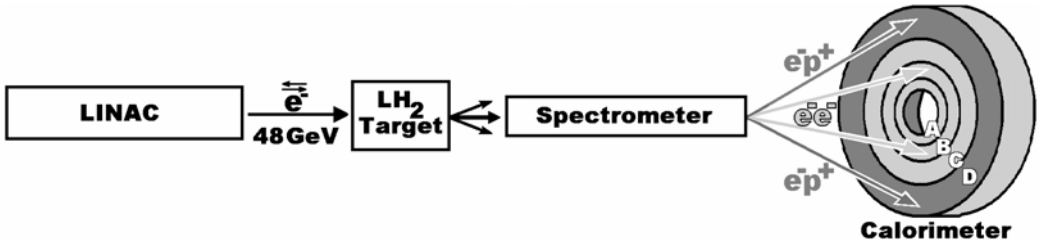

Figure 1.4: General diagram of the E158 apparatus. The regions of the E158 calorimeter are named as follows: A.) In ring B.) Mid ring C.) Out ring and D.) eP detector.

The calorimeter is divided into four annular regions, designated as In, Mid, Out, and eP. The E158 spectrometer focuses the scattered electrons so that the inner three regions of the calorimeter are dominated by Møller scattering events, while the outer eP ring is dominated by electron-proton scatters. The In and Mid region together are known as the Møller detector[2], and are used for the measurement of A^{PV}.

1.4 Experiment Timeline

The data for the E158 experiment was collected over four distinct periods, designated as Run 0 through Run 3. Each data set is analyzed independently to determine $\sin^2\theta_W$. The results of each Run are then combined to obtain the overall E158 result.

Table 1.1 presents the amount of data in each Run. This paper covers the combined results of Run 1 and Run 2, representing slightly over half of the full E158 data set. The analysis of Run 3 is still underway.

Dataset	Time	Total Data (pulses)
Run 0	Winter 2001	Engineering Run
Run 1	Spring 2002	212 million
Run 2	Fall 2002	236 million
Run 3	Summer 2003	360 million

Table 1.1: The E158 dataset boundaries.

[2]The Out region could have been included, but was found to be susceptible to large systematic uncertainties (Section 6.7.2.2).

Chapter 2

Theory

The SLAC E158 experiment measures the parity-violating asymmetry in Møller scattering at a Q^2 five orders of magnitude below the weak scale. The measurement probes the Standard Model at the one loop level, providing insight into the running of the electroweak observable $\sin^2\theta_W$.

This chapter presents the theoretical prediction for the parity-violating asymmetry A^{PV} in Møller scattering and its relation to the weak mixing angle. Additionally, previous low Q^2 electroweak experiments and their results are described.

2.1 The E158 Experiment

The experiment utilizes a 48 GeV polarized electron beam on unpolarized atomic electrons in a liquid hydrogen target to measure the parity-violating asymmetry in Møller scattering, at a Q^2 of 0.026 $(\mathrm{GeV/c})^2$. Radiative corrections reduce the tree-level asymmetry by 40%. The large relative size of higher-order effects allows the experiment to be a sensitive probe of the Standard Model. Sections 2.3 and 2.4 present the theoretical calculation of the expected asymmetry.

The effect from radiative corrections can be neatly accommodated by defining a Q^2 dependent weak mixing angle. Figure 2.1 displays the running of $\sin^2\theta_W(Q^2)$ as well as

the results of several precision electroweak experiments. The NuTeV point refers to a

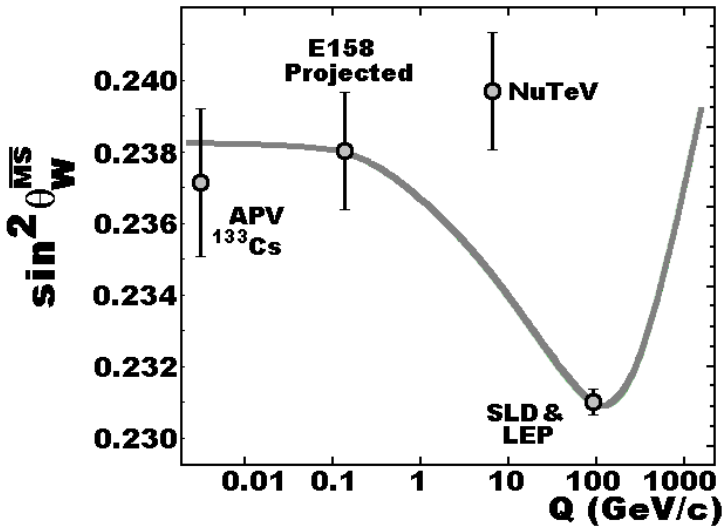

Figure 2.1: The running of $\sin^2\theta_W$ with Q.

neutrino experiment conducted at Fermilab [16], and the APV point represents atomic parity violation studies performed by NIST and the University of Colorado [17]. These experiments are described in Sections 2.2.1 and 2.2.2.

2.2 Previous Low Q^2 Electroweak Measurements

It is clear from Figure 2.1 that the Z-pole experiments have measured $\sin^2\theta_W$ to high precision, and the results are in agreement with the Standard Model. In contrast, the low Q^2 regime has been probed by only two experiments, with much less precision. The lack of electroweak measurements for low Q^2 is the primary motivation for the E158 experiment.

Both the NuTeV experiment and the APV measurements require considerable theoretical input to extract the weak mixing angle. The E158 experiment is designed to complement these experiments by examining the comparatively clean process of Møller scattering. Also, the energy scale is between the previous measurements, allowing the E158 experiment to provide a unique point on the $\sin^2\theta_W(Q^2)$ curve.

2.2.1 NuTeV Experiment Overview

The NuTeV experiment compared neutrino and anti-neutrino scattering rates to determine $\sin^2\theta_W$ [16]. The high purity neutrino beams were delivered by the Fermilab accelerator, and cross sections were measured in a 120-foot-long steel detector. The relevant Feynman diagrams are shown in Figures 2.2 and 2.3. The Q^2 of the experiment was 20 $(\mathrm{GeV/c})^2$.

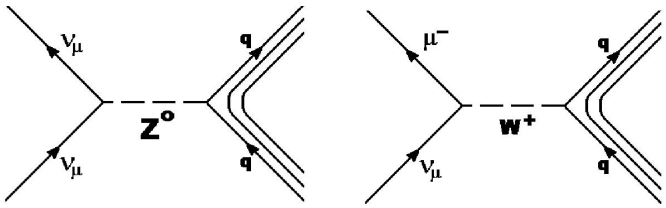

Figure 2.2: Neutrino scattering diagrams.

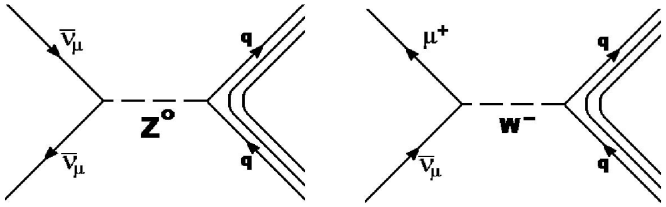

Figure 2.3: Anti-neutrino scattering diagrams.

The weak mixing angle is extracted from the data by constructing the Paschos-Wolfenstein ratio R^- [18], defined as

$$R^- \equiv \frac{\sigma(\nu_\mu N \to \nu_\mu X) - \sigma(\overline{\nu}_\mu N \to \overline{\nu}_\mu X)}{\sigma(\nu_\mu N \to \mu^- X) - \sigma(\overline{\nu}_\mu N \to \mu^+ X)}. \tag{2.1}$$

The quantity R^- is directly related to the weak mixing angle through

$$R^- = \frac{1}{2} - \sin^2\theta_W. \tag{2.2}$$

The NuTeV Collaboration reports a value for $\sin^2\theta_W$ that is 3σ above the Standard Model prediction.

Many attempts have been made to reconcile the NuTeV result within the framework of the Standard Model. The primary focus has been on understanding the parton distribution functions used in the determination of R^-. Nuclear effects are complex, and it is possible to shift the value of $\sin^2\theta_W$ based on the assumptions of these distributions [19]. The induced shifts have not yet been found to align significantly the NuTeV result with the Standard Model prediction. However, a recent $O(\alpha)$ re-analysis of deep-inelastic neutrino scattering indicates that perhaps the theoretical uncertainties used in the extraction of $\sin^2\theta_W$ are enough to reconcile the 3σ shift in the NuTeV result. The work in this area is still ongoing [20].

2.2.2 Atomic Parity Violation Overview

Electroweak experiments in atomic physics measure the perturbation of electronic orbitals induced by Z^0 exchange (Figure 2.4). The potential of the nucleus can be described as due to the standard electric charge Z and the weak charge Q_W. The Q^2 is very low, set by the energy scale of the atomic orbitals.

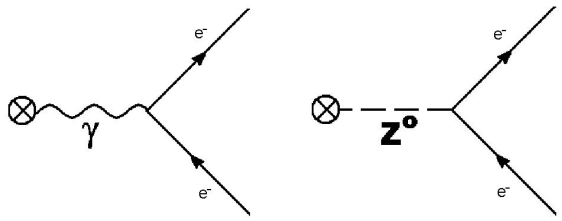

Figure 2.4: Tree-level contributions to the nuclear potential.

The Z^0 diagram produces small mixings of the unperturbed orthogonal electron orbitals. The overlap allows otherwise forbidden transitions to occur. In principle, atomic parity

violation experiments measure transition rates among these states to obtain Q_W.

At tree level, the weak charge of the nucleus is given by

$$Q_W = -N + Z(1 - 4\sin^2\theta_W), \tag{2.3}$$

where N is the number of neutrons and Z is the number of protons [21]. Since $\sin^2\theta_W$ is numerically very close to 0.25, Equation 2.3 essentially reduces the weak charge to the number of neutrons N. Radiative corrections alter the tree-level prediction in Equation 2.3, making atomic parity violation experiments sensitive to the running of the weak mixing angle [22, 23].

Because the weak charge is proportional to the number of neutrons in the nucleus, heavy atoms are the preferred subjects in APV experiments. However, to extract $\sin^2\theta_W$ from a measurement, it is necessary to have a precise model of the electronic wavefunctions involved in the transitions observed. The determination of the wavefunctions in heavy atoms is complex and is the greatest source of uncertainty for atomic parity violation measurements.

The most precise APV experiment utilized ^{133}Cs [17]. Cesium is a good subject because it is a heavy atom with a single valence electron. The experiment initially reported a weak charge that was 2.5σ below the Standard Model prediction. However, subsequent complex electron wavefunction analyses [24, 25, 26, 27, 28, 29] have moved this value to within 0.5σ of the theoretical prediction. The most recent result is plotted in Figure 2.1.

2.3 E158 Experiment at Tree Level

The E158 experiment measures the parity-violating asymmetry A^{PV} in Møller scattering. The asymmetry is defined as

$$A^{PV} \equiv \frac{\frac{d\sigma}{d\Omega}^R - \frac{d\sigma}{d\Omega}^L}{\frac{d\sigma}{d\Omega}^R + \frac{d\sigma}{d\Omega}^L}, \tag{2.4}$$

where $\frac{d\sigma}{d\Omega}$ is the differential cross section, and L and R refer to the helicity of the electron beam. The target electrons are unpolarized. At tree level, there are four diagrams which contribute to A^{PV}, depicted in Figure 2.5. In the limit that $m_{e^-}^2 << Q^2 << m_{Z^0}^2$, the

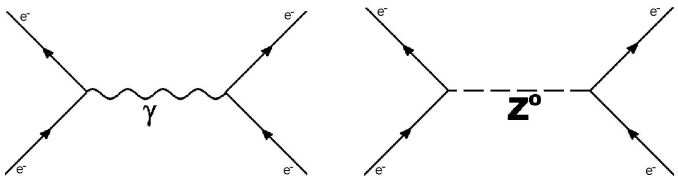

+ Crossed Diagrams

Figure 2.5: Tree-level contributions to A^{PV}.

asymmetry is given by [30]

$$A_{Tree}^{PV} = \frac{-G_\mu Q^2}{\sqrt{2}\pi\alpha} \frac{1-y}{1+y^4+(1-y)^4}(1-4\sin^2\theta_W), \tag{2.5}$$

where

$$y \equiv \frac{1-\cos\theta_{CM}}{2}. \tag{2.6}$$

G_μ is the Fermi constant obtained from the muon lifetime formula [31], and the fine structure constant α is roughly $\frac{1}{137}$, as is suitable for low Q^2 measurements. The θ_{CM} term refers to the center-of-momentum scattering angle.

Because $\sin^2\theta_W \approx \frac{1}{4}$, A^{PV} is very sensitive to the weak mixing angle. The relation is

made clear by noting

$$\frac{\Delta A^{PV}}{A^{PV}} = \frac{\Delta \sin^2\theta_W}{\frac{1}{4} - \sin^2\theta_W}. \tag{2.7}$$

The final E158 result is expected to measure A^{PV} to the precision of 12%, corresponding to a determination of $\sin^2\theta_W$ to ± 0.0014.

It is important to note that the tree-level asymmetry given in Equation 2.5 is a very small number. Even at its maximum ($y = \frac{1}{2}$), A^{PV}_{Tree} is only -300 ppb (parts-per-billion). It is the smallness of this number that presents the greatest challenge to the success of the experiment.

2.4 Radiative Corrections to A^{PV}

Because the tree-level asymmetry is suppressed by a factor of $1 - 4\sin^2\theta_W$, the contribution of higher-order diagrams is effectively enhanced. This feature is responsible for the running of the weak mixing angle in Figure 2.1, and allows the E158 experiment to be a sensitive probe of the Standard Model.

Marciano has evaluated A^{PV} including one-loop radiative corrections and found the corrected asymmetry to be given by [32]

$$\begin{aligned} A^{PV} &= \frac{-\rho G_\mu Q^2}{\sqrt{2}\pi\alpha}\frac{1-y}{1+y^4+(1-y)^4} \times \Big\{ 1 - 4\kappa(0)\sin^2\theta_W + \frac{\alpha}{4\pi\sin^2\theta_W} \\ &\quad - \frac{3\alpha(1-4\sin^2\theta_W)}{32\pi\sin^2\theta_W\cos^2\theta_W}[1+(1-4\sin^2\theta_W)^2] + F_1(y,Q^2) + F_2(y,Q^2) \Big\}, \end{aligned} \tag{2.8}$$

where

$$\sin^2\theta_W \equiv \sin^2\theta_W^{\overline{MS}}(M_{Z^0}^2). \tag{2.9}$$

The term in the braces now has a Q^2 dependence, producing the running of $\sin^2\theta_W$ depicted in Figure 2.1. The precise definition of $\sin^2\theta_W(Q^2)$ is given in Section 2.4.5.

The one-loop corrections reduce the tree-level prediction for A^{PV} by $\approx 40\%$. The expected asymmetry for the E158 experiment is then roughly -180 ppb, for $y = \frac{1}{2}$. The following sections describe the sources and sizes of the terms in Equation 2.8.

Because the effect of higher-order diagrams is large for low Q^2, the E158 experiment can be used as a sensitive probe for physics effects beyond the Standard Model at the TeV scale. Section 7.2 describes the new physics limits that can be set with the experiment, as well as presenting the current limits set by previous experiments.

2.4.1 $\gamma - Z^0$ Mixing Diagrams

The largest one-loop corrections are contained in the $\kappa(0)$ term in Equation 2.8. The relevant processes are represented by $\gamma - Z^0$ mixing diagrams and the W contribution to the electron anapole moment, depicted in Figure 2.6. The Q^2 dependence of these diagrams is contained in $F_2(y, Q^2)$.

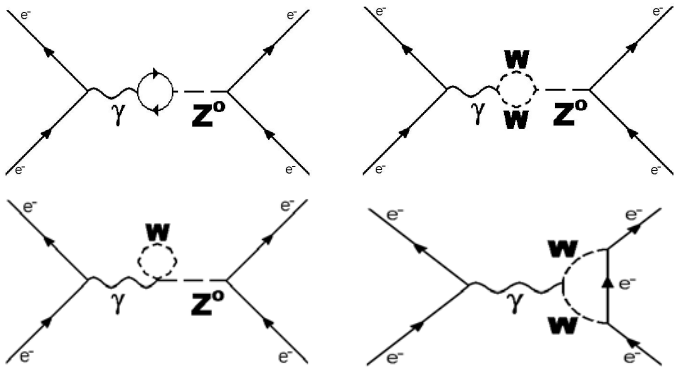

Figure 2.6: Photon-Z^0 mixing diagrams and the W contribution to the anapole moment.

The fermionic loop in the first diagram in Figure 2.6 presents the greatest calculational

challenge. The quark contribution cannot be evaluated perturbatively and must be determined from e^+e^- →hadrons experimental data. The uncertainty on κ represents the largest contribution to the theoretical uncertainty on A^{PV}. Evaluating the diagrams, κ is found to be

$$\kappa(0) = 1.0301 \pm 0.0025. \tag{2.10}$$

The 3% correction to $\sin^2\theta_W$ by $\kappa(0)$ corresponds to a 37% reduction in A^{PV}. It should be noted here that $F_2(\frac{1}{2}, 0.026\ (\mathrm{GeV/c})^2) = 0.00002$, a negligible contribution.

2.4.2 Heavy Box Diagrams

Box diagrams containing heavy bosons comprise the next correction to A^{PV}_{Tree}. These diagrams are depicted in Figure 2.7. The W diagram contributes the $\frac{\alpha}{4\pi \sin^2\theta_W}$ term in Equation 2.8. It yields a 4% increase in A^{PV} over the tree-level expression. The Z diagrams produce the $\frac{-3\alpha(1-4\sin^2\theta_W)}{32\pi \sin^2\theta_W \cos^2\theta_W}[1 + (1-4\sin^2\theta_W)^2]$ term in Equation 2.8, resulting in a negligible 0.1% shift to the tree-level expression.

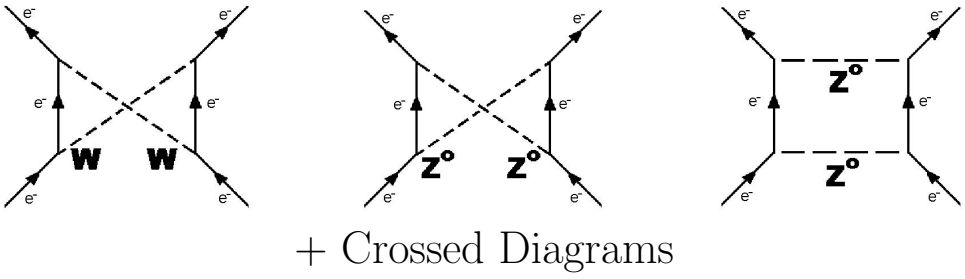

Figure 2.7: Heavy boson box diagrams.

2.4.3 $\gamma - Z^0$ Box Diagrams

The final contribution to the one-loop corrected value of A^{PV}_{Tree} comes from box diagrams containing both a photon and a Z^0 exchange. The relevant diagrams are depicted in Fig-

ure 2.8. The Z^0 contribution to the electron anapole moment also contributes at this level, shown in Figure 2.9.

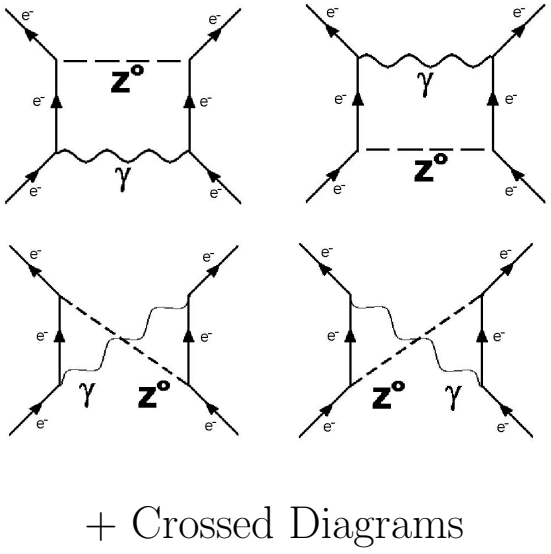

Figure 2.8: Photon-Z^0 box diagrams.

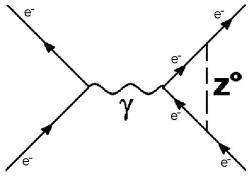

Figure 2.9: Anapole moment contribution from the Z^0.

The contribution of these diagrams is contained in the $F_1(y, Q^2)$ term in Equation 2.8. Evaluating F_1 for the values appropriate for the experiment, it is found that

$$F_1\left(\frac{1}{2}, 0.02\ (\mathrm{GeV/c})^2\right) = -0.0041 \pm 0.0010. \tag{2.11}$$

The F_1 function constitutes a 6% reduction in A^{PV}_{Tree}, largely canceling the previous W box diagram term.

2.4.4 ρ Term

The ρ term in Equation 2.8 follows from the convention chosen for G_μ and renormalization of the Z amplitude [33]. The explicit form is

$$\rho = 1 + \frac{\alpha}{4\pi} \times \left\{ \frac{3}{4\sin^4\theta_W} \log\cos^2\theta_W - \frac{7}{4\sin^2\theta_W} + \frac{3}{4\sin^2\theta_W}\frac{m_t^2}{m_W^2} + \frac{3m_H^2}{4\sin^2\theta_W m_Z^2}\left(\frac{\log\cos^2\theta_W \frac{m_Z^2}{m_H^2}}{\cos^2\theta_W - \frac{m_H^2}{m_Z^2}} + \frac{1}{\cos^2\theta_W}\frac{\log\frac{m_H^2}{m_Z^2}}{\cos^2\theta_W - \frac{m_H^2}{m_Z^2}} \right) \right\}, \tag{2.12}$$

where m_t refers to the mass of the top quark, and m_H denotes the mass of the Standard Model Higgs. The dependence on these masses is very slight. The other masses, m_Z and m_W , refer to the standard weak gauge bosons. Assuming $m_t = 170$ GeV/c^2 and $m_H = 200$ GeV/c^2, one finds $\rho = 1.00122$, a totally negligible correction to the overall asymmetry.

2.4.5 Definition of $\sin^2\theta_W(Q^2)$

The precise definition of $\sin^2\theta_W(Q^2)$ is a matter of convention. Often, only the terms due to the γ-Z mixing and the W contribution to the electron anapole moment (Section 2.4.1) are grouped into the definition of the weak mixing angle through

$$1 - 4\sin^2\theta_W^{\overline{MS}}(Q^2) \equiv 1 - 4\kappa(0)\sin^2\theta_W^{\overline{MS}}(M_Z^2) + F_2(Q^2). \tag{2.13}$$

The definition established in Equation 2.13 is typically preferred by theorists, and was used to produce Figure 2.1.

On the other hand, experimentalists usually report an "effective" weak mixing angle.

This amounts to defining $\sin^2\theta_W(Q^2)$ so that the tree-level asymmetry formula holds, with

$$
\begin{aligned}
1-4\sin^2\theta_W^{eff}(Q^2) \quad \equiv \quad & \\
& \rho\left\{1-4\kappa(0)\sin^2\theta_W+\frac{\alpha}{4\pi\sin^2\theta_W}\right. \\
& -\frac{3\alpha(1-4\sin^2\theta_W)}{32\pi\sin^2\theta_W\cos^2\theta_W}[1+(1-4\sin^2\theta_W)^2] \\
& \left.+F_1(y,Q^2)+F_2(y,Q^2)\right\}
\end{aligned}
\tag{2.14}
$$

Due to cancellations, the two definitions are very nearly equal for low Q^2. For the parameters of the E158 experiment, one finds $\sin^2\theta_W^{\overline{MS}}=0.2381$ and $\sin^2\theta_W^{eff}=0.2385$.

Chapter 3

E158 Beamline and Beam Monitoring

This chapter describes the major components of the E158 apparatus, from the beginning of the accelerator up to the final collimation before the detectors. The polarized beam, precision beam monitors, the liquid hydrogen target, and the spectrometer are covered.

3.1 Polarized Source

The helicity of the primary electron beam is controlled at the polarized source, located upstream of the linac (Figure 3.1). The source houses a complex optical system, depicted in Figure 3.2, which is employed to produce high beam polarization while minimizing susceptibility to helicity-correlated systematic effects [34, 35]. The following sections detail the components of the optical system and their relevance to the E158 experiment.

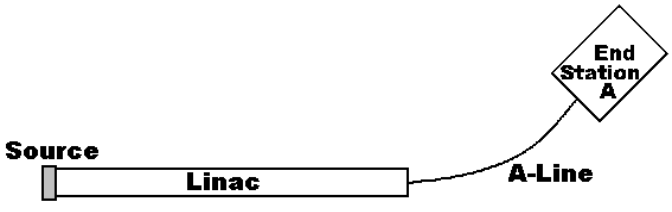

Figure 3.1: Location of the polarized source room.

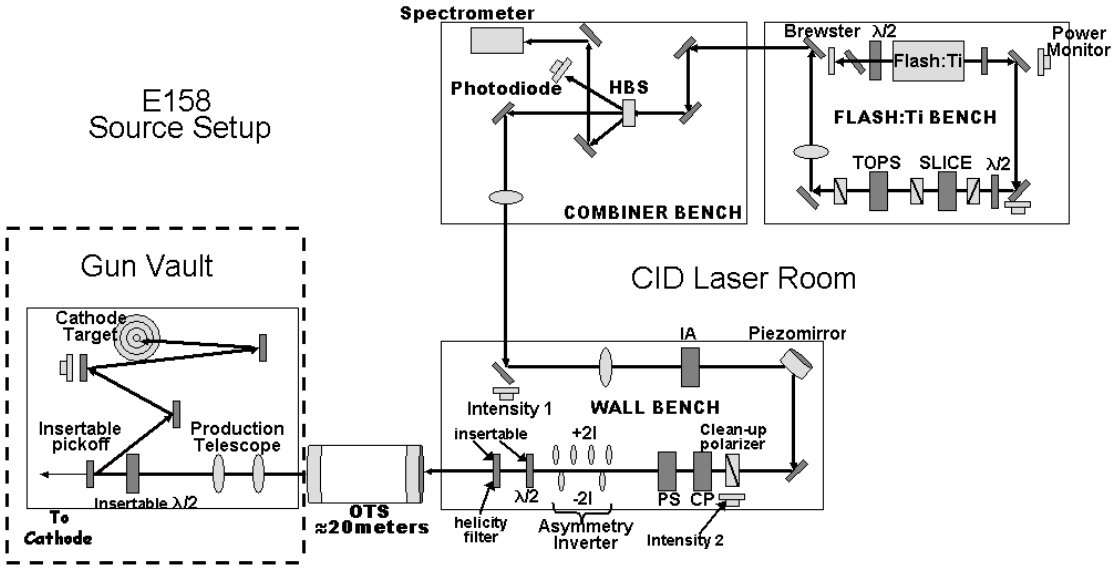

Figure 3.2: E158 optics configuration at the source.

3.1.1 Laser Bench

Laser light production and pulse-shaping occur on the laser bench. The system begins with a Flash:Ti laser which generates 12 μs pulses of linearly polarized light. A Brewster tuner is utilized to control the wavelength of the laser, holding it to within 4 nm of the central 854 nm wavelength. At 120 Hz, the laser power is roughly 2 W.

The Slice Pockels cell is used to sample the 300 ns portion of the laser pulse with the most favorable characteristics, balancing intensity with jitter. The Slice cell is a piezoelectric crystal, with optical properties that are affected by the applied voltage. At zero Volts the crystal is optically neutral, while at 3000 Volts it functions as a half-wave plate. The Slice cell sits between two crossed linear polarizers. Biasing the Slice as a quarter-wave plate allows the laser light to pass through both polarizers. When the cell is unbiased, an extinction ratio of 500 is achieved.

The Tops Pockels cell is used to shape the time profile of the laser pulse, to match the properties of the cathode. The Tops cell is placed between aligned linear polarizers and is

pulsed at low voltage to produce mild light extinction.

3.1.2 Combiner Bench

The elements on the combiner bench are only used for diagnostics. The harmonic beam splitter (HBS) diverts roughly 2% of the laser light to two separate beam monitors. The spectrometer records the laser wavelength, while the photodiode is used to monitor laser power.

3.1.3 Wall Bench

The components on the wall bench are used to define the helicity of the electron beam and to suppress helicity-correlated beam asymmetries. The intensity asymmetry (IA) Pockels cell is part of a feedback system designed to reduce the charge asymmetry of the electron beam. Analogous to the Tops cell, the IA cell is operated at low voltage between aligned linear polarizers. It is pulsed based on charge measurements performed early in the linac.

The circular polarizer (CP) and phase shifter (PS) Pockels cells are responsible for defining the helicity of the beam that ultimately reaches the cathode. The CP cell is pulsed at its quarter-wave voltage, converting the incoming light from linear to circular polarization. The helicity of the light is reversed by changing the sign of the voltage bias. The PS cell is run at lower voltages and is used primarily to correct for residual linear polarization left by the CP cell.

The piezomirror is used to reduce helicity-correlated beam position asymmetries. Like the IA Pockels cell, the piezomirror is controlled based on beam measurements using monitors early in the linac. The voltage applied to the mirror changes the angle of reflection, ultimately moving the laser spot on the cathode.

The asymmetry inverter is used to combat helicity-correlated effects due to asymmetries in the laser profile on the cathode. The inverter lenses can be moved as a unit between two configurations. The settings complement each other, with one spatially inverting the beam profile compared to the other. The lenses were toggled once in Run 1 and once in Run 2.

Following the wall bench, the laser light travels down the Optical Transport System (OTS) to the cathode. The OTS is essentially a 20 m pipe, filled with nitrogen, linking the source room with the cathode room. It contains several lenses configured to preserve the quality of the beam.

3.1.4 Polarized Gun

The gun bench holds the final optics preceding the cathode. The lenses on the bench are configured as a telescope, used to match the laser spot size to the dimensions of the cathode. A mirror can be inserted after the lenses to divert the laser beam to a diagnostic target. Optically, the target is in the same position as the real cathode. Centering light on the target ensures that the light will be centered on the cathode when the mirror is removed. The target is monitored remotely by a camera.

The final component on the bench is an insertable half-wave plate. It is used to combat helicity-correlated systematic effects by reversing the helicity of the laser light defined with the CP cell, while leaving the rest of the system unchanged. The wave plate is toggled once every two days during E158 production running.

The cathode used for the E158 experiment is composed of a strained GaAs lattice [36]. This type of cathode has been found to provide the highest presently achievable beam polarization along with high current. The polarization of the E158 electron beam was measured to be $\sim$85% (Section 4.2), with no evidence that the cathode was charge limited.

3.1.5 Helicity Sequence

The helicity of the electron beam is defined in sets of four pulses. The helicity of the first pair is chosen randomly, while the second pair is the conjugate of the first. Each quad of pulses then contains two separate sets of pulses, with the first pulse paired with the third and the second pulse paired with the fourth. Figure 3.3 illustrates the pulse sequence.

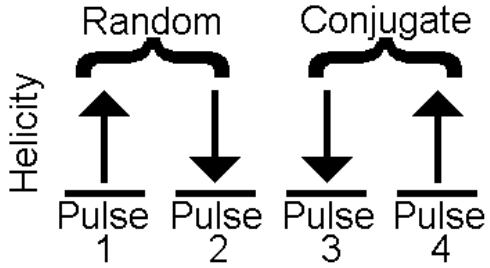

Figure 3.3: Helicity of the E158 electron beam.

Pairs of pulses, rather than single pulses, are the fundamental unit of the experiment. Quantities of the form

$$\frac{Pulse^R - Pulse^L}{Pulse^R + Pulse^L} \tag{3.1}$$

are called asymmetries, where L and R refer to the helicity state. The results from the detectors are reported as asymmetries. The units appropriate for the E158 experiment are ppm or ppb, signifying parts-per-million or parts-per-billion. Quantities of the form

$$Pulse^R - Pulse^L \tag{3.2}$$

are called differences, but may also be referred to as asymmetries. Beam position monitor results are reported in this form.

3.1.6 Beam Asymmetries

The polarized source is configured to decrease the size of helicity-correlated beam asymmetries. For a full E158 dataset, careful calibration of the positive and negative CP cell bias voltages suppresses the expected intensity asymmetry from ∼1000 ppm down to ∼100 ppm. The intensity asymmetry feedback then reduces the asymmetry to ∼100 ppb [35]. The large suppression is critical for controlling systematic uncertainties because A^{PV} is only ≈ -150 ppb.

Figure 3.4 depicts the integrated charge asymmetry versus time for the toroid used for the intensity feedback. The horizontal scale covers all of Run 1 and Run 2. The dotted line indicates purely statistical scaling. The final asymmetry is at the level of a few hundred ppb, as expected with the feedback asymmetry suppression.

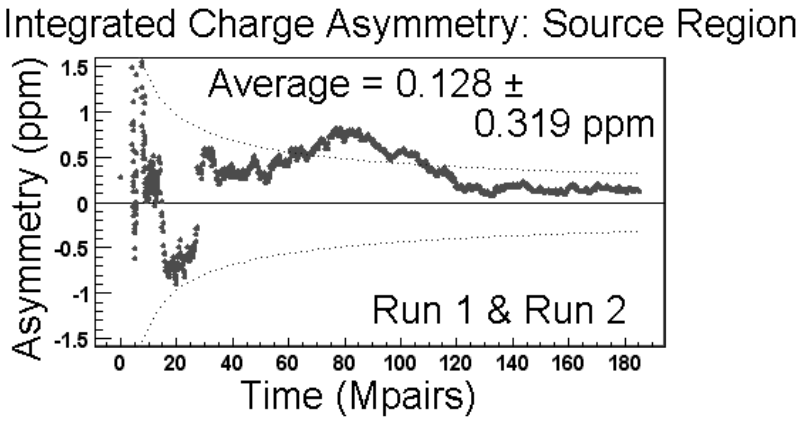

Figure 3.4: Integrated charge asymmetry measured near the source, spanning all of Run 1 and Run 2.

While the intensity feedback ensures that the charge asymmetry near the beginning of the linac is suppressed, it is the asymmetry at the target, more than two miles away, that is the relevant quantity for the E158 analysis. Figure 3.5 depicts the charge asymmetries measured by the toroids just upstream of the target for both Run 1 and Run 2. The asymmetry suppression due to the intensity feedback clearly translates into the target region,

Run 1	
Parameter	Integrated Asymmetry
Charge	210 ± 319 ppb
Energy	-0.1 ± 1.4 keV
X	-16.3 ± 5.6 nm
Y	-3.0 ± 4.0 nm
X Angle	0.38 ± 0.23 nR
Y Angle	0.11 ± 0.07 nR

Run 2	
Parameter	Integrated Asymmetry
Charge	496 ± 335 ppb
E	0.9 ± 2.1 keV
X	13.0 ± 6.7 nm
Y	-15.9 ± 5.2 nm
X Angle	0.33 ± 0.22 nR
Y Angle	0.13 ± 0.11 nR

Table 3.1: Integrated asymmetries for Run 1 and Run 2.

although the convergence is not as strong as at the source.

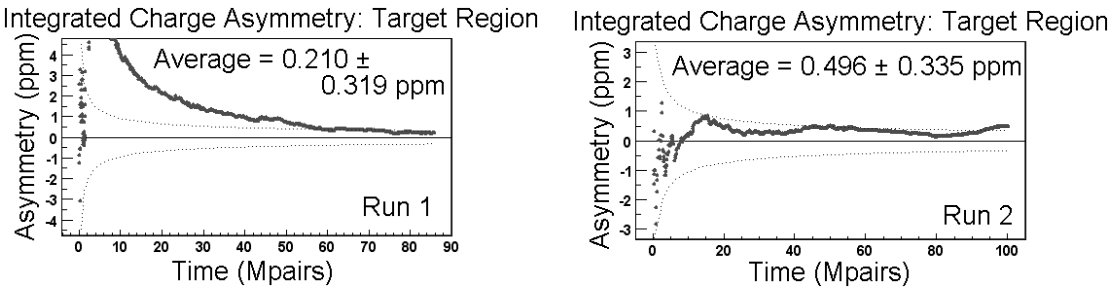

Figure 3.5: Run 1 and Run 2 target region integrated charge asymmetry.

Since most beam parameters are correlated to charge, the intensity asymmetry feedback also suppresses position asymmetries. (The position feedback with the piezomirror is also employed, though it proved to be less effective than the IA feedback.) In the absence of feedbacks, position asymmetries at the ∼100 μm would be expected for an E158 data set. The feedbacks suppress the asymmetries to the level of ∼1 nm. Table 3.1 presents the integrated asymmetries for Run 1 and Run 2.[1] The asymmetry suppression observed is at the level expected for the experiment [37].

[1]The average asymmetry is computed by weighting the data with the resolution of the primary E158 detector. The asymmetries are then directly applicable to the analysis of the detector results.

3.2 Beam Position Monitors

The position of the electron beam is measured with RF cavity beam position monitors (BPMs). Figure 3.6 depicts the location of the E158 BPMs. The X and Y positions of the beam at the target are measured with the target BPMs. The X and Y angles are computed using the difference between the target and angle BPMs, which are separated by 40 meters. The energy BPMs are located in an area of high dispersion so that a horizontal position measurement actually corresponds to an energy determination. The three BPMs located close to the source are employed for the source position feedback.

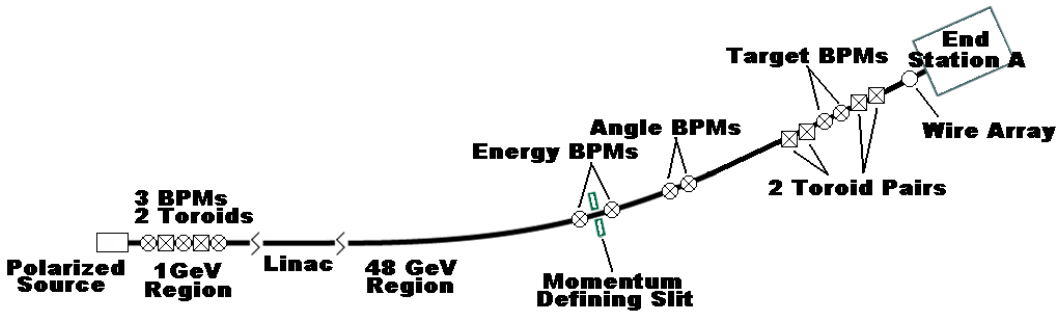

Figure 3.6: Location of E158 beam monitors.

3.2.1 BPM Operation

The beam position monitors are composed of three separate cavities [38]. Figure 3.7 is a picture of an E158 BPM. When the electron beam traverses the device, it excites the resonant electromagnetic modes of the cavities. The amplitude of the response is picked up by an antenna in each cavity and read out as the signal.

The rectangular cavities are employed to measure X or Y position. The beam excites either the TM_{210} or TM_{120}, with an amplitude that is proportional to both beam position and charge. The position cavities are then normalized to beam charge with the E158 toroids (Section 3.3), leaving only the sensitivity to position.

The final BPM cavity is cylindrical, and is only sensitive to beam charge. In principle, it could be used for the normalization of the BPM position cavities. The toroids were used instead because they have superior charge asymmetry resolution.

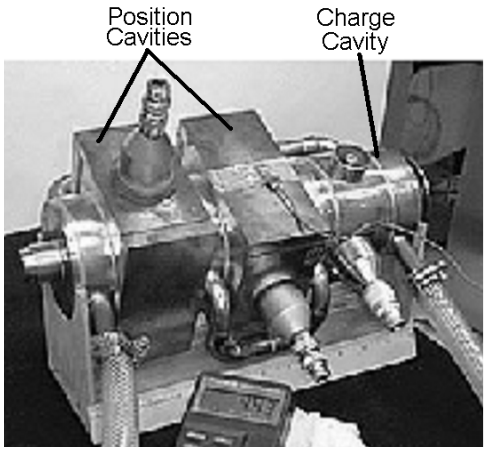

Figure 3.7: E158 beam position monitor.

Each E158 beam pulse is roughly 300 ns long. However, the pulse itself is composed of smaller electron bunches, grouped at the 2856 MHz rate of the accelerator. The BPM cavities respond to the bunches, producing a signal that oscillates at the accelerator rate. The resonant frequency of the cavities is 2856 ± 0.3 MHz, designed to optimize the response of the device.

The oscillation in the output signals is removed by mixing the BPM signals with an auxiliary signal locked to the accelerator rate. The mixing electronics produce two outputs, with amplitudes proportional to the amount of signal in phase or out of phase with the auxiliary signal. The mixer is tuned so that one of the output signals is maximized, minimizing the other. A feedback system was employed to ensure that phase drifts are counteracted and the primary signal remains a maximum.

Figure 3.8 depicts the two signals returned by the mixer for one of the BPM cavities. The signal quickly increases with the 300 ns beam pulse and then exponentially decays.

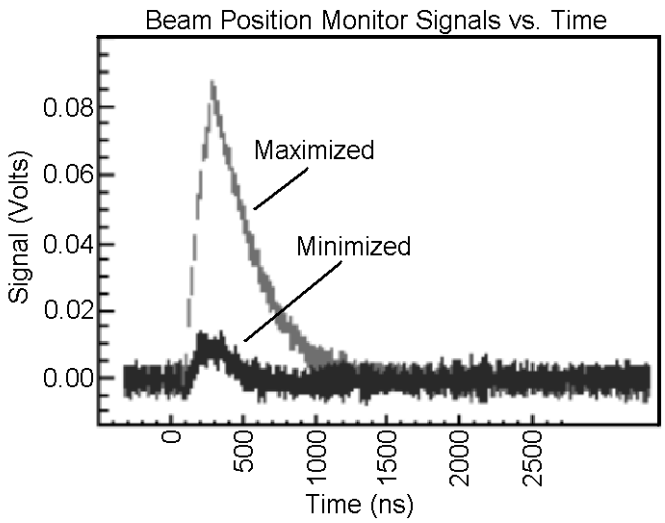

Figure 3.8: BPM signals after mixing.

The signals are read into custom built 16-bit VME ADCs (analog to digital converters) as part of the data stream. High-resolution ADCs are required to match the resolution of the BPMs.

3.2.2 BPM Performance

The BPMs are deployed in pairs or triplets (Figure 3.6) to allow for cross-checks between devices in close proximity. The performance of a BPM pair is quantified by the distribution of the agreement δ, defined as

$$\delta_i \equiv \frac{1}{2}(\Delta BPM_i^1 - \Delta BPM_i^2), \tag{3.3}$$

where ΔBPM_i^n indicates the position difference measured with BPM^n for the ith pulse pair. The width of the distribution is the pulse-pair resolution of the BPM pair. Figures 3.9 and 3.10 depict typical resolutions of the E158 BPMs.

The resolution of each of the BPMs exceeds the requirements of the E158 experiment. This can be demonstrated by noting that the asymmetry measured with the Møller detector

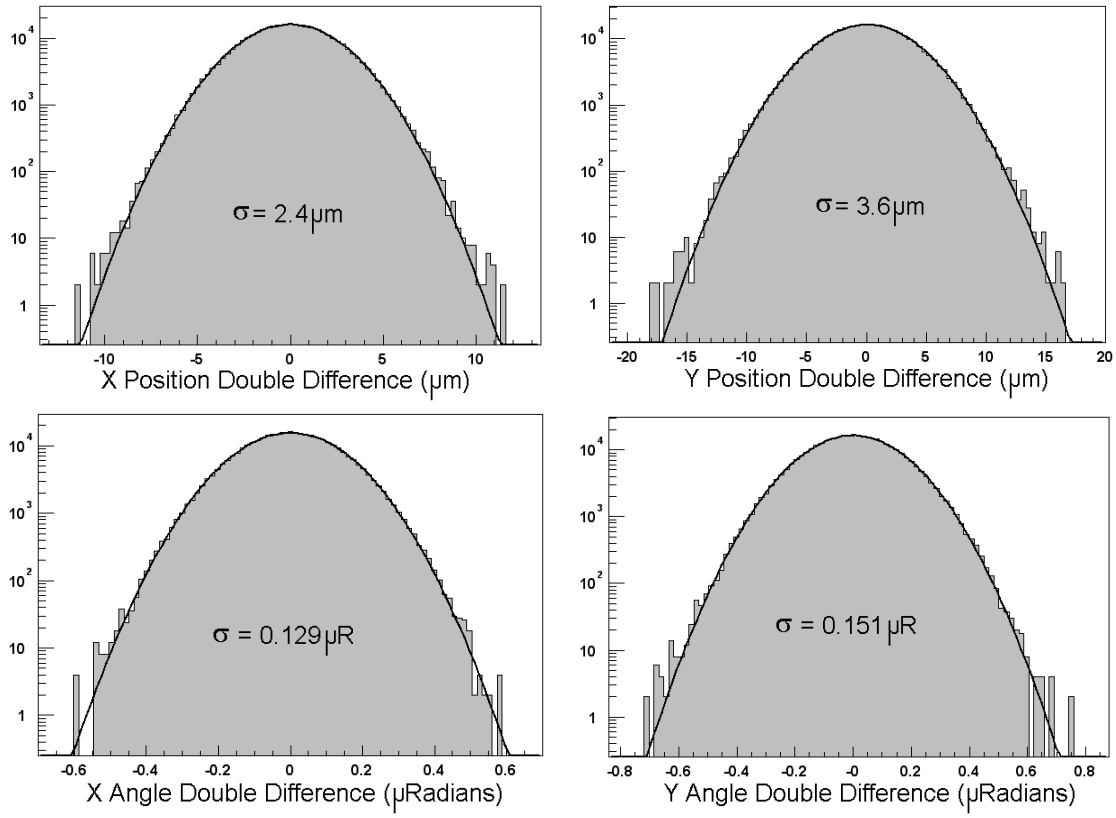

Figure 3.9: Angle and position BPM resolutions.

is corrected for beam asymmetries by

$$A^{PV} = A^{Raw} - \sum_{n=1}^{5} c_n \Delta BPM_n, \tag{3.4}$$

where A^{PV} is the true physics asymmetry, A^{Raw} is the measured detector asymmetry, ΔBPM_n is the position difference measured with BPM_n, and c_n is the experimentally determined sensitivity of the detector to beam motion. The sum covers the beam parameters of energy, X and Y position, and X and Y angle. This method is called regression, and is discussed in detail in Section 6.3. The resolution of the BPMs contributes to the resolution

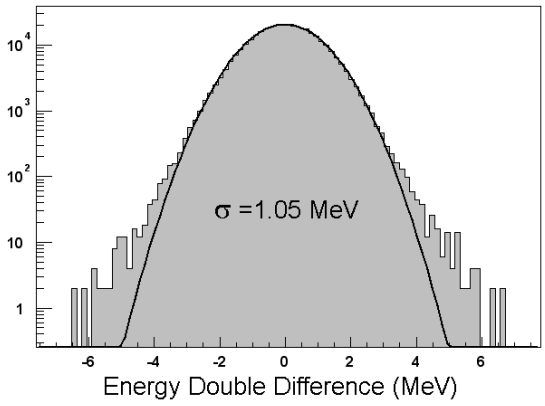

Figure 3.10: Energy BPM resolutions.

Parameter	Detector Coefficient c	BPM Resolution	Resolution Contribution
X	-0.1 ppm/μm	2.4μm	0.2 ppm
Y	-1.3 ppm/μm	3.6μm	4.7 ppm
Angle X	-52.6 ppm/μR	0.13μR	6.8 ppm
Angle Y	12.1 ppm/μR	0.15μR	1.8 ppm
Energy	-15.2 ppm/MeV	1.1 MeV	16.7 ppm
Total			18.7 ppm

Table 3.2: BPM contribution to Møller detector resolution.

of the detector $\sigma_{Detector}$ through

$$\sigma^2_{Detector} = \sum_{n=1}^{5} (c_n \sigma_n^{BPM})^2, \tag{3.5}$$

where σ_n^{BPM} is the resolution of BPM_n. The contributions to the resolution of the Møller detector are presented in Table 3.2. The resolution of the detector is typically around 200 ppm, while the contribution due to BPM resolution is negligible, at less than 20 ppm.

The resolution of the BPMs is also constrained by the general goal that individual contributions to the systematic uncertainty on A^{PV} be 5 ppb or less, over a full dataset. The uncertainty on A^{PV} measured with the Møller detector due to the BPM corrections is

$$\sigma_A^{PV} = \sum_{n=1}^{5} c_n < \delta_n >, \tag{3.6}$$

Parameter	Detector Coefficient c	BPM Agreement δ	$\sigma_{A^{PV}}^{systematic}$
X	0.4 ppm/μm	1.0 $\pm$ 0.6 nm	0.4 $\pm$ 0.2 ppb
Y	-1.2 ppm/μm	0.0 $\pm$ 1.0 nm	0.0 $\pm$ 1.2 ppb
Angle X	-66.1 ppm/μR	-0.07 $\pm$ 0.05 nR	4.6 $\pm$ 3.3 ppb
Angle Y	7.3 ppm/μR	0.02 $\pm$ 0.03 nR	0.1 $\pm$ 0.2 ppb
Energy	-25.9 ppm/MeV	0.0 $\pm$ 0.2 keV	0.0 $\pm$ 5.2 ppb

Table 3.3: Run 1 Estimate of uncertainty on A^{PV} due to BPM corrections.

where $< \delta_n >$ is the average BPM agreement for the n^{th} BPM pair[2]. Table 3.3 details the observed BPM agreement for Run 1 and the contribution to the uncertainty on A^{PV} [39]. The uncertainty on the agreement is proportional to the resolution of the BPMs.

Each uncertainty on $\sigma_{A^{PV}}^{systematic}$ is near the goal of 5 ppb or below for all beam parameters, implying that the BPM resolution is adequate for the experiment.

3.3 Charge Monitors

The beam charge is measured by several toroids distributed along the beamline (Figure 3.6). The toroids located near the source are used for the intensity feedback, while the toroids near the target are used for normalizing the detector signals. Specifically, the raw asymmetry A^{Raw} measured with the Møller detector is

$$A^{Raw} = \frac{\left(\frac{M}{T}\right)^R - \left(\frac{M}{T}\right)^L}{\left(\frac{M}{T}\right)^R + \left(\frac{M}{T}\right)^L}, \tag{3.7}$$

where M and T refer respectively to the Møller detector and toroid signals, and L and R refer to the helicity of the beam.

[2]It will be demonstrated in Section 6.7.2.2 that this is a naive estimate. For the present purposes, however, it is adequate.

3.3.1 Toroid Overview

Each toroid is composed of an iron ring wrapped with copper wire, positioned around ceramic portions of the beam pipe. When a charged particle passes through the ring, a voltage is produced in the wire by inductance. The signal is then amplified and sent through a rectifier before being read into the ADCs as the charge measurement.

3.3.2 Toroid Performance

Because the toroid signal is used for normalizing the detector signal, it is desirable that the toroid intensity asymmetry resolution be much better than the Møller detector resolution of 200 ppm.

The toroid resolution is determined experimentally in a fashion similar to the method employed for the BPMs in Equation 3.3. The resolution is defined as the width of the distribution of the agreement δ_i, given by

$$\delta_i = \frac{1}{\sqrt{2}}(A_i^1 - A_i^2). \tag{3.8}$$

The A_i^n terms refer to the asymmetry measured by toroid n for the i^{th} beam pulse. The prefactor is $\frac{1}{\sqrt{2}}$, instead of $\frac{1}{2}$ used for the BPMs because only one toroid is used for the charge normalization, instead of a pair.

Figure 3.11 presents the distribution of the agreement δ for a typical one-hour data run. The width is 59 ppm, which is well below the 200 ppm resolution of the Møller detector. The average resolution during the experiment was actually closer to 50 ppm, while periods as low as 30 ppm were observed. The drifts in resolution appear to be coming from the toroid amplifying electronics.

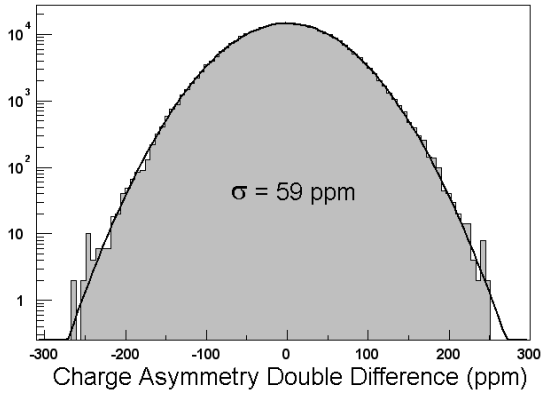

Figure 3.11: Toroid resolution.

The toroids are also required to have a signal response as linear as the detectors, because they are used for direct normalization. Section 4.1.4 demonstrates that the Møller detector is linear to the level of roughly 99%, so it is required that the toroid be linear to that level as well.

Each toroid mounted on the beamline has a single wire passing through its ring that can be used for *in situ* calibration and linearity testing. A calibrator which can produce pulses with better than 0.05% charge stability is used to test the response of the toroid to several different currents. The curvature in the plot of the toroid versus the calibrator determines the linearity.

Figure 3.12 presents the results of a toroid linearity test. The error bars on the plot, due to calibrator fluctuations, are much smaller than the data points themselves. Also note that the toroid is normalized so that its slope versus the calibrator is unity. The coefficient of the second order term in the fit is quite small, indicating that the toroid is linear to better than 99%, as required.

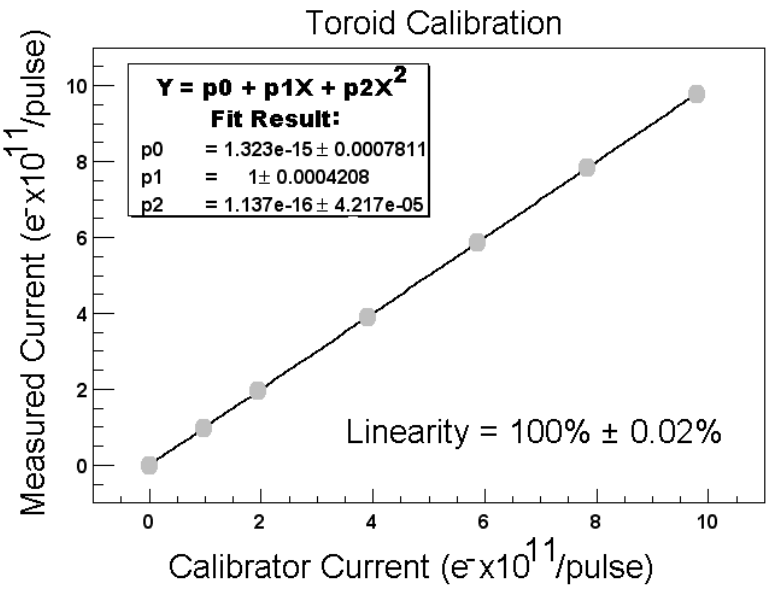

Figure 3.12: Toroid signal versus calibrator signal.

3.4 Wire Array

The transverse spatial profile of the beam is monitored with a device called the wire array. It is positioned directly upstream of the target (Figure 3.6) and can be remotely moved in and out of the beam path. It is composed of two sets of 48 parallel wires, one horizontal and one vertical, forming a grid through which the beam passes. The wires are composed of a copper-beryllium alloy, with a diameter of 180 microns and a spacing of 356 microns. When the beam passes through the grid, it causes the wires to lose electrons, producing a small voltage which is read out as the signal. Foils near the wires are held at positive potential to attract the liberated electrons to reduce the chance for recombination, enhancing the signal by a factor of two. Figure 3.13 presents a typical profile measurement provided by the wire array. The beam shape is roughly Gaussian in both axes, with an RMS of approximately 1 mm.

In addition to monitoring the shape of the beam, the wire array is used to measure the helicity-correlated spot size asymmetry. The size and uncertainty of the spot size asymmetry

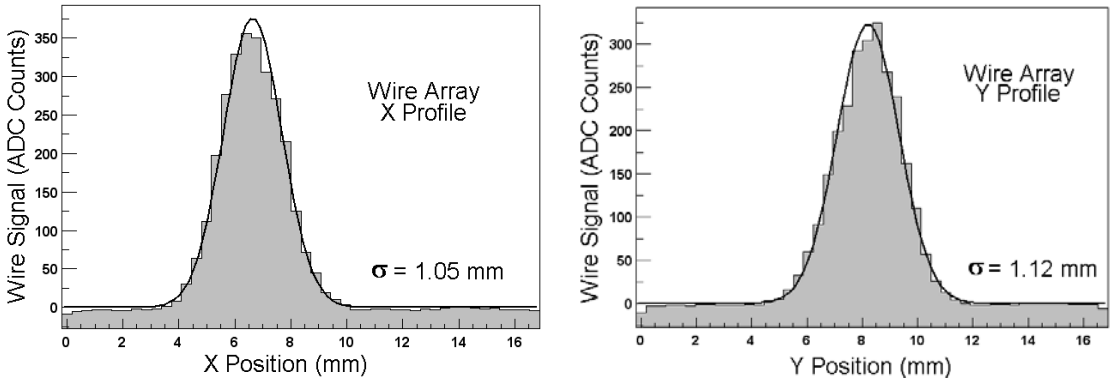

Figure 3.13: Wire array profiles for both X and Y axes.

have implications for the systematic uncertainty on A^{PV} measured with the Møller detector.

The detector sensitivity to spot size α can be expressed as

$$A^{Measured} = A^{PV} + \alpha \Delta S, \tag{3.9}$$

where $A^{Measured}$ is the asymmetry measured with the detector, A^{PV} is the true physics asymmetry, and ΔS is the spot size asymmetry. The coefficient α can be experimentally determined by comparing the widths of the distributions of the hybrid asymmetries

$$J_+ \equiv A^{Measured} + \eta \Delta S \tag{3.10}$$

and

$$J_- \equiv A^{Measured} - \eta \Delta S. \tag{3.11}$$

The η term is an arbitrary scale factor inserted for dimensional concerns, and also functions to make the detector and wire array contributions to $J_\pm$ roughly the same size. In the absence of spot size sensitivity, the width of the distributions of J_+ and J_- would be the

same. The degree to which they differ determines the size of α through

$$\alpha = \frac{\sigma^2_{J_+} - \sigma^2_{J_-}}{4\eta\sigma^2_{\Delta S}}. \tag{3.12}$$

Figure 3.14 depicts the spot size sensitivity determined with this method for each detector[3], for both Run 1 and Run 2. Because the coefficients differ among the detectors, the sensitivity is dominated by geometry rather than a common effect, such as spot size induced target density fluctuations. In all cases, the magnitude of the sensitivity is greater in Run 1 than Run 2, most likely due to different beam tunes.

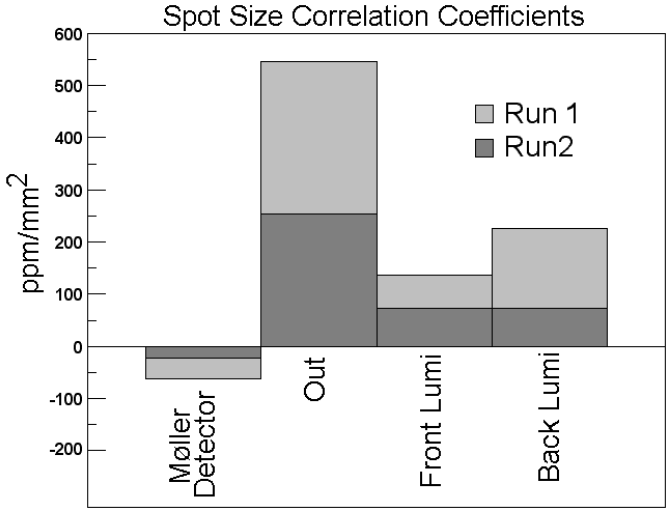

Figure 3.14: Detector spot size correlation coefficients.

The coefficients can be combined with the helicity-correlated spot size differences measured with the wire array to produce the systematic uncertainty due to spot size on the asymmetry measured with the detectors. Tables 3.4 and 3.5 detail the computed uncertainties for Run 1 and Run 2.

The third column in the tables represents the contribution to the asymmetry measured

[3]The luminosity monitor is a low-angle detector used for a null-asymmetry measurement. It is described in Chapter 5.

Detector	α (ppm/mm^2)	Average Spot size Asymmetry $< \Delta S >$ (10^{-6}mm^2)	Systematic Uncertainty Estimate $\alpha < \Delta S >$ (ppb)
Møller	-61 ± 4	5.5 ± 6.9	-0.3 ± 0.4
Out	546 ± 17		3.0 ± 3.8
Front Lumi	138 ± 6		0.8 ± 1.0
Back Lumi	227 ± 9		1.2 ± 1.6

Table 3.4: Run 1 systematic uncertainty on A^{PV} due to spot size.

Detector	α (ppm/mm^2)	Average Spot size Asymmetry $< \Delta S >$ (10^{-6}mm^2)	Systematic Uncertainty Estimate $\alpha < \Delta S >$ (ppb)
Møller	19 ± 3	-3.7 ± 25.2	-0.2 ± 0.5
Out	253 ± 32		-0.9 ± 6.4
Front Lumi	72 ± 8		-0.3 ± 1.8
Back Lumi	73 ± 7		-0.3 ± 1.8

Table 3.5: Run 2 systematic uncertainty on A^{PV} due to spot size.

with the detectors due to spot size. Because $\alpha < \Delta S >$ is consistent with zero in all cases, the uncertainty on this number will be used as the estimate for the spot size systematic uncertainty for the detectors. The Run 2 uncertainty is larger because the wire array was inserted for less data compared to Run 1.

3.5 Skew Quadrupole Magnet

The emission of synchrotron radiation traversing the A-Line bend leading up to the experimental hall has the effect of actually improving the quality of the beam in the horizontal direction [40]. Higher energy electrons emit more radiation while lower energy electrons emit less, pushing all electrons toward the average energy. Because virtually all of the bends are in the horizontal plane, there is no enhancement for the vertical beam parameters.

The E158 experiment introduced a skew quadrupole magnet near the end of the A-Line to mix the vertical and horizontal beam parameters. The location of the magnet is depicted in Figure 3.15. The skew quad is a standard quadrupole magnet rotated around the beamline by 45^o. By mixing the horizontal and vertical beam parameters, the overall

quality of the beam is improved.

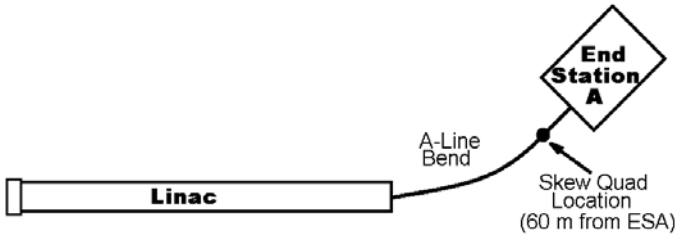

Figure 3.15: Location of skew quadrupole magnet.

Figure 3.16 presents the effect of the skew quad on the detector asymmetry distributions. The width of the distribution is the resolution of the detector. The presence of the skew quad dramatically improves the resolution of the luminosity monitor and the Out detector, while having little effect on the Møller detector.

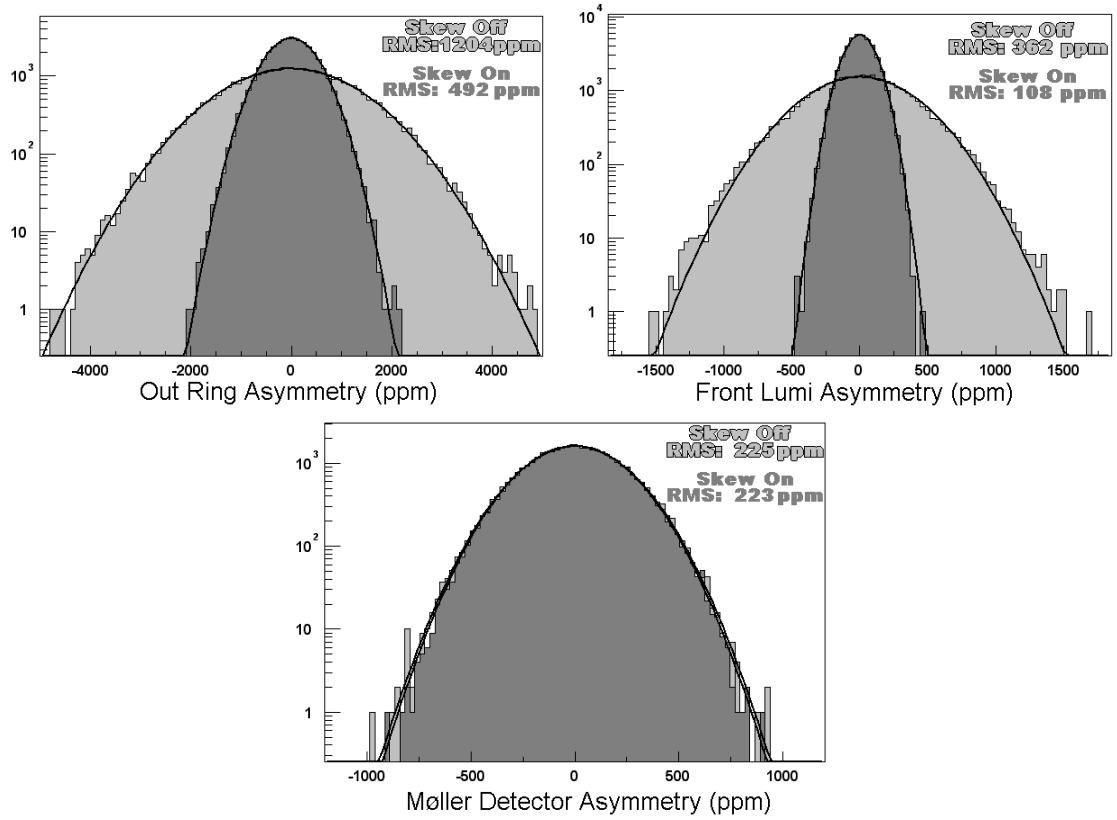

Figure 3.16: Effect of the skew quad on detector resolution.

The presence of the skew quad was not found to affect the beam position jitter or energy

jitter in any discernible way. The resolution enhancement for the Out and lumi detectors is likely a geometric effect related to the beam divergence.

3.6 Liquid Hydrogen Target

The E158 target is a 1.5-meter-long cylinder of liquid hydrogen [41]. Hydrogen was chosen because the background electron-proton scattering events are more easily separated and modeled than for other targets.

The hydrogen in the target is maintained at a temperature of 20 K. The density is 0.07 g/cm^3, making the target 0.17 radiation lengths. The hydrogen is continually pumped around the target loop at 10 m/s, to minimize density changes due to heating by the primary beam. Mesh discs are positioned in the target cell, out of the path of the beam, to induce turbulent flow and further reduce potential density fluctuations. Figure 3.17 depicts the components of the target loop.

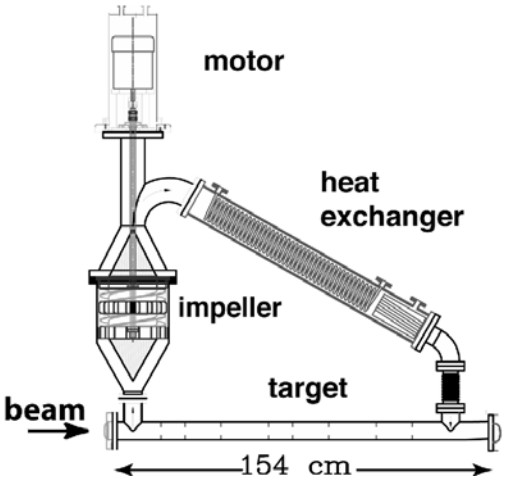

Figure 3.17: E158 cryotarget loop.

The hydrogen is cooled by 14 K helium gas flowing through the heat exchanger. The helium is provided by a refrigerator located in a building adjacent to End Station A. The loop

itself is wrapped in 30 layers of aluminized Kapton, to minimize heating due to radiation.

The entire loop sits inside a vacuum chamber, depicted in Figure 3.18. The chamber is large enough to allow the entire target loop to be retracted out of the beamline.

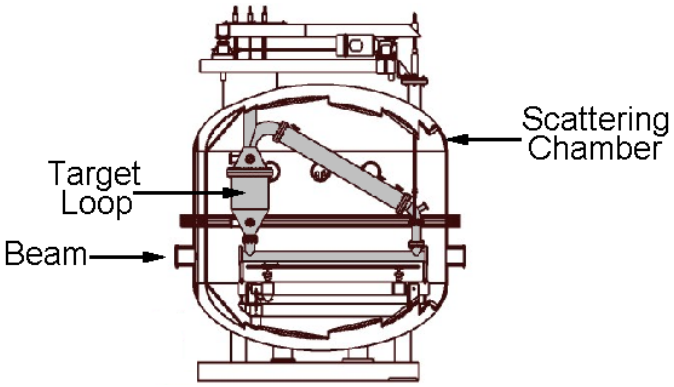

Figure 3.18: Cryotarget scattering chamber.

The electron beam deposits 700 W of power in the target for the highest current and repetition rate used by the E158 experiment. The temperature of the target is stabilized through an adjustable heater located at the end of the heat exchanger [42]. The target control program automatically monitors the beam current and rate, and adjusts the heater to maintain stable running.

The target loop contains 55 liters of hydrogen, with 25 liters in the target cell. The full loop has an explosive yield equivalent to 8 kg of TNT, a serious safety concern. The target loop is equipped with burst-discs which rupture when the target loop pressure exceeds safe running conditions. The hydrogen is then directed out of the End Station roof through a 100 mm wide pipe. The target vented in this manner several times over the course of the experiment (usually due to trouble with the refrigeration) and the safety systems worked flawlessly. The scattering chamber is also equipped with a 160 mm wide pipe to vent the hydrogen out the roof of ESA in the unlikely event of a rupture in the target loop itself. This catastrophic failure mode never occurred.

3.7 Spectrometer

The E158 spectrometer is used to separate the Møller scattered electrons from backgrounds. It is composed of a set of three dipole magnets followed by a package of four quadrupole magnets. The spectrometer stretches roughly half of the length of End Station A, as can be seen in Figure 3.19.

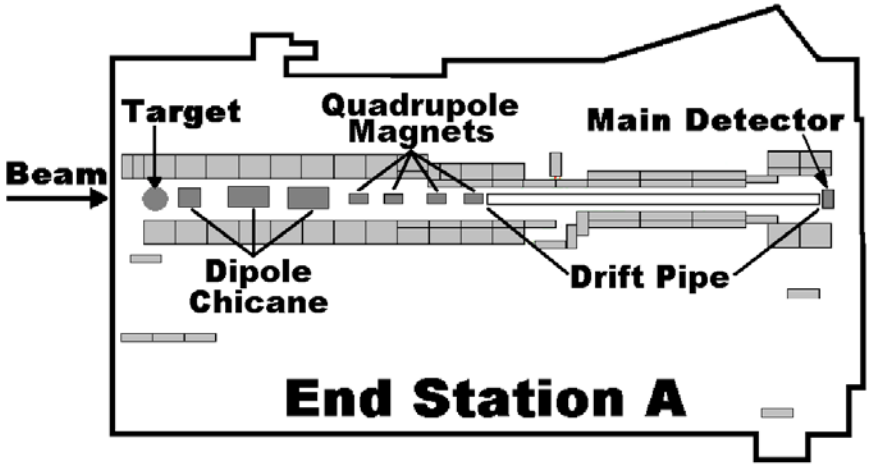

Figure 3.19: E158 spectrometer overview.

The design of the spectrometer is closely related to the geometry of the E158 calorimeter (Section 4.1). Figure 3.20 depicts the face of the detector.

The calorimeter is divided into four annular regions designated In, Mid, Out, and eP. The inner three regions are dominated by Møller scattered electrons and are used in the primary measurement of A^{PV}. The outer region is dominated by electron-proton scatters and is used for a supplementary measurement. All four regions are collectively called the E158 calorimeter.

3.7.1 Dipole Chicane

The primary purpose of the dipole chicane is the collimation of background bremsstrahlung photons. For the peak beam power of 500 kW, the target produces an 85 kW photon

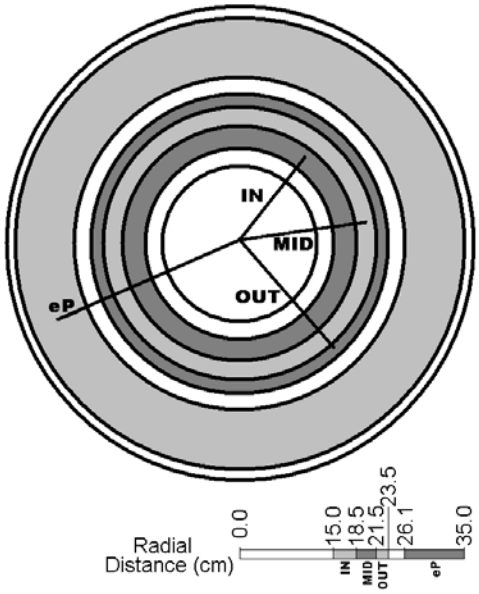

Figure 3.20: Regions of the E158 calorimeter.

beam. The power level of the photon beam is too high to block with material. Instead, two collimators are employed to keep the E158 calorimeter out of the line of sight of the target. The unblocked photons travel with the unscattered primary beam electrons to the beam dump out the east side of End Station A. Figure 3.21 depicts a 12 GeV scattered electron and a target photon traversing the chicane.

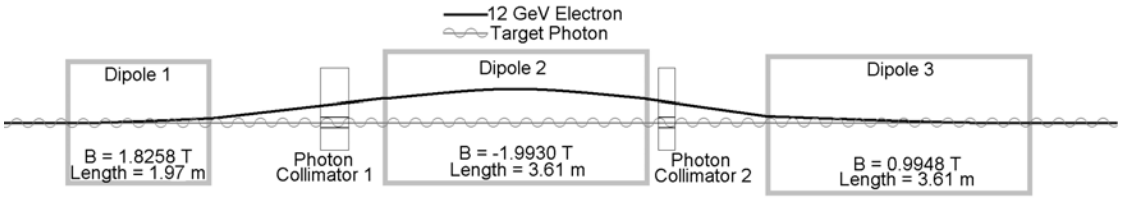

Figure 3.21: E158 dipole chicane.

The photon collimation is provided by two tungsten cylinders located between the dipole magnets. Figure 3.22 depicts the first of these collimators; the second is similar.

The chicane magnet strengths are chosen such that the integral of the transverse magnetic field over the path of a particle is zero, making it an achromat. Charged particles emerge from the chicane along their initial trajectory, ensuring that the shape of the scat-

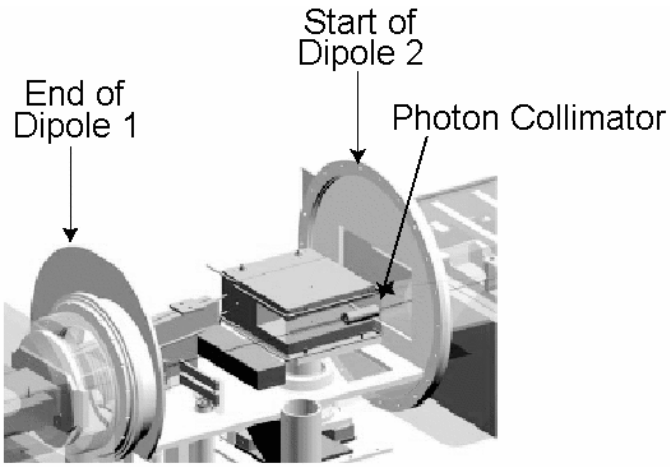

Figure 3.22: First photon collimator.

tered electron flux is unaffected by the presence of the magnets.

3.7.2 Main Acceptance Collimator

The main acceptance collimator is located between the end of the dipole chicane and the beginning of the quadrupole package. The collimator acts in conjunction with the quadrupole magnets to provide the separation of the Møller and eP scattered electrons. Figure 3.23 depicts the collimator, looking down the beamline. The flaring of the collimator edges is done to minimize edge scattering. The collimator is 12 cm thick of copper, followed by 3 cm of tungsten, representing forty radiation lengths of material.

The primary beam and the signal flux of the luminosity monitor pass through the central hole of the collimator. The Møller and electron-proton scatters observed with the E158 calorimeter pass through the outer semi-circular holes. Figure 3.24 depicts the signal flux at the calorimeter with and without the collimator in place. Note that the shape of the distributions is greatly influenced by the quadrupole magnets, discussed in the following section.

The In, Mid, and Out regions of the E158 calorimeter are located between radii of

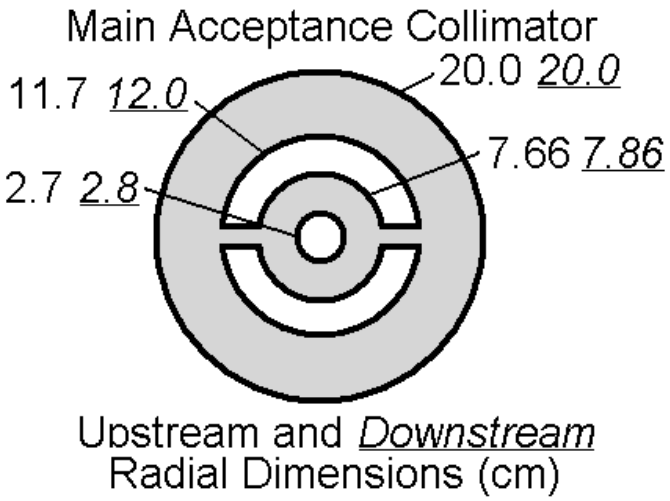

Figure 3.23: Main acceptance collimator.

15 cm and 23.5 cm. With the collimator in place, these portions of the calorimeter are dominated by the Møller scattered electrons between the energies of 12 GeV and 24 GeV. The eP detector is positioned between 26.1 cm and 35 cm, where the signal is dominated by electron-proton scatters.

3.7.3 Quadrupole Magnets

The quadrupole magnets shape the signal distribution that passes through the main acceptance collimator to separate the electron-electron and electron-proton scattering events. Figure 3.25 presents data scans performed with the profile detector (Section 4.3). The results demonstrate the size of the signal flux at the E158 calorimeter with and without the quadrupole magnets energized.

When the magnets are off, all of the electrons go to the eP detector. When the quadrupoles are on, the lower energy Møller scattered electrons are focused onto the In, Mid, and Out regions of the detector. Comparing quads-on and quads-off data with the Monte Carlo simulation provides a powerful calibration of the model of the E158 spectrometer.

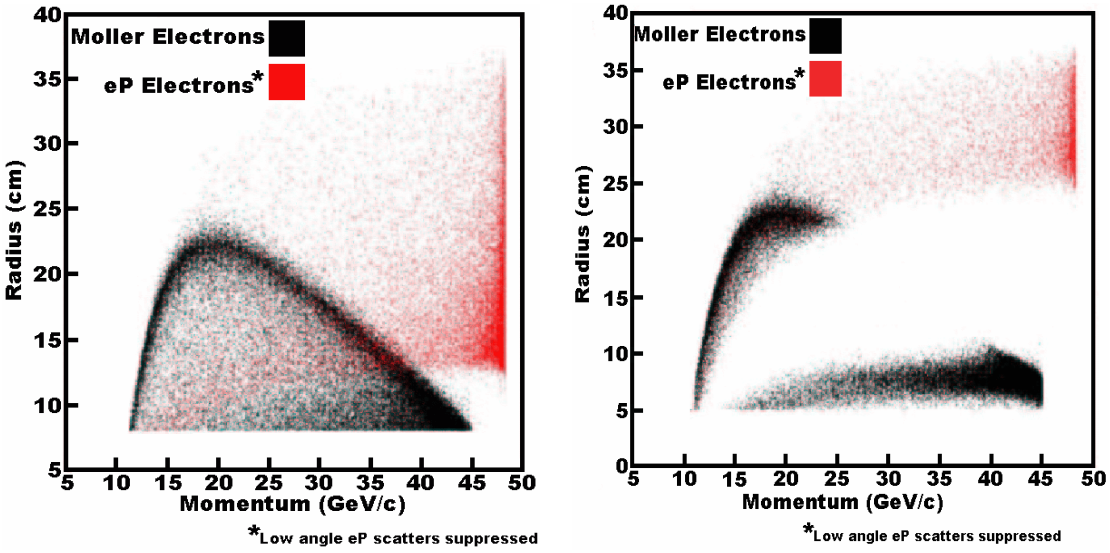

Figure 3.24: Effect of main acceptance collimator on signal flux.

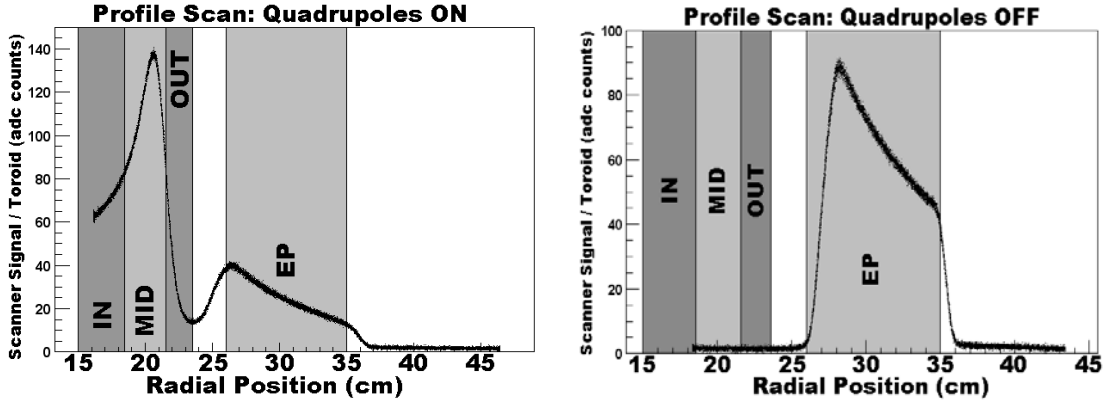

Figure 3.25: Profile scans with and without quadrupole magnets.

The simulation (Section 6.7.1) is crucial for estimation of the background electron-proton events in the In, Mid, and Out detectors.

3.7.4 Insertable Acceptance Collimator

An additional collimator is mounted on rails next to the main acceptance collimator. It can be remotely inserted or withdrawn when required. It functions to decrease the size of the acceptance of the main collimator, providing better separation between the Møller

and proton scattered electrons. The trade-off is that the amplitude of the overall signal flux is greatly reduced. The collimator is inserted for applications that do not require high statistics, such as polarimetry. Figure 3.26 is a photograph of the insertable collimator, with the main acceptance collimator visible in the background.

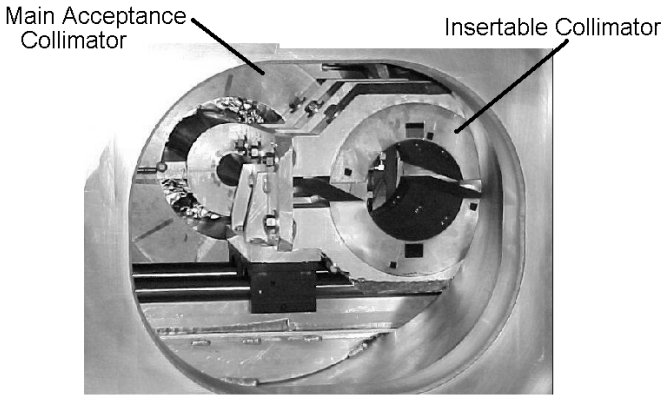

Figure 3.26: Insertable acceptance collimator.

The large openings at the top and bottom of the insertable collimator are used for polarimetry. The four smaller openings are used for background studies useful for fine-tuning the Monte Carlo simulation.

Figure 3.27 depicts the change in the scattered electron profile with the insertable collimator in the beam. The left plot is a vertical scan, observing flux from the large lower hole of the collimator. The separation between the Møller and proton scattered electrons is cleaner than when the collimator is removed, shown in the plot on the right. The vertical scale on the right plot has been normalized to match the conditions of the left plot, making apparent the signal suppression with the insertable collimator in place.

3.7.5 eP Collimator

The asymmetry in the electron-proton flux that enters the eP detector is an order of magnitude larger than A^{PV}. A simulation of showering in the E158 calorimeter demonstrates

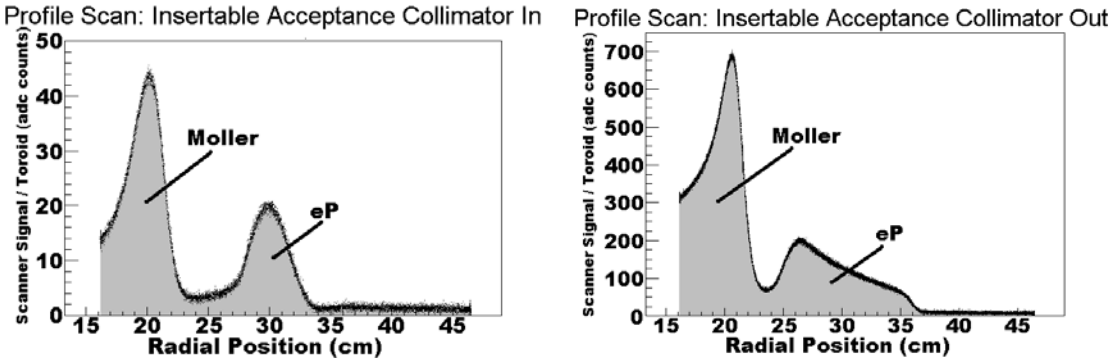

Figure 3.27: Profile scans with (left) and without (right) the insertable collimator.

that shower leakage from the eP detector into the other regions of the detector can be an important effect [43]. Shower leakage accounts for 35% of the eP background in the Out detector, with roughly 15% in the Mid and In regions.

To reduce the influence of the background, the eP collimator was installed between Run 1 and Run 2 to block completely the eP detector, as well as 75% of the Out detector. The collimator is composed of lead, 22.86 centimeters thick. It is a "clamshell" design, with halves that are remotely insertable and removable. Figure 3.28 presents an overhead view of the detector area, including the eP collimator, while Figure 3.29 depicts the coverage of this collimator on the face of the E158 calorimeter.

Though the majority of the Out detector is blocked, its signal is only degraded by 25% due to the eP collimator. The bulk of the Out signal resides at lower radii, and the Out ring has some shower sharing with the Mid ring. Figure 3.30 presents data from profile scans with and without the eP collimator in place. It is clear that the collimator effectively blocks the flux of the eP detector.

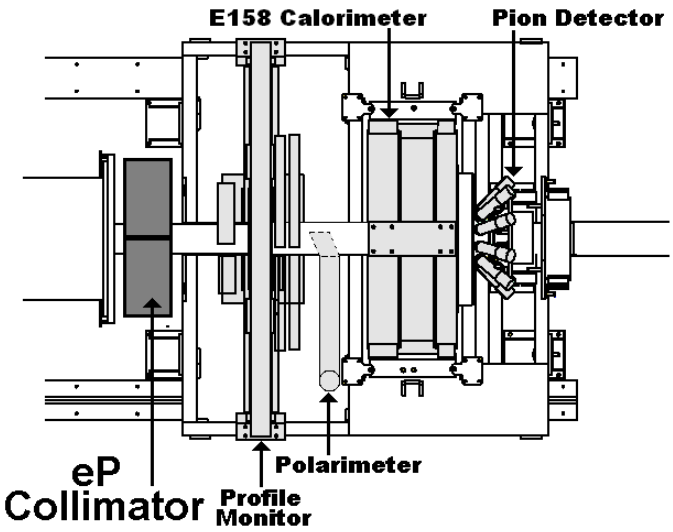

Figure 3.28: Insertable eP collimator, top view.

3.7.6 Synchrotron Collimation and Photon Masks

A background of synchrotron photons is produced by the bends in the dipole chicane. For the highest beam current and rate, the synchrotron radiation from the final dipole magnet (D3) is 115 W, of which approximately 10% is directed at the E158 calorimeter [44]. The energy in the synchrotron radiation intersecting the calorimeter is comparable to the energy contained in the total electron signal flux. The synchrotron radiation represents a sizable dilution to the main signal, but the primary concern is that it can introduce a helicity-correlated asymmetry of its own, several orders of magnitude greater than A^{PV} [45].

The synchrotron background is decreased by three sets of collimators. The first is provided by 40 radiation lengths of material in the spokes of the main acceptance collimator, seen in Figure 3.23. The second is a similar pair of spokes, comprised of 20 radiation lengths of tungsten, installed after the final quadrupole magnet. The final collimators are also spokes of 20 radiation lengths of tungsten, bolted directly to the face of the detector. The final two sets of synchrotron collimators are visible in Figure 3.31. The collimators reduce the synchrotron signal to 0.15% of the electron signal in the E158 calorimeter.

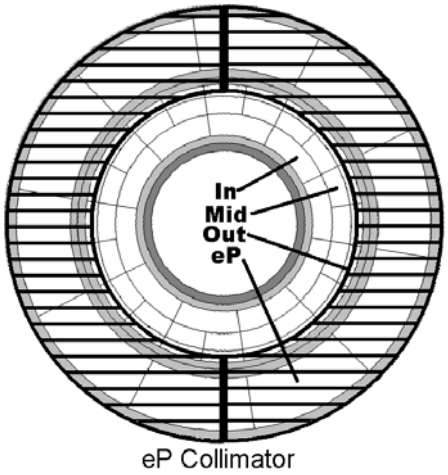

Figure 3.29: The hatched area represents the coverage of the eP collimator on the face of the E158 calorimeter.

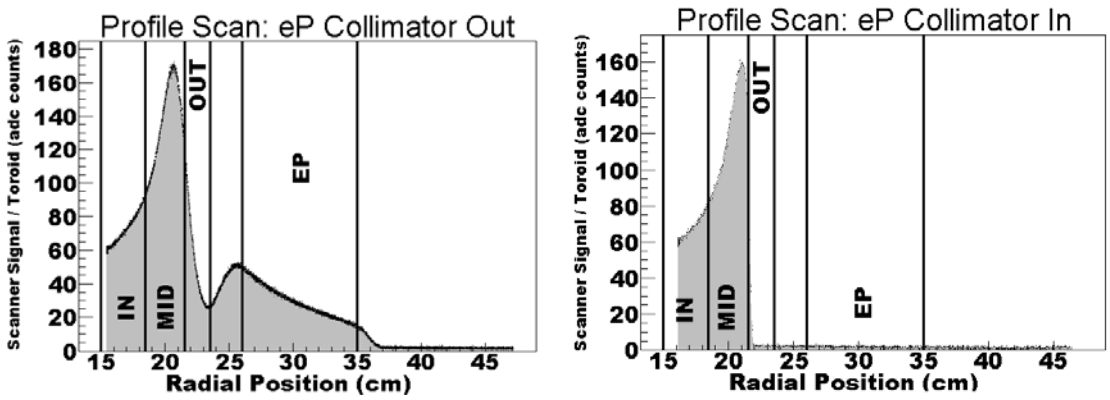

Figure 3.30: Profile scans without (left) and with (right) the eP collimator in place.

The final set of collimators are 7 tungsten rings located inside the drift pipe upstream of the E158 calorimeter (Figure 3.31). These are used to block photons scattered from the photon collimators between the dipole magnets. The rings were installed after the initial engineering run of the experiment, before the beginning of Run 1. The resolution of the Møller detector improved from 500 ppm to 200 ppm between Run 0 and Run 1, due to the tungsten rings blocking this background.

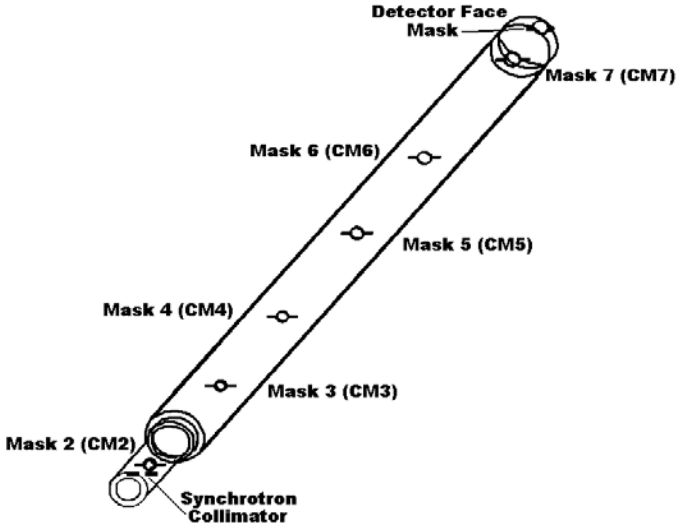

Figure 3.31: Drift pipe synchrotron and photon collimators.

Chapter 4

Detectors

The data from the E158 experiment is used to determine a single quantity: the parity-violating asymmetry in Møller scattering. However, the measurements of many different detectors contribute both directly and indirectly to the final result. Figure 4.1 depicts the locations of the detectors in End Station A. Most of the devices are mounted to a movable cart, depicted in Figure 4.2. The following sections give descriptions of the E158 detectors and their roles for the experiment[1].

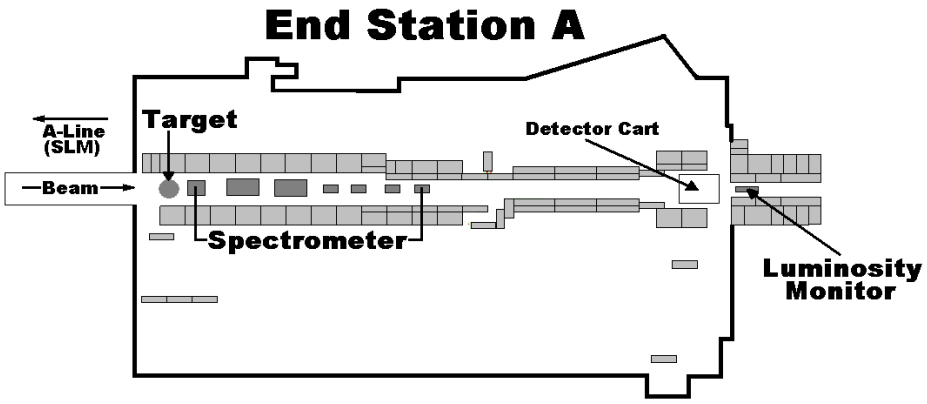

Figure 4.1: Overhead view of the detector locations in End Station A.

[1]The luminosity monitor was the primary responsibility of the author and is covered separately in Chapter 5.

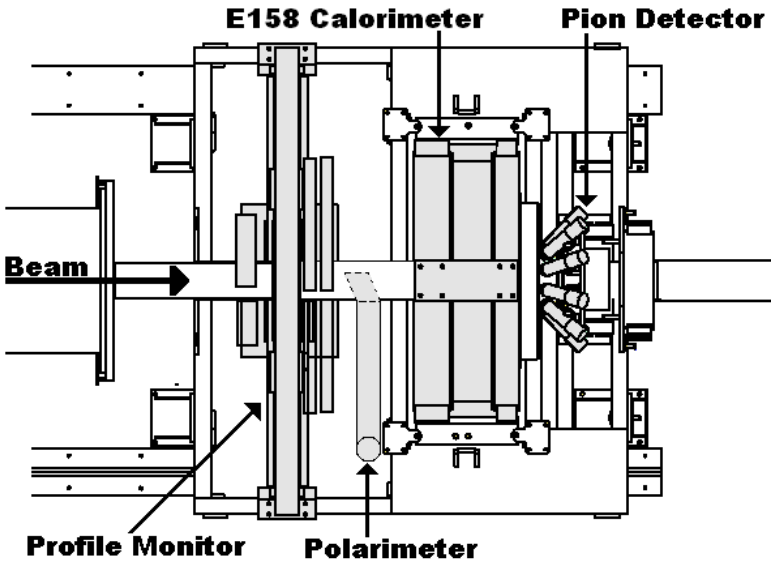

Figure 4.2: Overhead view of the movable detector cart.

4.1 E158 Calorimeter

The E158 calorimeter is the primary detector of the E158 experiment [46]. It is divided into four separate annular regions, denoted as the In ring, Mid ring, Out ring, and eP detector. The spectrometer (Section 3.7) focuses electrons scattered from the target so that the In, Mid, and Out regions are dominated by Møller scattering, while the eP detector is dominated by electron-proton scatters.

The In and Mid region are collectively known as the Møller detector, and provide the primary measurement of A^{PV}. The Out ring could also have been included, but Section 6.7.2.2 will demonstrate that it was found to be susceptible to large systematic effects. The eP detector supplements the Møller detector by providing information on the background electron-proton scattering events.

4.1.1 Calorimeter Design

The calorimeter is mounted on the movable detector cart located in End Station A (Figure 4.2). It is 16 radiation lengths thick, chosen as a compromise between large signal size and minimizing sensitivity to the pion background. The calorimeter is composed of 100 copper plates interspersed with quartz fibers. The three inner regions are 10% quartz by volume, while the eP detector is 2%. Electrons shower in the copper and produce Cherenkov light in the quartz, which is then directed through light guides to photomultiplier tubes (PMTs) for detection. The Cherenkov angle in quartz is close to 45°, so the plates and fibers are positioned at this angle to maximize light collection efficiency. The resulting geometry is depicted in Figure 4.3. The In, Mid, and Out rings make up the dark inner region while the eP detector is the light outer region.

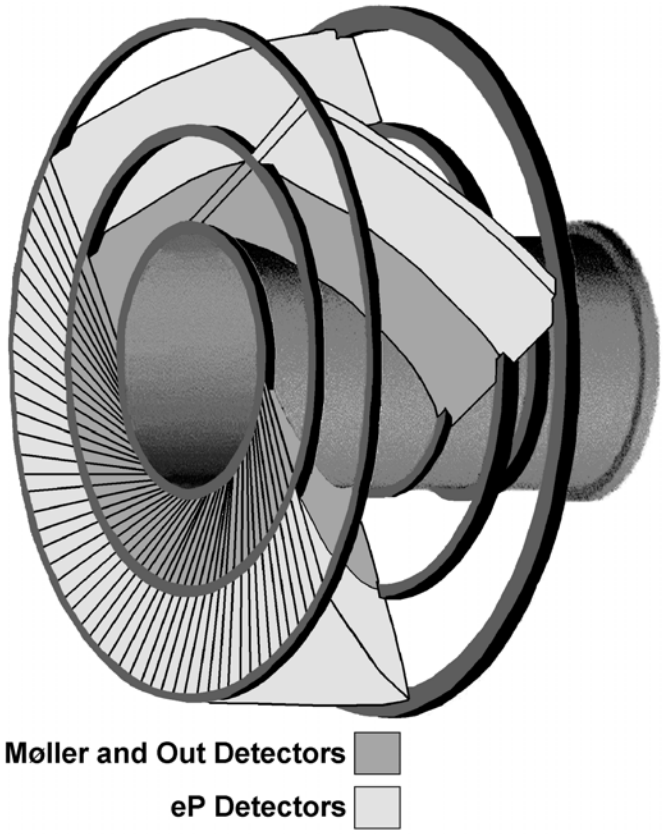

Figure 4.3: Partially constructed E158 calorimeter.

The quartz fibers are bundled to divide the calorimeter into the four concentric zones. Each region is further subdivided with bundles of fibers servicing separate photomultiplier tubes. Figure 4.4 depicts the different regions of the detector. The In and eP rings are serviced by 10 tubes, while the Mid and Out rings have 20 tubes.

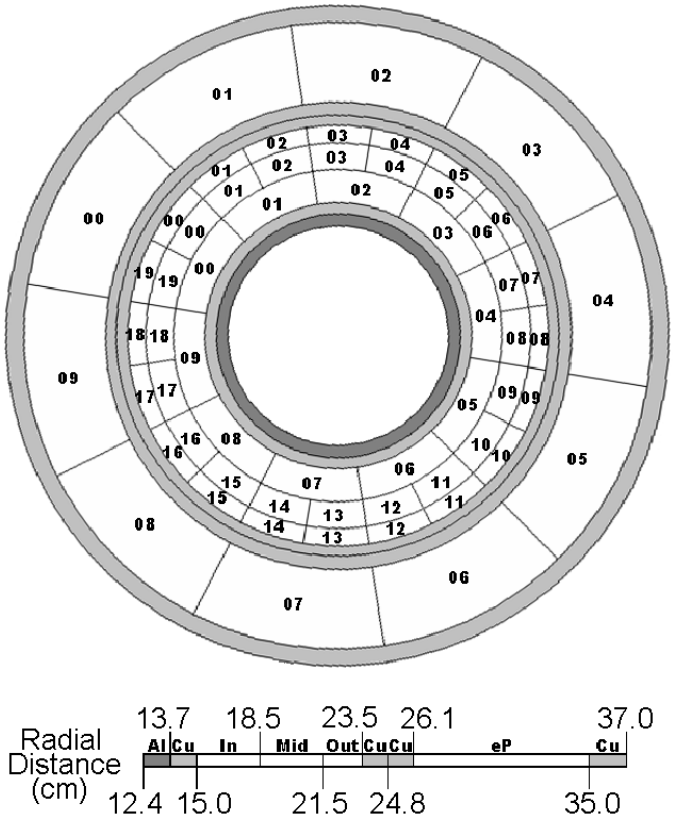

Figure 4.4: Calorimeter channel map.

To protect the PMTs from radiation damage, they are located roughly 70 cm from the beamline. The 60 light guide periscopes that direct the Cherenkov light from the calorimeter to the PMT locations are shown in Figure 4.5.

The PMTs are also encased by a large slab of lead for further protection. Figure 4.6 presents a diagram of the lead shielding. The PMTs are positioned in the cylinders drilled in the back shield. The two rows of PMTs are located at radial distances of 67.3 cm and 75 cm. Over the course of the experiment, the E158 calorimeter absorbed a radiation dose

Figure 4.5: Light guide configuration.

of approximately 500 MRad, while the PMT dose was only ∼1 Rad.

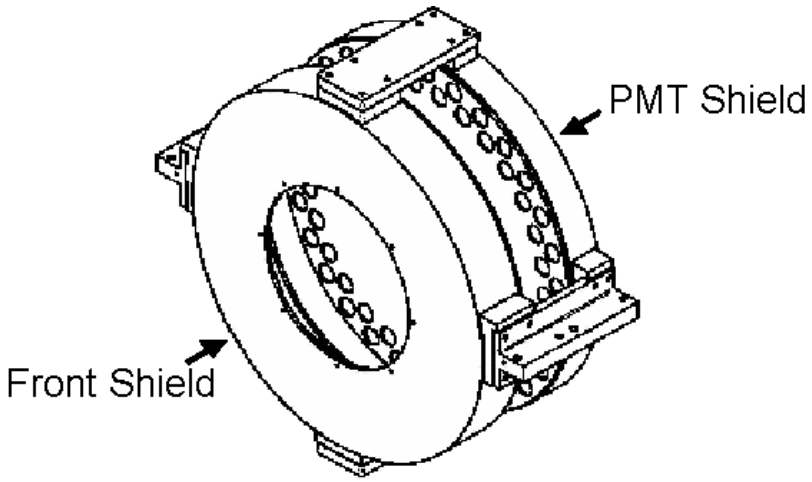

Figure 4.6: E158 calorimeter lead shielding.

4.1.2 Calorimeter Electronics

The electronics for the E158 calorimeter are depicted in Figure 4.7 [47]. The RLC circuit is employed to increase the length of the signal from the PMTs. The longer time constant allows the ADCs (analog-to-digital converters) to integrate for a longer period of time,

suppressing random noise. Employing this method, it was found that the ADCs had only one to two counts of noise, compared to the full range of 64,000 counts.

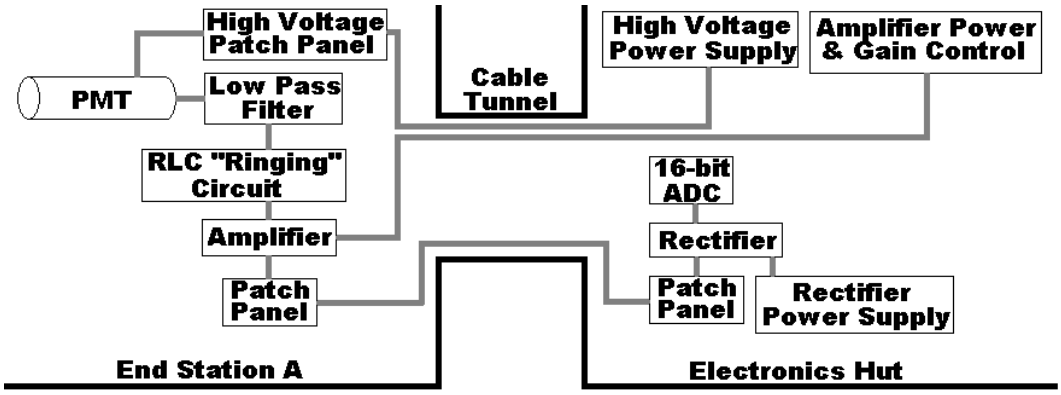

Figure 4.7: E158 calorimeter electronics diagram.

The power supplies and ADCs are located in the electronics hut, which is accessible at all times. The hut is connected to the End Station through 200 feet of cable laid in an underground tunnel. The amplifiers are located in the End Station near the detector to avoid amplifying pick-up noise from the cables.

4.1.3 Calorimeter Resolution

The asymmetry resolution of the Møller detector is the dominant contributor to the overall uncertainty on the measured value of A^{PV}. Because of the large cross section for Møller scattering, the detector receives a signal of $\approx$ 20 million scattered electrons for a beam current of 5×10^{11} electrons. The counting statistics contribute roughly 160 parts-per-million (ppm) to the resolution of the detector. Additionally, common-mode electronics noise contributes 110 ppm to the resolution, so that the overall resolution is near 200 ppm. Figure 4.8 depicts the Møller detector asymmetry distribution for a standard one-hour data run. The correlation of the detector with the beam monitors has already been removed through the regression process, covered in Section 6.3.

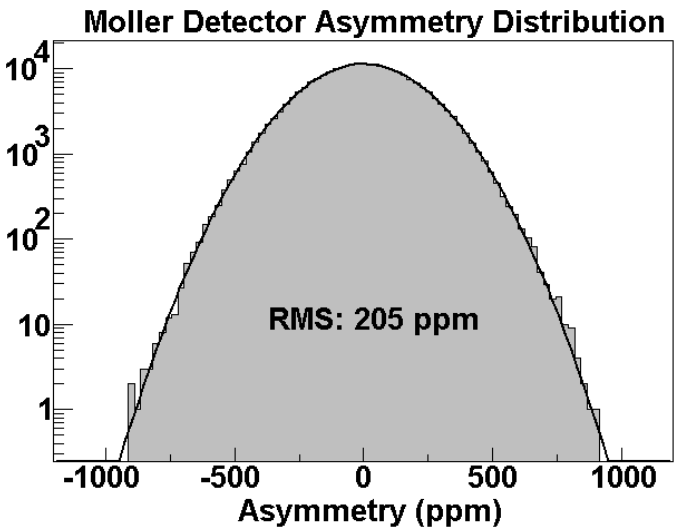

Figure 4.8: Møller detector asymmetry resolution.

The Out detector receives an additional four to seven million Møller electrons (depending on whether the insertable eP collimator is in or not). If the Out detector is included with the In and Mid regions, the detector resolution improves slightly, as seen in Figure 4.9. Because of its large systematic susceptibility and only marginal resolution gain, the Out detector is not included in the measurement of A^{PV}.

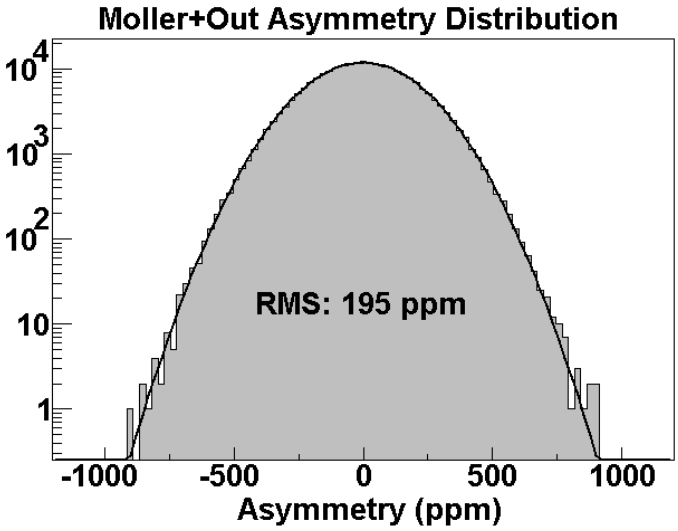

Figure 4.9: Møller plus Out ring asymmetry resolution.

The eP ring is dominated by electron-proton scatters, and is used to measure the parity-

violating asymmetry in this background. Figure 4.10 depicts the eP detector asymmetry distribution. The resolution of the eP detector is adequate to perform its function, which will be covered in Section 6.7.1.

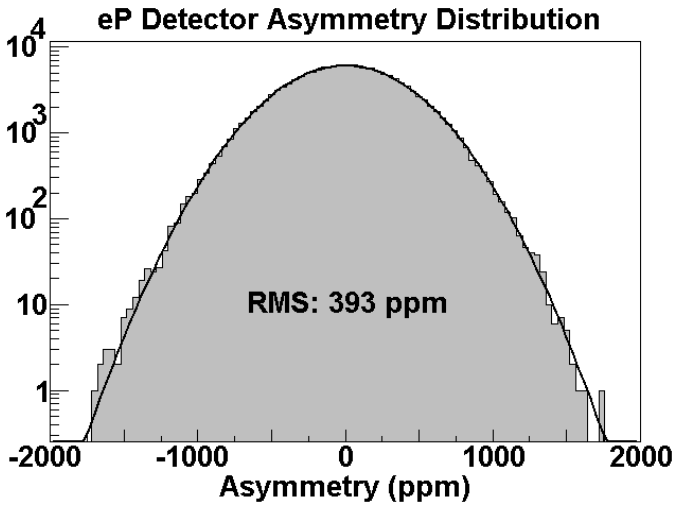

Figure 4.10: eP ring asymmetry resolution.

4.1.4 Calorimeter Linearity

A non-linear response can introduce an error between the asymmetry observed with the detector $A^{Measured}$ and the physics asymmetry A^{PV}. Section 5.10.1 demonstrates that the shift introduced by the non-linearity ϵ of the detector is given by

$$A^{Measured} = (1 - \epsilon)A^{PV} - \epsilon A^{Toroid}, \tag{4.1}$$

where A^{Toroid} refers to the charge asymmetry of the beam measured with a toroid.

The regression procedure is employed to reduce the detector's sensitivity to beam parameters, including the charge asymmetry, effectively removing the ϵA^{Toroid} term in Equation 4.1. The remaining $(1 - \epsilon)A^{PV}$ term is a source of systematic uncertainty. Because A^{PV} is $\approx$ -150 ppb, it is important to keep ϵ at the level of 1% to insure that the systematic

Run I	
Ring	Linearity
In	0.996 ± 0.013
Mid	0.986 ± 0.010
Out	0.995 ± 0.012

Run II	
Ring	Linearity
In	0.994 ± 0.012
Mid	0.989 ± 0.009
Out	1.009 ± 0.011

Table 4.1: Measured linearity of the In, Mid, and Out rings of the E158 calorimeter, for Run I and Run II.

uncertainty is only a few ppb.

The linearity of the calorimeter was constrained by comparing the observed value of a large asymmetry measured at multiple PMT input light levels [48]. The asymmetry was provided by the iron foil used for polarimetry, described in Section 4.2. The foil was inserted simultaneously with the liquid hydrogen target so that the signal flux was nearly the same as during normal production running. Filters were placed in front of some of the PMTs, reducing the light level to 1/3 or 1/2 of the signal seen during normal running. By comparing the asymmetry recorded by each class of PMT, it is possible to determine the linearity. Linearity of 100% would mean that all tubes would record the same asymmetry. Table 4.1 presents the Møller detector linearity found by this method in Run I and Run II. The results indicate that the detector non-linearity is at the 1% level, as required.

4.2 Polarimeter

The polarimeter is used periodically to monitor the polarization of the electron beam. Measurements are performed after each energy change and source halfwave plate toggle, corresponding roughly to one measurement every two days. In the absence of other backgrounds, the physics asymmetry A^{PV} is related to the asymmetry measured with the Møller

detector $A^{Measured}$ and the beam polarization P through

$$A^{PV} = \frac{A^{Measured}}{P}. \tag{4.2}$$

The uncertainty on P translates directly into an uncertainty on A^{PV}.

4.2.1 Polarimetry Method

The beam polarization measurement is performed in a special configuration of the E158 apparatus, with the liquid hydrogen target retracted and a supermendur foil placed in the beam [49]. The foil is magnetically polarized by a pair of Helmholtz coils which are only energized during the measurement. The insertable acceptance collimator, discussed in Section 3.7.4, is moved in, and the spectrometer quadrupole magnets are adjusted to provide better separation of the Møller and electron-proton scattering events. The polarimeter detector, described in the following section, is moved onto the Møller peak in the scattered flux, directly in front of the Møller detector.

The polarized foil produces a helicity-correlated asymmetry in the scattering rate, due to the magnetic dipole interaction [50]. The asymmetry A_m is related to the beam polarization P_{beam}, the target polarization P_{foil}, and the center-of-momentum scattering angle θ_{CM} through

$$A_m = \cos(20^\circ) P_{beam} P_{foil} \frac{(7 + \cos^2\theta_{CM}) \sin^2\theta_{CM}}{(3 + \cos^2\theta_{CM})^2}. \tag{4.3}$$

The coefficient of $\cos(20^\circ)$ is included to account for the angle of the foil with respect to the beam. The tree-level asymmetry calculation of Equation 4.3 is adequate because higher order corrections are found to be well below 1% [51].

The foil is comprised of 49% Cobalt, 49% Iron, and 2% Vanadium. All three of these

elements have two valence electrons that are polarized by the magnetic field, while the inner electrons remain unpolarized. The valence electrons account for roughly 8% of all electrons, so the maximum polarization of the foil is around 8%. Assuming a beam polarization of 75%, A_m is expected to be approximately 4%, over five orders of magnitude larger than A^{PV}.

Because the asymmetry is large, it can be measured in a relatively short period of time. To avoid excessive heating of the foil, runs are taken at a beam repetition rate of 10 to 15 Hz, compared to the normal rate of 120 Hz. For each measurement, data is taken for approximately 10 minutes, accumulating 5000 pulse pairs. Figure 4.11 presents the measured asymmetry distribution for a typical polarimetry run. While the statistical

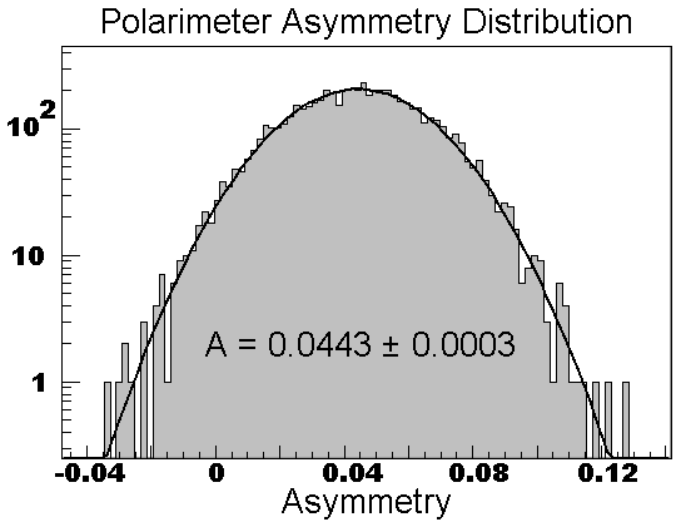

Figure 4.11: Polarimeter asymmetry distribution for a single run.

uncertainty on the measured asymmetry is small, the polarimetry systematic uncertainties covered in Section 4.2.3 dominate.

Immediately after each polarization run, data is taken with the foil removed, to serve as a background measurement. In total, each polarization measurement lasted approximately 30 minutes.

4.2.2 Polarimeter Design

The polarimeter is mounted on the detector cart between the profile monitor and the Møller detector, as shown in Figure 4.2. Figure 4.12 is a schematic of the detector looking downstream from the target.

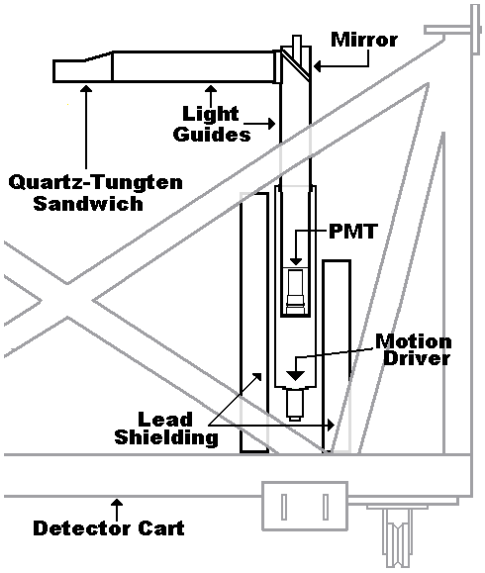

Figure 4.12: Polarimeter position on the detector cart.

The apparatus is remotely movable in the vertical direction. When not in use, the polarimeter is lowered to a radial distance of 50 cm so that it does not interfere with the electron flux entering the Møller detector. During a polarimetry measurement, the device is raised to a radial distance of 21 cm, the location with the highest rate of scattered Møller electrons.

Signal electrons create an electromagnetic shower in the polarimeter's quartz-tungsten sandwich, which is depicted in Figure 4.13 [52]. The shower creates Cherenkov light which is directed through a light guide to the photomultiplier tube that records the signal. The sandwich plates are angled at 30°, which simulations indicated was optimal for light collection. The extra tungsten plate at the front of the sandwich has only a minimal influence

Systematic Uncertainties	
Item	Uncertainty
Background Subtraction	3.0%
Foil Polarization	3.0%
Result Spread	2.5%
Polarimeter Linearity	1.5%
Foil Angle	1.0%
Foil Heating Depolarization	1.0%
Levchuk Effect [54]	1.0%
Analyzing Power	0.5%
Helmholtz Magnetic Field	0.2%

Table 4.2: Polarimetry uncertainties, relative to P_{beam}.

on the light yield, but serves to decrease sensitivity to low-energy backgrounds.

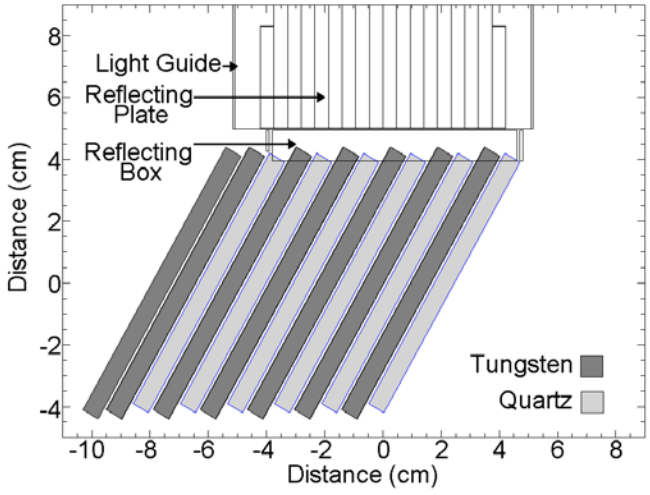

Figure 4.13: Quartz-tungsten sandwich of polarimeter.

4.2.3 Polarimeter Systematic Uncertainties

While the data acquired for each polarization measurement provides a statistical uncertainty well below 1%, there are many sources of systematic uncertainties also to consider. Table 4.2 itemizes each effect, which are covered in detail in Reference [53].

The contribution labeled "Result Spread" refers to the results obtained with different target foils. Three foils of differing thickness were available on the movable target chassis: 20 μm, 50 μm, and 100 μm. Each foil gave a different result for the polarization. The reason

for this behavior is unclear, so the spread in the results is submitted as a contribution to the systematic uncertainty.

The quadrature sum of all the items nets a total uncertainty of 5.5%, relative to P_{beam}. The beam polarization was typically around 84%, so this amounts to an absolute uncertainty of $\pm 4.6\%$ on the beam polarization.

4.2.4 Polarimeter Results

Figure 4.14 shows the polarization measurements spanning one month of Run II. The variation among the measurements is only a few percent, indicating that the beam polarization was fairly stable. The average polarizations used for computing the physics asymmetry were found to be

$$P_{beam} = 84.9\% \pm 4.6\% \tag{4.4}$$

for Run I and

$$P_{beam} = 84.4\% \pm 4.6\% \tag{4.5}$$

for Run II.

4.3 Profile Monitor

The profile monitor is used to measure the radial distribution of the scattered electrons entering the Møller detector. The signal flux maps are employed to fine-tune the Monte Carlo simulation of the E158 spectrometer, which plays a critical role in background estimation for the Møller detector measurements.

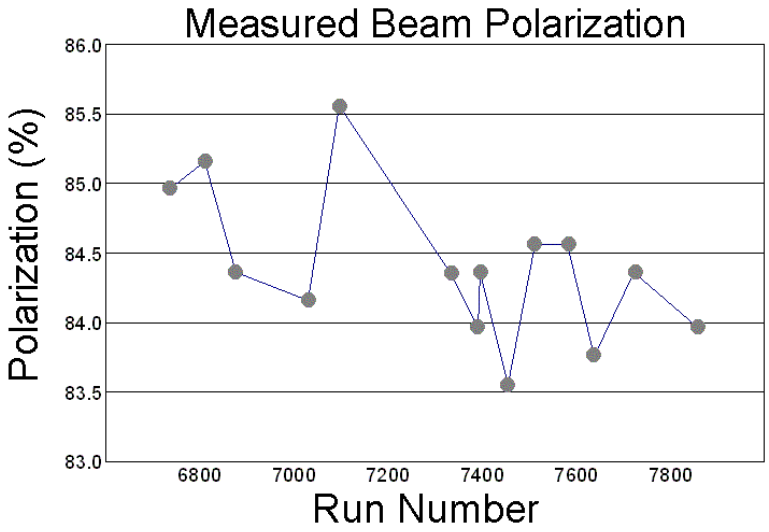

Figure 4.14: Run II beam polarization measurements, spanning 1 month.

4.3.1 Profile Monitor Design

Figure 4.2 shows the location of the profile monitor from overhead, while Figure 4.15 presents a schematic drawing of the device. The profile monitor is comprised of two of pairs movable Cherenkov detectors mounted to a rotatable annulus. The detectors can be moved radially from the beam pipe out to 50 cm, fully covering the extent of the E158 calorimeter. The annulus can be rotated over 180°, allowing radial scans at any angle. The scanners are cross-calibrated by comparing data taken 180° apart.

The Cherenkov detectors are mounted in pairs for background subtraction [55]. The signal from the front scanner is weighted and subtracted from the back scanner to produce a corrected signal. The front scanner utilizes only a quartz block, while the back scanner is also equipped with a tungsten preradiator. Figure 4.16 depicts one of the back scanners.

The shutter mounted in front of the PMT can be opened and closed remotely, for background studies. Additionally, the outer tube of the scanner is rotatable so that the tungsten preradiator can be removed for additional background measurements.

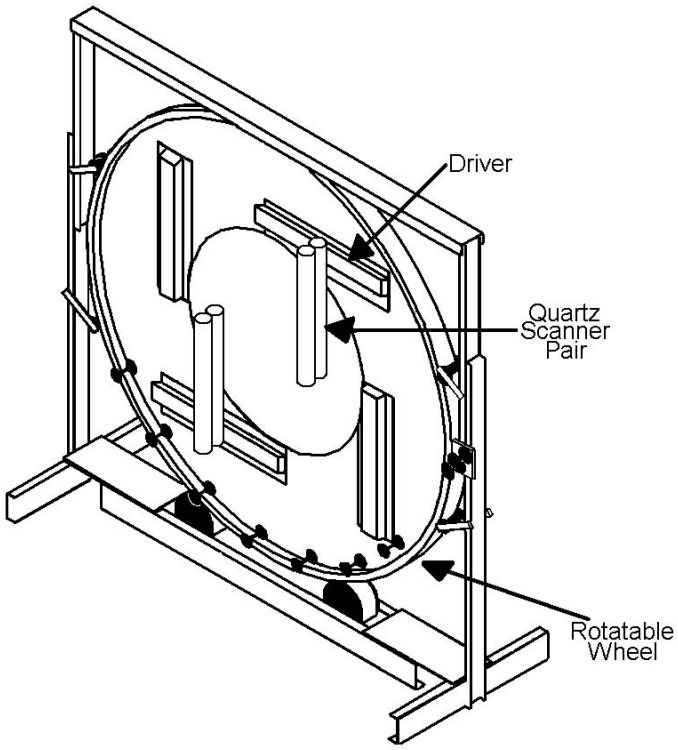

Figure 4.15: Profile monitor schematic.

4.3.2 Profile Scan Results

A profile scan consists of multiple radial scans over the full azimuth, in increments of 20°. A full scan required roughly 30 minutes of beam time. Figure 4.17 shows a typical radial scan at one particular angle. The Møller peak is at the left, and the electron-proton scattering peak is at the right. The use of profile scans for background subtraction is discussed in Section 6.7.1.

4.4 Pion Detector

Pion production in the target contributes a small background to the Møller scattering process. The parity-violating asymmetry A^{PV} is related to the asymmetry obtained from

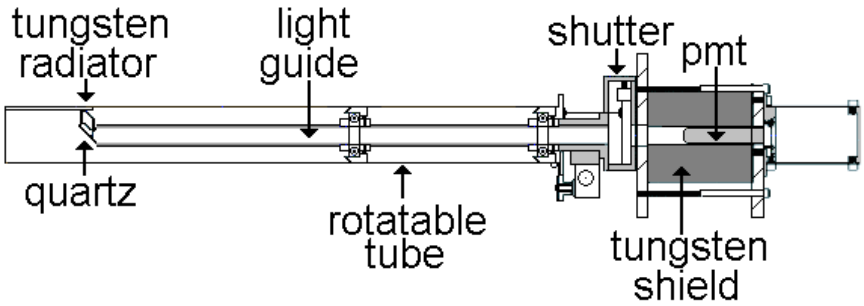

Figure 4.16: Quartz scanner schematic.

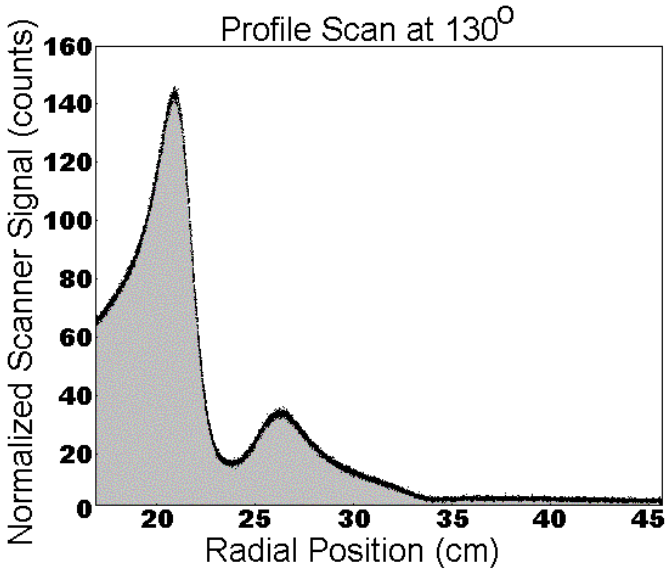

Figure 4.17: Radial scan produced with the profile monitor.

the Møller detector $A^{Measured}$ and the pion background through

$$A^{PV} = \frac{A^{Measured} - \frac{\epsilon N_\pi}{N_{ee}} A^\pi}{1 - \frac{\epsilon N_\pi}{N_{ee}} A^\pi}. \tag{4.6}$$

The term N_π/N_{ee} is the ratio of the number of pions to electrons passing through the Møller detector. The ϵ term refers to the average signal size produced by a pion in the Møller detector, compared to the average signal produced by an electron. The term A^π represents the parity-violating asymmetry of the pion background. The pion detector is utilized to determine A^π, as well as the ratio N_π/N_{ee}, while the remaining unknown ϵ must

be found from simulations of the Møller detector [56].

Pions are produced through real and virtual photoproduction, as well as deep inelastic scattering processes. Calculations indicate that the pion background passing through the Møller detector is likely to have an asymmetry at the level of 1 ppm, an order of magnitude higher than the Møller scattering asymmetry A^{PV} [37]. However, it is also found that the ratio N_π/N_{ee} is expected to be less than 1%. Sensitivity to the background is further suppressed because the Møller detector is less sensitive to pions than electrons. Simulations show that ϵ is 0.22 ± 0.15. Combining these factors, it is expected that the pion asymmetry correction to $A^{Measured}$ is less than 4 ppb, with a dilution factor less than 0.004.

4.4.1 Pion Detector Design

The pion detector is located directly behind the E158 calorimeter, shown in Figure 4.2. The lead PMT shield and active copper region of the Møller detector constitute 60 radiation lengths of material in front of the pion detector. The material ensures that the signal in the pion detector is dominated by pions, with little contamination from scattered electrons.

The detector is composed of 10 individual photomultiplier tubes, mounted symmetrically around the beam pipe. A quartz block is positioned in front of each tube, defining an active region for the detector between 15 cm and 23.5 cm, measured radially from beam center. This region exactly matches the extent of the three inner rings of the E158 calorimeter so that the two detectors observe the same pion flux. The tubes are mounted at 45° relative to the beam, to maximize Cherenkov light collection efficiency. Figure 4.18 depicts the pion detector looking downstream from the target.

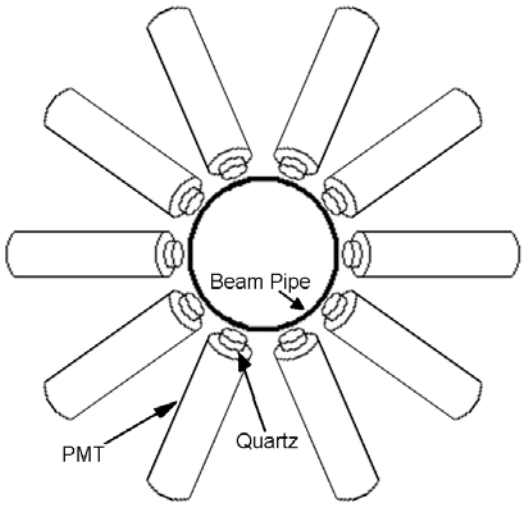

Figure 4.18: Pion detector layout.

4.4.2 Pion Detector Resolution

The required asymmetry resolution for the pion detector is set by the general goal that individual systematic uncertainties be kept below the level of 5 ppb. Because the correction due to the background pion asymmetry is expected to be less than 5 ppb for the Møller detector, it is acceptable to measure the pion asymmetry to $\pm$ 100% of its value, corresponding to a precision of $\approx$ 1 ppm. Since Run I and Run II are each composed of roughly 80 million pulse-pairs of data, the RMS of the pion detector asymmetry distribution is required to be less than 1 ppm$\times\sqrt{8 \times 10^7} \approx 0.01$.

Figure 4.19 presents the pion asymmetry distribution for a typical one-hour data run. The RMS of the distribution is a factor of two smaller than the required 0.01, indicating that the pion detector design is adequate for the experiment.

It should be noted that the resolution is 25 times less sensitive than the Møller detector. Because of its relative insensitivity, it was found that it was unnecessary to use the regression procedure to remove the correlation of the pion detector asymmetry to beam asymmetries: all of regression correlation coefficients were consistent with zero.

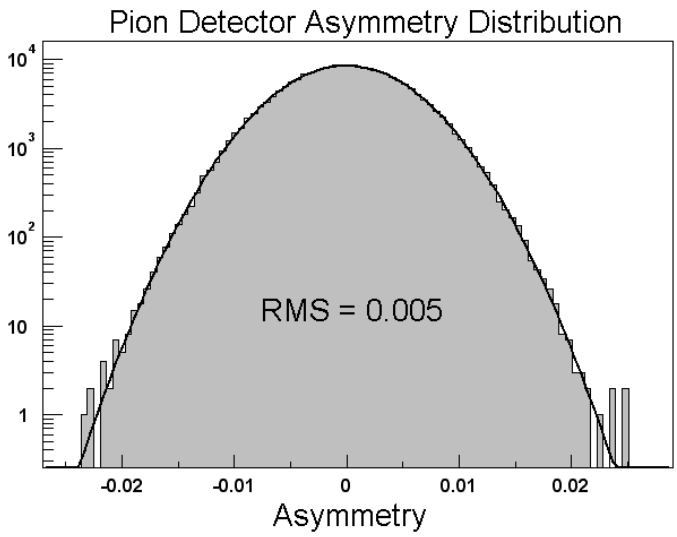

Figure 4.19: Pion detector asymmetry distribution, covering one run.

4.4.3 Pion Detector Electromagnetic Background

Though the pion detector is positioned behind 60 radiation lengths of material, it is still expected that Møller scattered electrons will contribute a small dilution to the pion signal. To measure the amount of contamination, special runs were taken with the polarimetry foil included with the liquid hydrogen target. The runs have a large, quickly measured, asymmetry. For these data, the Møller detector recorded an asymmetry of 522 ppm (with negligible uncertainty) while the pion detector measured an asymmetry of 62 ppm $\pm$ 11 ppm. Therefore, it is demonstrated that the electromagnetic contamination in the pion detector is only 13.5% $\pm$ 2.7%, which is small. The remaining signal in the pion detector is assumed to be pions.

4.4.4 Ratio of N_π to N_{ee}

The ratio N_π/N_{ee} was determined from two special runs. First, one of the pion detector tubes was placed in front of the Møller detector. Data was then taken using only the polarimetry foil as a target. The foil was unpolarized: it was used simply as a thin target,

so that the pion tube would not saturate. The tube was then moved back behind the Møller detector, and normal data was taken with the liquid hydrogen target. The signal attenuation provided by the Møller detector is related by

$$f^{Attenuation} = \frac{PMT_{LH2}^{Back}}{PMT_{Foil}^{Front}} \times \frac{Møller^{Foil}}{Møller^{LH2}}, \tag{4.7}$$

where the term $f^{Attenuation}$ designates the ratio of the signal flux at the front of the Møller detector to the signal at the front of the pion detector. The PMT terms refer to the signal size from the pion tube, while the Møller terms designate the signal size found by combining all of the tubes from the Mid ring of the Møller detector. The Møller ratio is included as a normalization, to account for the use of the different targets. It was found that $f^{Attenuation} = 2.003 \times 10^{-4} \pm 0.346 \times 10^{-4}$.

The attenuation number is compared with a GEANT3 simulation to extract the ratio N_π/N_{ee} [57]. The simulation is used to determine the value of

$$f^{Attenuation} = \frac{C_{ee}^{Back} + \frac{N_\pi}{N_{ee}} C_\pi^{Back}}{C_{ee}^{Front} + \frac{N_\pi}{N_{ee}} C_\pi^{Front}}. \tag{4.8}$$

Here the C terms refer to the size of the Cherenkov response of the pion detector. The $Back$ and $Front$ labels indicate the location of the pion tube, while ee and π refer to Møller electrons and pions, respectively.

Comparing the observed $f^{Attenuation}$ with the simulation yields

$$\frac{N_\pi}{N_{ee}} = 0.0063 \pm 0.0021. \tag{4.9}$$

The uncertainty is composed of the statistics of the real measurement, as well as a conser-

Pion Asymmetry A_π	
Run I	-1.74 ± 0.46 ppm
Run II	-0.36 ± 0.48 ppm

Table 4.3: Pion detector asymmetry results.

vative systematic uncertainty estimate found by varying the simulation parameters.

4.4.5 Pion Detector Results

Table 4.3 presents the asymmetries measured with the pion detector for Run I and Run II. The results for the two runs differ by three standard deviations. The cause for this effect can be understood by noting that the signal in the pion detector is reduced by 40% when the insertable eP collimator (Section 3.7.5) is in place. This indicates a sizable signal due to punchthrough from the eP detector directly into the PMTs of the pion detector. Because the asymmetry measured with the eP detector was $\approx$ 1.5 ppm, the contamination of the pion detector in Run I renders it unusable. Therefore, it was decided that the Run II result would also be employed for Run I, with the Run I result disregarded. Using A^π, N_π/N_{ee}, and ϵ, the correction applied to Run I and Run II is -0.5 ± 0.8 ppb, with a dilution factor $\frac{\epsilon N_\pi}{N_{ee}}$ of 0.0014 ± 0.0011.

4.5 Synchrotron Light Monitor

The Synchrotron Light Monitor (SLM) detects synchrotron radiation produced in the A-Line, the curved beamline connecting the linac to End Station A [58]. The general location of the detector is depicted in Figure 4.20.

The device is used to quantify the vertical polarization of the beam by measuring the helicity-correlated asymmetry in the synchrotron radiation. The asymmetry has relevance to the Møller detector, because it also presents itself in the synchrotron radiation background

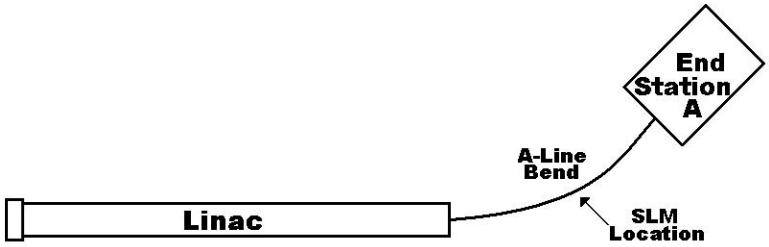

Figure 4.20: SLM location in the A-Line bend.

produced in the dipole magnets in End Station A.

4.5.1 Synchrotron Asymmetry

The power emitted by an electron beam traversing a magnet has an asymmetry related to the amount of spin polarization in the direction of the magnetic field [45, 59]. The power in a synchrotron beam is given by

$$P = P_0 \left[1 - \left(\frac{55\sqrt{3}}{24} + \eta \right) \chi \right], \tag{4.10}$$

where P_0 refers to the classically calculated synchrotron radiation power, and $\eta = \pm 1$ refers to the electron spin oriented parallel or anti-parallel to the magnetic field. The χ term reflects the properties of the applied magnetic field through

$$\chi = \frac{3\hbar\gamma^2}{2m_e c\rho}, \tag{4.11}$$

with ρ being the bend radius. The asymmetry in the synchrotron radiation power is found to equal χ through

$$A^{SR} \equiv \frac{P^+ - P^-}{P^+ - P^-} = \chi. \tag{4.12}$$

The final dipole magnet in the E158 spectrometer, D3, produced the vast majority of

the synchrotron radiation background for the Møller detector. Using the values for this magnet, it is found that the power asymmetry in the synchrotron radiation is $\approx$ 35 ppm for a 100% vertically polarized electron beam [44].

If the Møller detector were truly a calorimeter for photons over the energy range in the synchrotron radiation, the analyzing power for vertical polarization would be χ. However, it is likely that the detector has a non-linear response to synchrotron photons in the relevant energy ranges. Simulations indicate that the energy weighted asymmetry for the Møller detector would be closer to 65 ppm, rather than the real asymmetry of 35 ppm [60]. To be conservative, it will be assumed that the Møller detector has an analyzing power of 60 ppm $\pm$ 30 ppm for vertical beam polarization.

By comparing the Møller detector signal sizes for empty target runs to normal runs with the liquid hydrogen target, it was found that synchrotron radiation comprises 0.15% $\pm$ 0.05% of the total Møller detector signal. Combining this factor with the synchrotron asymmetry and an expected vertical beam polarization of $\sim$1% reduces the effect of the background to a few ppb.

The asymmetry measured with the SLM is used to place bounds on the amount of vertical polarization in the electron beam, which in turn constrains the effect of the synchrotron radiation produced in the D3 magnet on the Møller detector.

4.5.2 SLM Design

Figure 4.21 presents a schematic of the SLM. The synchrotron radiation in the SLM region exits through a 1 cm thick aluminum flange. Then, a 1 mm thick layer of lead is used to convert the photons into an electron shower. The shower then traverses a quartz bar, producing Cherenkov light. The light is directed by a mirror to three photodiodes, which

deliver the SLM signal to the ADCs. Photodiodes have low resistance to radiation, so the mirrored box is heavily shielded with lead.

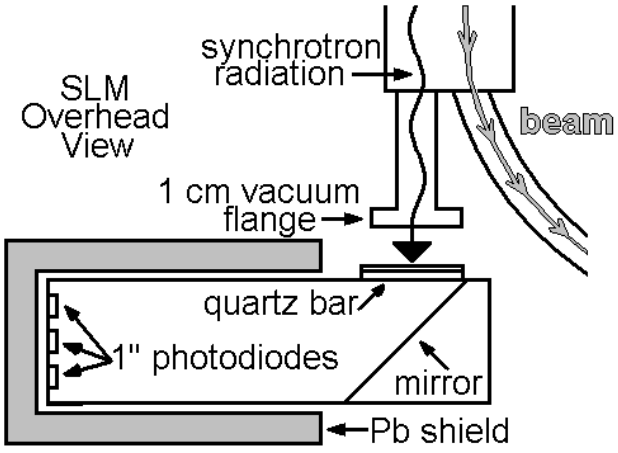

Figure 4.21: SLM layout.

4.5.3 SLM Resolution

The synchrotron radiation background affects the Møller asymmetry in a manner analogous to the pion background given in Equation 4.6:

$$A^{PV} = \frac{A^{Measured} - fA^{Synch}}{1 - f}. \tag{4.13}$$

The term f is the dilution factor, while A^{Synch} refers to the asymmetry registered in the Møller detector due to the synchrotron radiation produced in the D3 magnet of the spectrometer.

The value for fA^{Synch} is given by

$$fA^{Synch} = (0.0015 \pm 0.0005) \times (60 \text{ ppm} \pm 30 \text{ ppm}) \times P_y, \tag{4.14}$$

where the first term is the dilution factor f, the second is the analyzing power of the

Møller detector, and P_y is the vertical beam polarization. As with the pion background, it is desirable to keep the uncertainty due to the synchrotron background below 5 ppb. Therefore, the SLM is required to measure the vertical beam polarization to roughly 5%.

The analyzing power of the SLM is found from simulations to be 60 ppm ± 30 ppm (coincidentally the same as the Møller detector). Therefore, over the course of the typical data set of 80 million pulse pairs, the SLM must measure its asymmetry to the level of 2 ppm, corresponding to an asymmetry resolution of 0.03.

It was found that combining the three SLM channels actually did not significantly increase the detector resolution. The dominant noise source for the detector must be common to all three photodiodes. Therefore, it was decided to use the single SLM channel (diode 2) with the best resolution for the SLM result. Figure 4.22 depicts the asymmetry distribution of the SLM data for a typical one-hour data run.

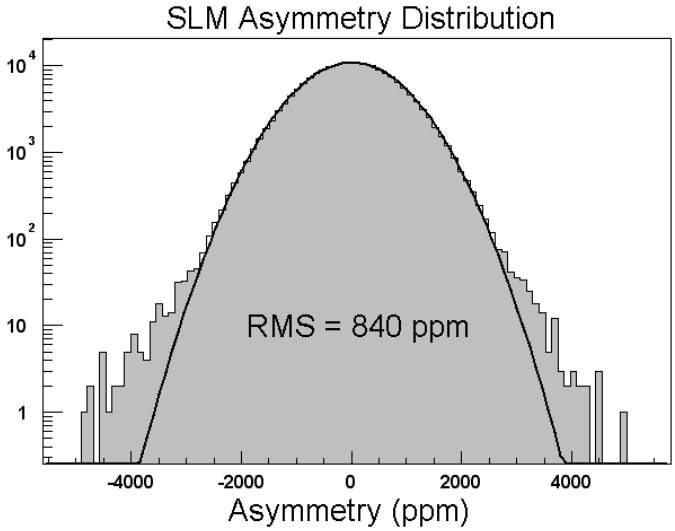

Figure 4.22: Regressed SLM channel 2 asymmetry distribution, for one run.

With an RMS of 840 ppm, the SLM greatly exceeds the resolution requirements of the E158 experiment. Unlike the pion detector, the resolution is sufficient that regression against beam monitors is useful. Like the Møller detector and the luminosity monitor, the SLM is

Vertical Polarization (%)		
	45 GeV	48 GeV
Run I	-1.7 ± 0.9	1.7 ± 0.9
Run II	-1.7 ± 0.9	3.1 ± 1.6

Table 4.4: Vertical beam polarization at the target.

regressed against beam charge, energy, X and Y position, and X and Y angle. Regression produces a factor of two improvement in the resolution, resulting in the distribution seen in Figure 4.22.

4.5.4 SLM Results

The SLM asymmetry results are presented in Figure 4.23. The data is split into four separate chunks, based on energy and source halfwave plate (HW) state. The cancellation between the energy states is good, effectively reducing the systematic effect due to synchrotron radiation for the Møller detector.

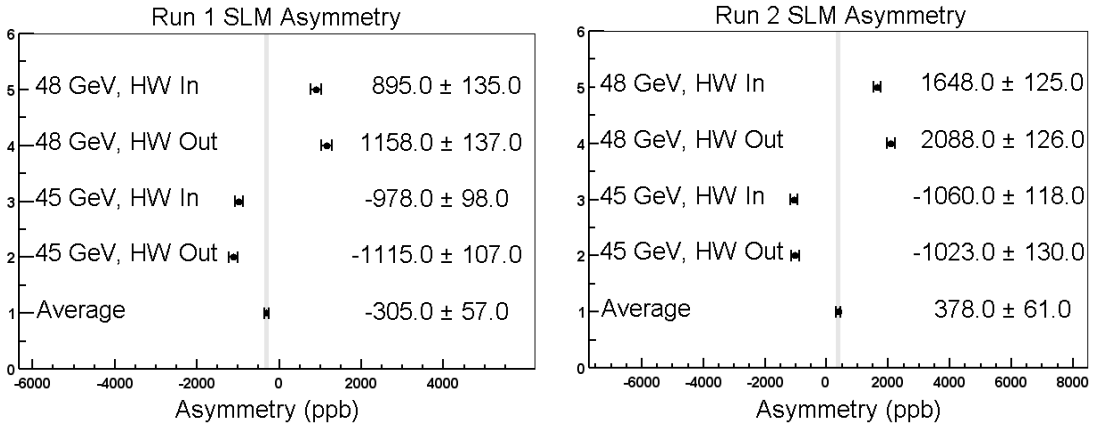

Figure 4.23: SLM asymmetry results for Run I and Run II.

Table 4.4 presents vertical beam polariation results for both Run I and Run II, computed using the SLM asymmetry. The amount of vertical polarization is ∼1%, consistent with expectations.

Using the Møller detector analyzing power and the synchrotron dilution factor, the

Diluted Synchrotron Asymmetry (ppb)		
	45 GeV	48 GeV
Run I	-1.6 ± 1.2	1.5 ± 1.2
Run II	-1.6 ± 1.2	2.8 ± 2.2

Table 4.5: Synchrotron asymmetry correction for the Møller detector.

diluted asymmetry contribution to the Møller detector asymmetry fA can be calculated. Table 4.5 details the results, which are found to be at a manageable level.

Chapter 5

Luminosity Monitor

The luminosity monitor is designed to perform measurements complementary to the Møller detector. The primary function of the device is to provide a statistically significant null-asymmetry measurement by observing extremely forward angle Møller and Mott scattering. It fills the secondary role of determining the level of density fluctuations in the liquid hydrogen target. The detector is also used to monitor the noise properties of the beam because of its large sensitivity to beam motion. All of these functions serve to ensure the data quality that is used in producing the final physics result.

5.1 Detector Signal

The luminosity monitor, henceforth to be called simply the "lumi," is positioned 70 meters downstream of the target, at an angle of one milliradian (Figure 5.1). At this location, about 70% of the scattered electrons that hit the detector have energies greater than 40 GeV. The average Q^2 of the signal is 0.003 $(\mathrm{GeV/c})^2$, an order of magnitude lower than for the signal observed with the Møller detector [61].

The signal rate in the detector is high, with approximately 3×10^8 scattered electrons for the nominal beam current of 5×10^{11} electrons per pulse. It is because of the large signal in this region that the lumi is able to provide an asymmetry measurement that has statistical

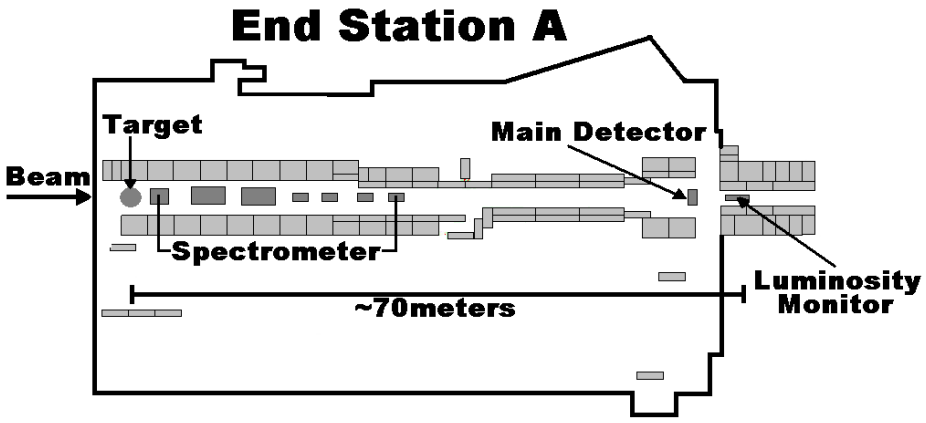

Figure 5.1: Layout of End Station A for experiment E158.

significance on the level of the result obtained by the Møller detector. Figure 5.2 depicts a Monte Carlo simulation of the various components of the lumi signal flux [62].

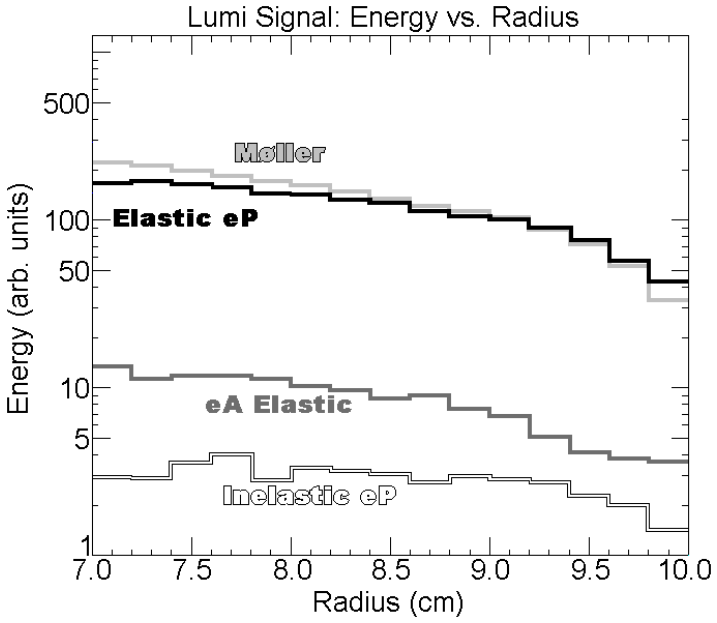

Figure 5.2: Components of lumi signal at face of detector.

The signal is dominated by Møller and Mott scattering from the target. The contribution labeled eA refers to scattering from components in the experimental apparatus other than the target. The largest contributor to this background is the aluminum end windows of the target cell. The final component is a small contribution from inelastic electron-proton

scattering in the target.

The overall expected asymmetry A^{lumi} is the sum of the individual signal component asymmetries A_i, weighted by their signal size S_i through

$$A^{lumi} = \frac{\sum_i S_i A_i}{\sum_i S_i}. \tag{5.1}$$

Figure 5.3 depicts the asymmetries of each of the lumi signal components, multiplied by the ratio of its signal size to the total signal. (Note that the sign of the eA asymmetry has been reversed.) Combining each component yields an expected asymmetry of -15 ppb ± 5 ppb

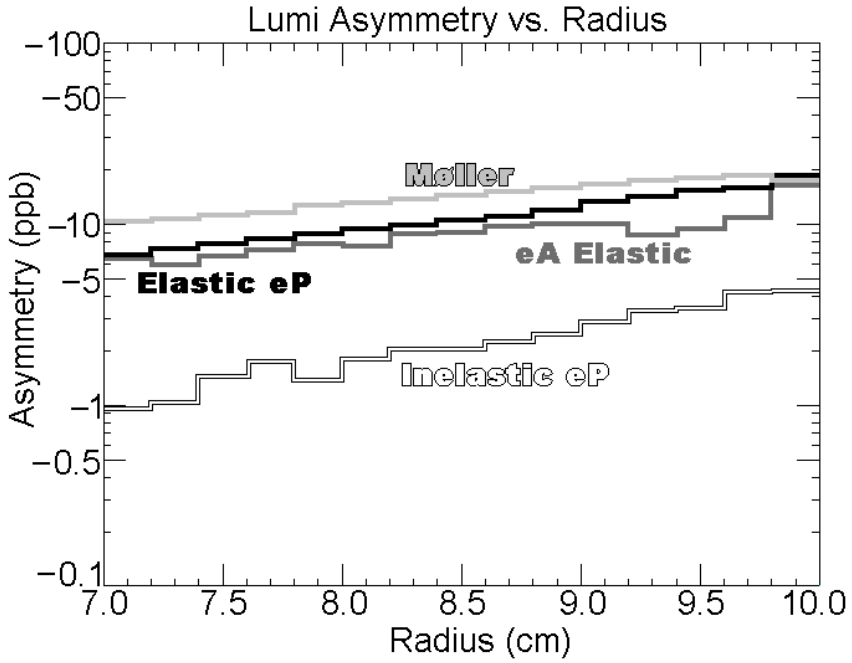

Figure 5.3: Contributions to lumi asymmetry.

for the lumi. For comparison, the Møller detector is expected to observe an asymmetry of approximately -150 ppb, a full order of magnitude larger.

Over the course of the experiment, the Møller detector is expected to observe a non-zero asymmetry with a significance of 10 standard deviations. The lumi is expected to measure

essentially zero asymmetry, with the same statistical significance. As a result, the lumi can be used to augment the Møller detector as a sensitive monitor for false asymmetries.

5.2 Synchrotron Radiation Background

The E158 spectrometer, which is discussed in Section 3.7, has three dipole magnets used to direct the primary beam around the collimation for photons from the target. The deflected beam produces synchrotron radiation, which in principle could be a large background for the lumi. The amount of power in the synchrotron beam is calculated to be about 0.02% of the total beam power [44]. For nominal data runs, this amounts to approximately 115 Watts. Simulations show that about 15% of this power is directed at the luminosity monitor [63].

Figure 5.4 displays a simulation of the distribution of background photons at the face of the lumi. The dark horizontal band is the region dominated by synchrotron radiation. The density of photons is weighted predominantly to the right side of the plot because the bend of the final dipole is to the left. The sensitive region of the detector is superimposed as the area between the black circles. The empty central region was omitted from the simulation for simplicity.

The energy absorbed from actual signal electrons is expected to be about 150 Watts, meaning that synchrotron radiation is roughly 10% of the energy of the lumi signal at the face of the detector [64]. By itself this is a large dilution factor, but the main issue of concern is that synchrotron radiation can have helicity-correlated asymmetries of its own [45, 59, 65, 66]. Asymmetries up to the level of 600 ppb could be generated in the synchrotron spectrum from the E158 spectrometer. Because the expected physics asymmetry of the lumi is only 15 ppb, it is desirable to limit the detector sensitivity to synchrotron radiation to less than 1% of the total signal. As will be demonstrated in Section 5.9, this was successfully

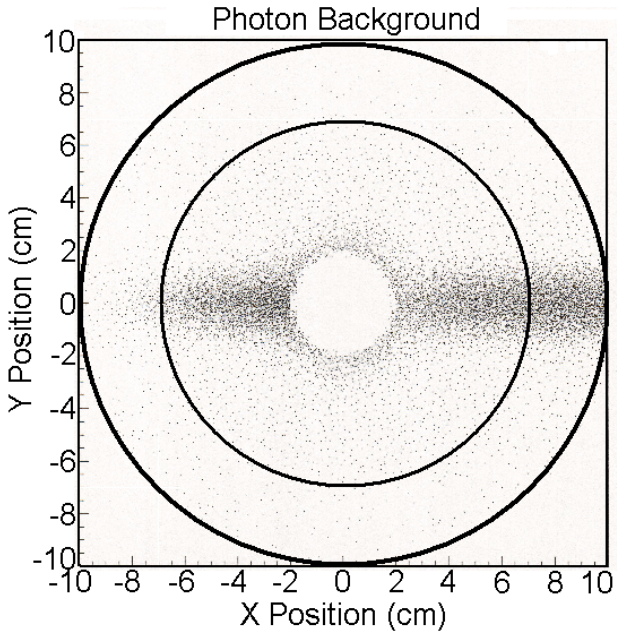

Figure 5.4: GEANT simulation of photon flux at the lumi.

incorporated into the design and renders the synchrotron background contribution small.

5.3 Detector Design

The lumi is an ionization detector, comprised of 16 individual channels. These channels are grouped into two separate, full-azimuth rings. The upstream ring is identified as the "front lumi" and the downstream ring as the "back lumi." The front lumi is positioned behind seven radiation lengths of aluminum showering material. Directly behind the front lumi is an additional four radiation lengths of aluminum, followed by the back lumi. Figure 5.5 depicts the layout of the full luminosity monitor.

The aluminum between the two sets of rings ensures that the back lumi will have a smaller signal than the front lumi. An EGS4 simulation indicates that the reduction in signal should be approximately a factor of three between the two rings [64]. The smaller signal allows the back lumi to serve as a cross-check on the front ring for systematic effects

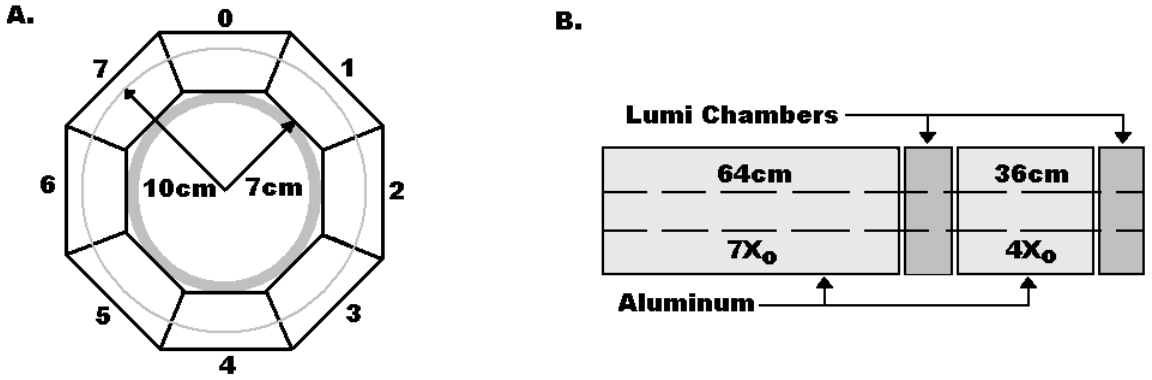

Figure 5.5: A. Front view of one full lumi ring, with sensitivity between 7 and 10 cm. B. Side view, depicting the two lumi rings and the aluminum showering material.

related to signal size.

Each chamber houses a package of 11 parallel plates (Figure 5.6), positioned transverse to the incoming signal electrons. A bias of 100 V is applied to alternate plates, in order to produce an electric field between each plate pair. As an ionizing particle traverses the chamber, it produces electron-ion pairs, which are collected on the plates as the signal.

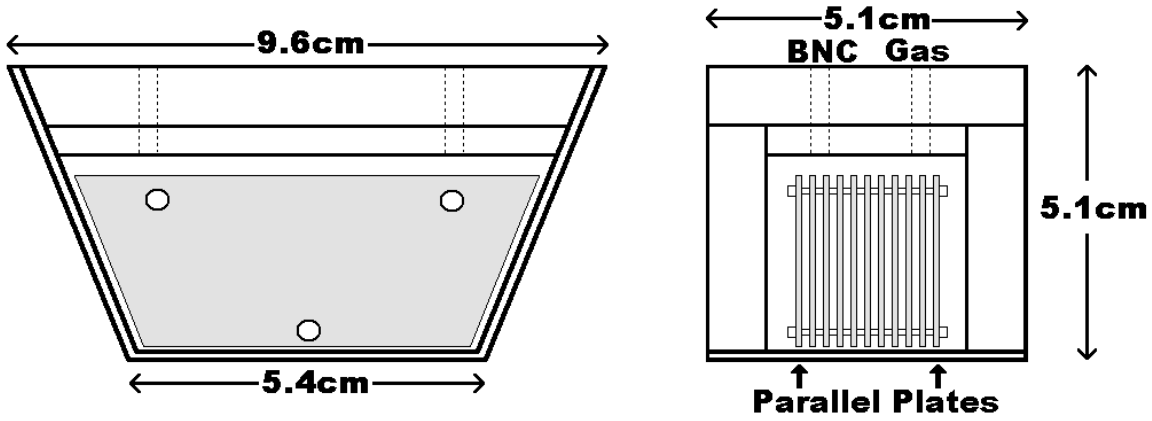

Figure 5.6: Individual chamber design, with signal plates shaded.

The chambers are filled with nitrogen gas, at a pressure of just slightly over one atmosphere. The overfilling is done to ensure that the amount of oxygen in the chambers is minimized, since it has the property that it can capture signal electrons before they are collected on the plates. The gas is continually flowed through the chambers so that

contaminants due to radiation damage are not allowed to accumulate.

An electron passing through the lumi parallel to the beamline encounters one centimeter of nitrogen. It is expected that a single electron will produce ≈ 60 ionization pairs for this amount of gas [67].

The aluminum in front of the detector rings performs the dual role of showering the main signal and attenuating synchrotron radiation. A simulation shows that the front lumi ring is positioned very close to the shower maximum, with a predicted multiplicity of roughly 100 [64]. It is also expected that the synchrotron radiation background is suppressed below the level of 1% of the signal at this depth.

The large scattering rate, coupled with the gain factors from the showering in the aluminum and the ionization trail in the nitrogen gas, allows the chambers themselves to produce signals on the level of several volts. The size of the output signal means that no additional amplification electronics are required, which considerably simplifies the detector design.

The signals travel along 100 feet of coaxial cables from the chambers to the ADCs, where they are read in differentially (after the bias voltage is filtered out of the signal cable). By subtracting the two signals from each chamber, noise pick-up from the transmission cables is suppressed. Figure 5.7 is a schematic of the lumi electronics setup.

5.4 Lumi Signals

Because each pair of plates is capacitively coupled, each chamber actually produces two signals, of opposite sign. Figures 5.8 and 5.9 display oscilloscope traces of these signals, the first from a front lumi chamber and the second from a back lumi chamber.

The time structure of the beam provided by the accelerator can be approximated as a

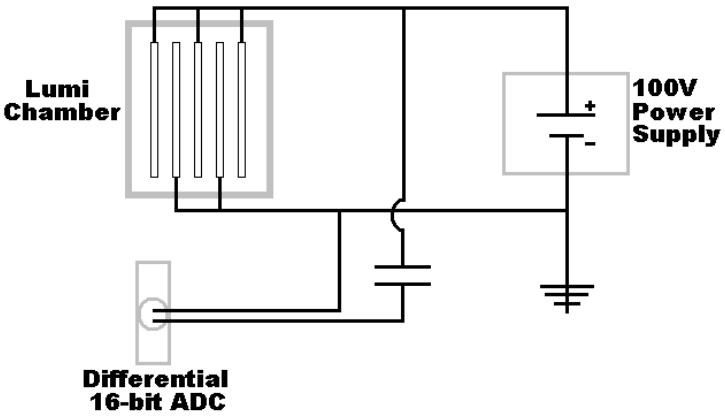

Figure 5.7: Lumi electronics setup.

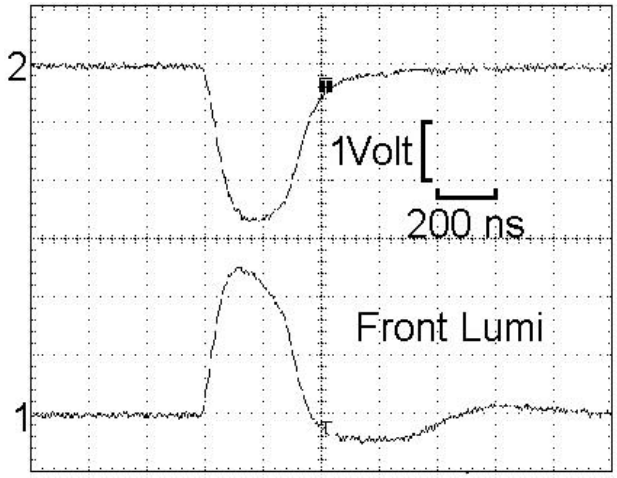

Figure 5.8: Front lumi signal traces.

square pulse with a duration of 300 ns. As can be seen from the scope traces in the figures, the lumi signal is of similar length, indicating that electron collection occurs quickly. Also note that the front lumi has a signal three times larger in magnitude than the back lumi, in agreement with simulations.

The fast signal observed on the scope is composed of the electrons from ionization pairs. The ions arrive much later than their electron counterparts due to their much higher mass. In fact, the ion signal is stretched out to such an extent that it is all but invisible on the oscilloscope traces. Nevertheless, it is statistically beneficial to collect the signal due

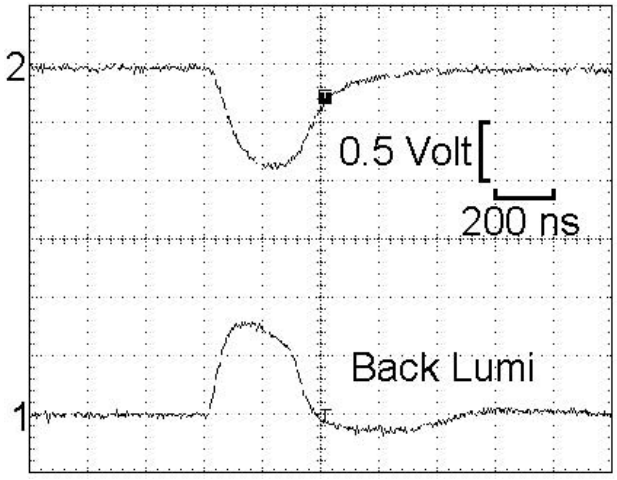

Figure 5.9: Back lumi signal traces.

to the ions. By extending the integration time of the ADCs from two microseconds to 30 microseconds, thereby collecting more ions, it is observed that the detector asymmetry resolution improves by 50%.

5.5 Gas System

The gas system (Figure 5.10) for the lumi was designed to be very simple. The nitrogen for the entire detector is supplied by a single bottle, located outside of End Station A. The flow rates of the individual chambers are balanced by adjusting needle valves located on the the output lines. During operation, the gas flow is monitored by microphones positioned to detect the sound of nitrogen bubbles escaping through silocone oil at the end of the gas lines. The flow rate was extremely low, and the gas bottle was changed only once per month. The chambers are electrically isolated from each other by inserting non-conductive tubing at the entrance and exit ports of the copper gas lines.

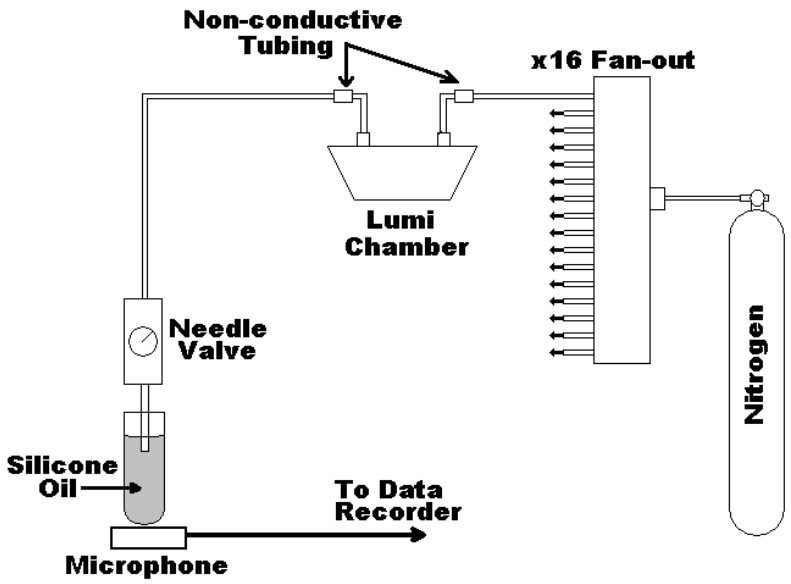

Figure 5.10: Gas system configuration for lumi.

5.6 Asymmetry Resolution

The asymmetry measured with the lumi A^{Raw} is defined as

$$A^{Raw} = \frac{\left(\frac{S}{T}\right)^R - \left(\frac{S}{T}\right)^L}{\left(\frac{S}{T}\right)^R + \left(\frac{S}{T}\right)^L}, \tag{5.2}$$

where S refers to the detector signal, L and R are the beam helicity, and T refers to the beam charge measured by a toroid just upstream of the target.

To measure the true physics asymmetry, however, effects due to beam motion must be removed. This is achieved through measuring the correlation between the detector asymmetry and the various beam monitors, and then removing this correlation. This process is known as beam regression, and will be discussed in detail in the section concerning data analysis (Section 6.3). Regression covers six parameters, removing the detector correlations with the X and Y beam positions, dX and dY beam angles, the beam energy E, and the beam charge Q.

The asymmetry is corrected on a pulse-pair basis through

$$A^{PV} = A - \sum_{n=1}^{6} c_n (b_n^R - b_n^L), \tag{5.3}$$

where the sum covers the six regression parameters, the constants c_n are the experimentally determined correlation coefficients, and the b_n terms are the values given by the BPMs. In the case of the charge correction, the difference in Equation 5.3 becomes an asymmetry measured with a toroid.

Figures 5.11 and 5.12 display the correlation coefficients for the position and angle motion obtained from a typical run, for each lumi chamber. The large azimuthal dependence of the coefficients is evident in the sinusoidal pattern in the plots. The numbering scheme for the chambers is the same as found in Figure 5.5.

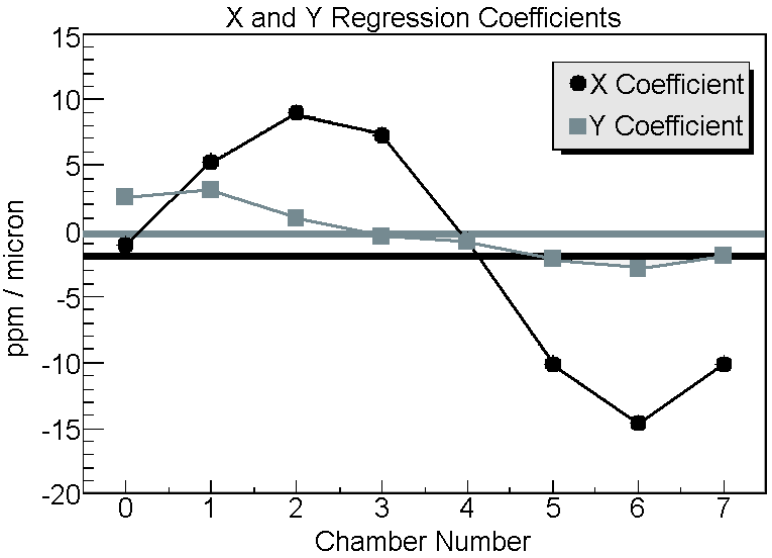

Figure 5.11: X and Y correlation coefficients. The averages are shown as straight lines.

The asymmetry for the whole detector is the average of the asymmetries found by the individual chambers, given by

$$A_{Total}^{PV} = \frac{1}{N} \sum_{m=1}^{N} A_m^{PV}. \tag{5.4}$$

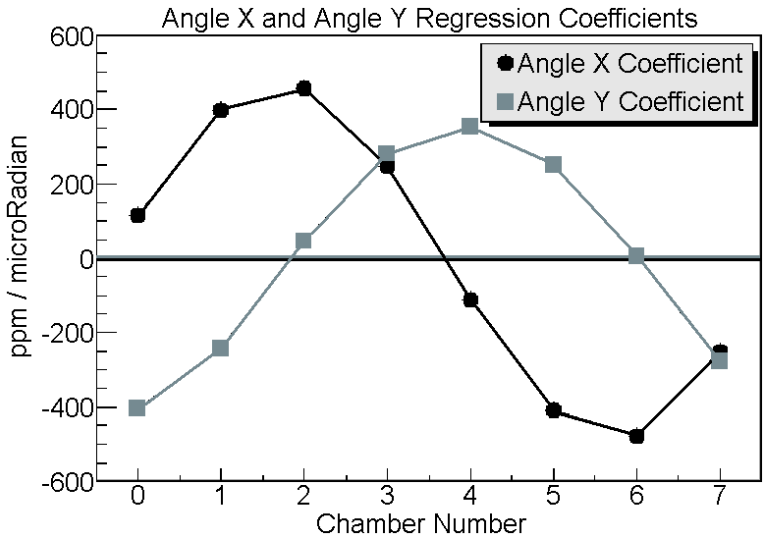

Figure 5.12: dX and dY correlation coefficients The averages are shown as straight lines.

Here the sum is over the individual lumi channels, and N refers to the total number of channels used. Since the front lumi and back lumi are treated as separate detectors, this number is usually eight.

Substituting Equation 5.3 into Equation 5.4 for each chamber yields the expression for the whole detector through

$$A^{PV}_{Total} = \frac{1}{N}\sum_{m=1}^{N}(A^{Raw}_{m} - \sum_{n=1}^{6} c^{m}_{n}(b^{R}_{n} - b^{L}_{n})), \tag{5.5}$$

which can be written as

$$A^{PV}_{Total} =< A^{Raw} > - \sum_{n=1}^{6} < c_n > (b^{R}_{n} - b^{L}_{n}). \tag{5.6}$$

The variable m is summed over the lumi channels, and n sums over the beam monitors. The form of the asymmetry given in Equation 5.6 is exactly the same as in Equation 5.3, except that the terms are replaced by averages over the chambers. In particular, it can be seen that the correlation coefficient relevant for the detector as a whole is the average of

the individual chamber correlation coefficients.

The average of the channel coefficients is plotted as a solid line in Figures 5.11 and 5.12. The average is always much less than the amplitude seen in the coefficients of the individual chambers, indicating that the sensitivity of the detector as a whole to beam motions is much less than the individual chamber sensitivities. The suppression is so large because lumi chambers are automatically gain matched by design.

The RMS of the distribution of A^{PV} is the resolution of the detector. For a given set of data, the resolution determines how well the mean asymmetry is known. The Møller detector typically has an RMS of 200 ppm. For the lumi to serve as a useful cross-check on the main detector, then, it must also have an asymmetry resolution of at least 200 ppm. Figure 5.13 demonstrates the level of improvement in resolution obtained by removing detector correlations to the beam through regression. The RMS of the corrected distribution is roughly 100 ppm, which is at a level that meets experimental goals for the lumi design.

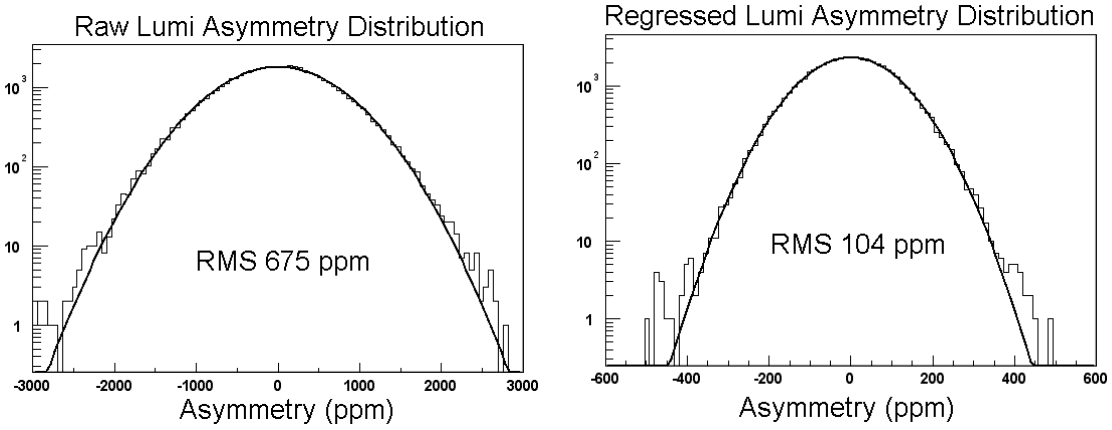

Figure 5.13: Left: Raw lumi asymmetry distribution. Right: Regression-corrected lumi asymmetry distribution.

5.7 Resolution Contributions

In order to evaluate the performance of the lumi, it is instructive to itemize the contributions to the overall asymmetry resolution. Mathematically, it can be shown that the expected resolution is given by

$$\sigma^2_{A^{PV}} = \frac{1}{2N}(1+\frac{\Delta E}{E}^2)+\sigma^2_{Boiling}+\sigma^2_{Pedestal}+(1+c_Q)^2\sigma^2_{ToroidResolution}+\sum_{n=1}^{5} c_n^2\sigma^2_{BPMResolution}. \tag{5.7}$$

The term $\sigma_{A^{PV}}$ refers to the statistical width of the asymmetry distribution. The number of scattered electrons entering the detector is given by N, so the $\frac{1}{2N}$ term is a reflection of counting statistics. The statistics are modified by the energy resolution of the detector, represented by the $\frac{\Delta E}{E}$ term. The next term, $\sigma_{Boiling}$, refers to contribution due to density fluctuations in the liquid hydrogen target. The term $\sigma_{Pedestal}$ represents all types of electronics noise. The final two terms involve the resolutions of the toroid and beam position monitors, indicated by $\sigma_{ToroidResolution}$ and $\sigma_{BPMResolution}$, respectively. The beam monitors affect the lumi asymmetry resolution because they are used in the regression process, discussed in the previous section. The degree to which the beam monitors contribute is related by the experimentally determined correlation coefficients c_n. The toroid term has a slightly different form than that of the BPMs because it is used for both normalization and as a regression parameter.

Each item in Equation 5.7 is separately known. The beam monitor resolutions can be obtained directly from the data, as discussed in Section 3.2.2. Zero current beam pulses occur at a rate of 0.5 Hz during normal running, allowing $\sigma_{Pedestal}$ to be measured reasonably well. The contribution due to counting statistics is obtained from a Monte Carlo simulation. The energy resolution of 50% is obtained from a simulation of the detector response. The

Luminosity Monitor Resolution Contributions			
Parameter	Coefficient	BPM Resolution	Contribution (ppm)
Q	-0.097 ppm/ppm	28.5 ppm	26
E	-3.17 ppm/MeV	2.0 MeV	6
X	-5.36 ppm/μm	3.3 μm	18
Y	-0.52 ppm/μm	4.5 μm	2
dX	-11.48 ppm/μR	0.1 μR	1
dY	4.81 ppm/μR	0.2 μR	1
Counting Statistics			45
Energy Resolution			20
Boiling Noise*			50
Pedestal Noise			60
Total		Calculated:	98
		Observed:	104

Table 5.1: Contributions to the luminosity monitor asymmetry resolution. *Target boiling is covered in Section 5.8.

energy resolution is low because many of the showers are not contained by the detector. This leaves the term due to boiling noise, which is calculated using the method described in Section 5.8. Combining these contributions for a run provides a full resolution accounting for the lumi. Table 5.1 presents the resolution contribution itemization for a typical one-hour data run.

The dominant contributions to the resolution are electronics noise, boiling noise, and counting statistics. The remaining contributions due to beam monitor resolution are small by comparison. The observed resolution of 104 ppm compares well with the calculated value of 98 ppm, indicating that all major noise sources are known. The resolution exceeds the 200 ppm level required by the experiment.

5.8 Target Boiling

As discussed in Section 3.6, heating from the primary beam can cause density fluctuations in the liquid hydrogen target. Though it is not technically "boiling" that is occurring, this is still the standard name that has attached itself to this issue. The amount of boiling is

important to the experiment because it directly translates to noise for the detectors. Also, if there exists an asymmetry in the density fluctuations, a false asymmetry measured by the detectors could result.

In principle, once the lumi and Møller detector asymmetries are corrected for beam motion, the only correlation between them is in target density fluctuations and the resolutions of the beam monitors used for the corrections. The latter contribution can be obtained from the data, so by observing the level of common-mode noise between the two detectors, the amount of boiling noise can be extracted. The method employed [42] begins by defining two composite asymmetries through

$$J_{\pm} \equiv A_{M\text{ø}ller} \pm A_{Lumi}. \tag{5.8}$$

Here A refers to the regression corrected asymmetries of the Møller detector and the lumi. If the two detectors were completely uncorrelated, the RMS of the distributions of J_+ and J_- would be the same. The amount that the two differ yields the common-mode noise between the two detectors. Accounting for the noise due to beam monitor resolutions, the amount of boiling noise is given by

$$\sigma^2_{Boiling} = \frac{\sigma^2_{J_+} - \sigma^2_{J_-}}{4} - (1 + c^M_Q + c^L_Q)\sigma^2_{ToroidResolution} - \sum_{n=1}^{5} c^M_n c^L_n \sigma^2_{BPMResolution}. \tag{5.9}$$

As with the preceding section, the c_n terms refer to the beam correction coefficients. The superscripts M and L refer to the Møller detector and the lumi, respectively. Similar to Equation 5.7, the toroid term differs from the BPM terms because it is used for both normalization and as a regression parameter.

To determine how much of this "boiling" noise is actually due to target density fluc-

Run Label	Spot Size(mm x mm)	Pump Speed(speed/nominal)
1	1.5 x 1.5	1
2	1.0 x 1.0	1
3	1.0 x 1.0	1
4	1.0 x 1.0	1
5	1.5 x 1.5	2/3
6	1.0 x 1.0	2/3
7	1.0 x 1.0	2/3
8	1.0 x 1.0	2/3
9	1.5 x 1.5	1/3
10	1.0 x 1.0	1/3

Table 5.2: List of target boiling data runs.

tuations, as opposed to some other unmeasured common-mode noise source, a battery of runs were taken in which the parameters of the beam and target were varied. Table 5.2 details the conditions for these runs, while Figure 5.14 displays the amount of boiling noise calculated for each run, using Equation 5.9.

The term "spot size" refers to the dimensions of the beam at the entrance to the scattering chamber, as determined by the wire array (Section 3.4). Smaller beam spot size should translate to greater target boiling effects. The vast majority of production data was taken in the 1.0 mm x 1.0 mm spot size configuration. The pump speed regulates the velocity of the liquid hydrogen around the target loop. Slower speeds should naturally translate into larger boiling effects since the hydrogen remains in the beam for longer periods of time. The nominal pump speed produces a liquid hydrogen velocity of 10 m/s, while the lowest pump speed produces essentially zero flow [41].

Figure 5.14 shows little variation in the amount of calculated boiling noise among the configurations tested. The small data spread indicates that the dominant common-mode noise between the lumi and the Møller detector is not caused by target density fluctuations.

Even if all of the common-mode noise between the two detectors were due to boiling, the effect is still only roughly 50 ppm. This amount of boiling noise is well below the proposal

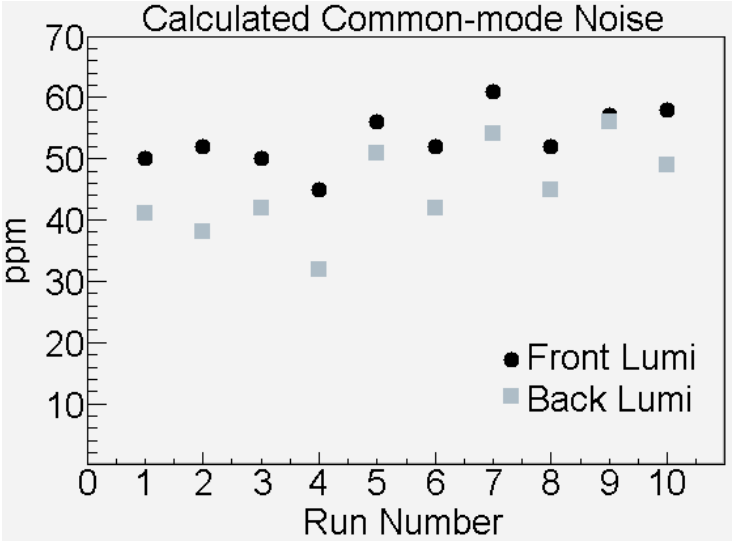

Figure 5.14: Extracted boiling noise.

goal of 100 ppm [37]. Barring a large asymmetry observed by the lumi, this level of noise renders boiling effects inconsequential for the Møller detector analysis.

5.9 Synchrotron Radiation Suppression

As discussed in Section 5.2, it is important that synchrotron radiation comprise no more than 1% of the total lumi signal. Simulations show that the aluminum material in front of the lumi reduces the synchrotron background by a large factor. To measure the suppression, the signal sizes with the target in place and empty target runs are compared. When the target is out, the dominant background is synchrotron radiation. Figure 5.15 displays the synchrotron suppression results obtained for each chamber. The channel numbering follows the convention established in Figure 5.5.

As expected from the synchrotron distribution (Figure 5.4) the background is heavily peaked in chamber two, the channel on the right side of the lumi rings. Even if all of this background were due to synchrotron photons, it is clear that it is significantly below

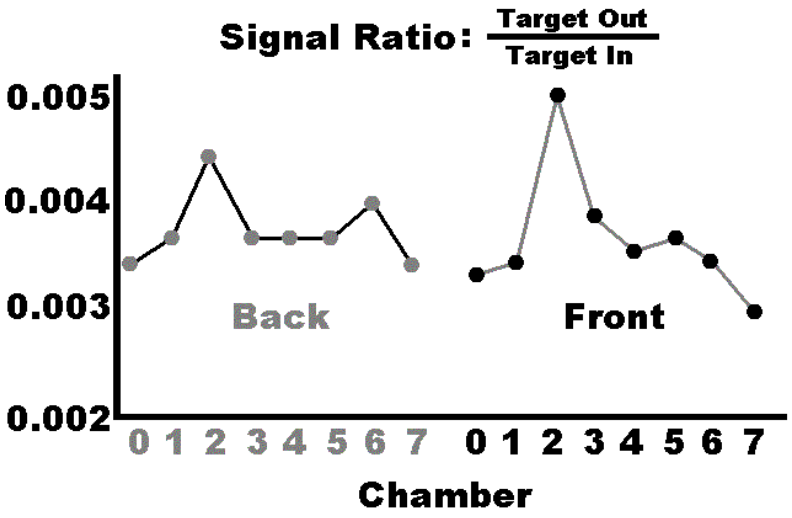

Figure 5.15: Synchrotron radiation background levels by chamber.

the desired 1% level. Because there are assuredly other background sources present, the true synchrotron radiation background is actually closer to the difference between chamber two and chamber zero, roughly 0.2%. The maximum asymmetry expected from synchrotron radiation is at the 600 ppb level, so the asymmetry contribution of the synchrotron radiation is reduced to the level of a few ppb.

5.10 Linearity

Although the lumi signal flux is quite large, the detector was designed to remain linear to better than 1%. The main design concern is that electrons and ions could recombine before being detected on the plates in the chambers. This effect would likely scale with signal size, producing a non-linearity. The small distance between the collection plates was chosen to limit electron transit time, and the 100 V bias was chosen to produce a fast signal. These two design features limit the chance of electron-ion recombination, and are expected to produce a very linear response.

5.10.1 Requirements

The requirement that individual systematic uncertainties be at the level of 5 ppb or below can be used to set the linearity limit for the E158 detectors. For simplicity, the response of the detector to charge is assumed to be a blend of linear and quadratic terms through

$$S = \alpha F - \beta F^2, \tag{5.10}$$

where S is the lumi signal size, F is the real signal flux, and α and β are constants. The flux is related to the beam charge N through

$$F^{L,R} = \sigma^{L,R} N, \tag{5.11}$$

where L and R refer to the beam helicity, and $\sigma^{L,R}$ is proportional to the scattering cross section. The non-linearity of the detector response ϵ is defined as the ratio of the quadratic term to the full signal, as

$$\epsilon \equiv \frac{\beta F^2}{\alpha F - \beta F^2} \approx \frac{\beta F}{\alpha}. \tag{5.12}$$

The E158 toroids are known to be very linear (Section 3.3.2), so their response T is assumed to be simply proportional to charge:

$$T = N. \tag{5.13}$$

Inserting the forms in Equations 5.10 through 5.13 into the asymmetry defined in Equation 5.2 yields

$$A^{Measured} = (1 - \epsilon) A^{Phys} - \epsilon A^{Toroid}, \tag{5.14}$$

where A^{Phys} refers to the true parity-violating asymmetry, and A^{Toroid} is the charge asymmetry measured with the toroid. However, because charge is included as a regression parameter in Equation 5.3, the term proportional to A^{Toroid} is effectively removed. Note that the charge regression coefficient can be identified as ϵ, the non-linearity of the detector. The final result is then

$$A^{Measured} = (1 - \epsilon)A^{Phys}. \tag{5.15}$$

Assuming that the physics asymmetry is 15 ppb for the lumi and 150 ppb for the Møller detector, the linearity $1 - \epsilon$ must be determined to 30% for the lumi and 3% for the Møller detector, to keep the systematic uncertainty at the level of 5 ppb. Perhaps surprisingly, this renders the linearity of the lumi unimportant.

The charge regression coefficient for the lumi varies between 3% and 8%. At face value, this indicates that the lumi is less linear than expected. However, while the charge coefficient certainly contains non-linearity information, as discussed in Section 6.7.2.2, it also contains sensitivity to any unmeasured beam parameter. Therefore, while regression against charge removes detector non-linearity, it can not be used to quantify it.

5.10.2 Measured Linearity

As demonstrated in the preceding section, it is not paramount that the lumi possess exceptional linearity, because of the additional regression performed against charge. However, since the detector was designed to keep non-linearities below the level of 1%, it is still instructive to quantify the linearity of the detector.

In principle, the linearity could be determined by observing the ratio of lumi signal to the toroid signal for various currents, since the toroids are known to be essentially linear. Figure 5.16 displays the lumi signal versus current for a single data run.

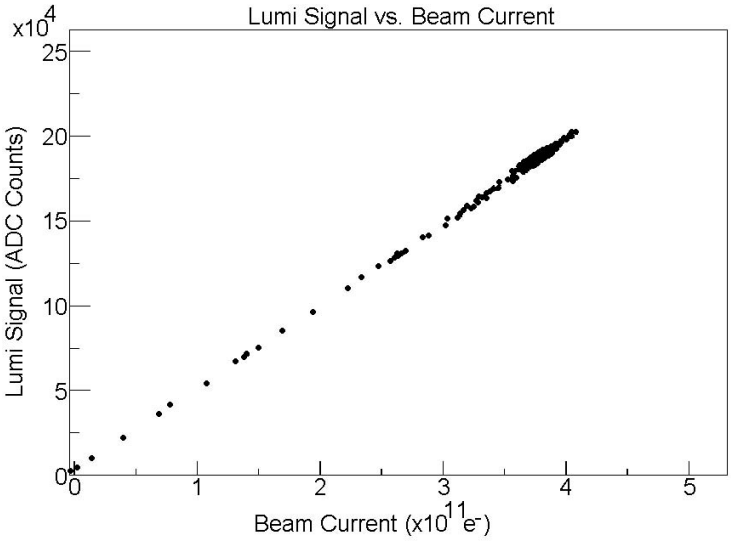

Figure 5.16: Lumi signal versus beam current.

Because most beam parameters such as position and angle are also correlated to charge, Figure 5.16 is not a clean representation of the lumi response to current. The lumi is sensitive to beam motion, so plots such as this can only be used to bound the lumi non-linearity to $\sim$10%, which is similar to the result obtained from the charge regression coefficient.

To obtain a better linearity determination, the effect of the motion of the beam must be mitigated. One way to do this is to observe the ratio of the unnormalized lumi asymmetry A_0 to toroid asymmetry A^{Toroid}. The asymmetries are defined as

$$A_0^{Lumi} \equiv \frac{S^R - S^L}{S^R + S^L} \tag{5.16}$$

and

$$A^{Toroid} \equiv \frac{T^R - T^L}{T^R + T^L}, \tag{5.17}$$

with S and T referring to the lumi and toroid signals, respectively. Using the forms for the lumi and toroid signals given in Equations 5.10 and 5.13, the relation between A_0^{Lumi} and

A^{Toroid} is

$$A_0^{Lumi} = (1 - \epsilon)A^{Toroid}. \tag{5.18}$$

The ϵ term that appears on the right-hand side of Equation 5.18 modifying the proportionality to the toroid asymmetry is again the lumi non-linearity.

The linearity is determined by plotting the ratio of A_0^{Lumi} to A^{Toroid} as a function of the analysis cut on beam jitter. As the beam cuts are tightened, the ratio of the uncorrected lumi asymmetry to the toroid asymmetry then tends toward $1 - \epsilon$, the linearity of the detector.

Figures 5.17 and 5.18 show the results of measuring this ratio as a function of the cut on beam jitter. Here 100 production data runs have been used, which is roughly one quarter of the full data set for Run I. The beam cut refers to the maximum allowed beam jitter, in both X and Y, measured at the lumi. These numbers were obtained using the lumi as a BPM, as detailed in Section 5.12. The points at the left of the plot have the most stringent beam jitter cut.

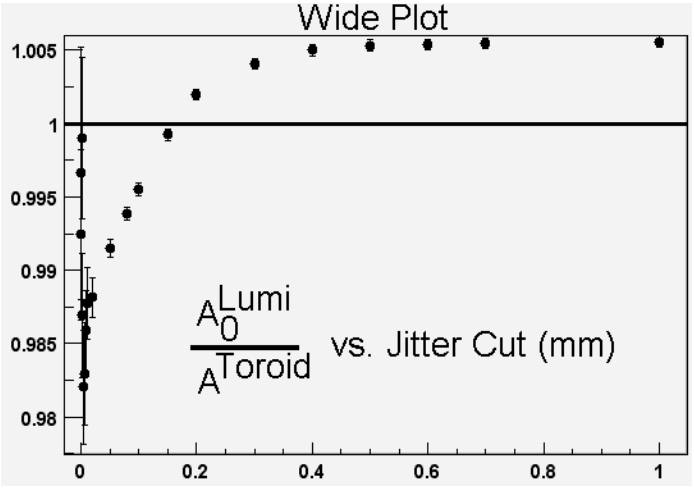

Figure 5.17: Full range of results.

It is clear that the ratio never departs dramatically from unity, indicating that no gross

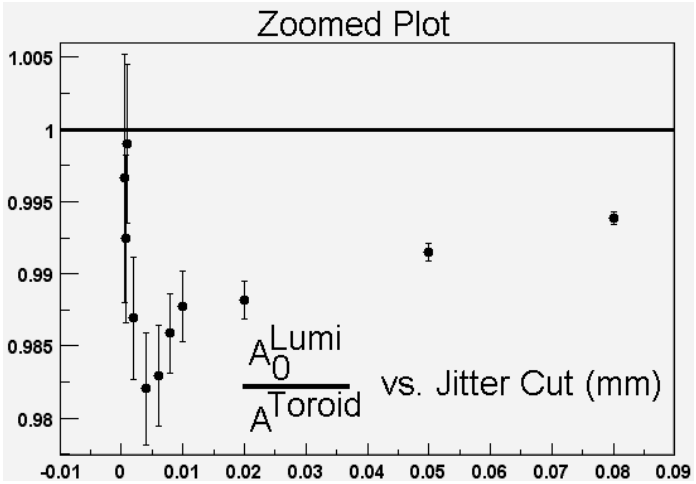

Figure 5.18: Tight beam cuts subset of linearity results.

non-linearity exists. As the beam cuts are tightened, the ratio is seen to vary between 98.0% and 100.5%, demonstrating the linearity of the lumi to the level of $\approx 2\%$.

5.11 Missing Pulse Effect

An unexpected feature of the lumi signal reveals itself after a beam pulse is absent. Missing pulses occur regularly at 0.5 Hz, due to a scheduled pedestal pulse, and random beam drop-outs also occur. Figure 5.19 displays the charge-normalized front lumi signal versus time, with a missed-pulse occurring at the zero of the x-axis. The signal is noticeably larger after the missed pulse, though it is still only 0.5% above the average signal. The effect decays quickly and is virtually absent after 3 pulses.

A possible explanation for this behavior is that the detector, which is really a capacitor, is only allowed to recharge fully during the missing pulse. This would explain why subsequent pulses receive a boost in size. No other detectors see the effect, so it appears that this behavior is internal to the lumi design.

Whatever the true cause, the effect produces additional tails to the lumi asymmetry

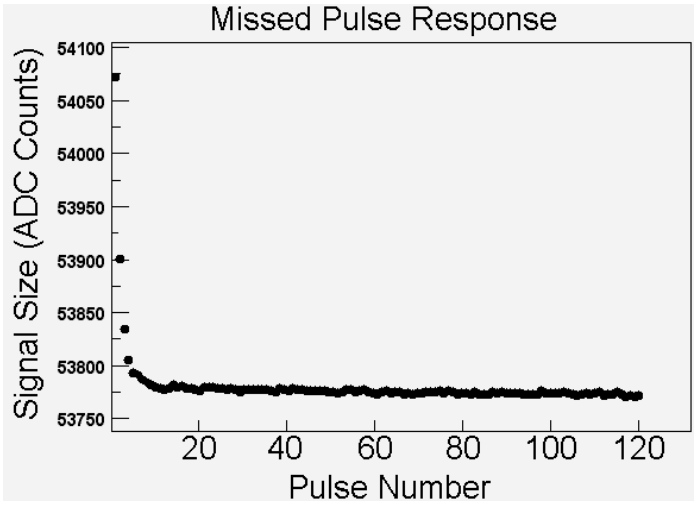

Figure 5.19: Charge normalized lumi signal following a missing pulse.

distributions, resulting in an effective decrease in the asymmetry resolution. To combat this, a cut in the analysis is made to remove the first 8 pulses after the pedestal pulse. This amounts to a 7% cut on the data. Figure 5.20 demonstrates the improved detector resolution when the additional cut is included.

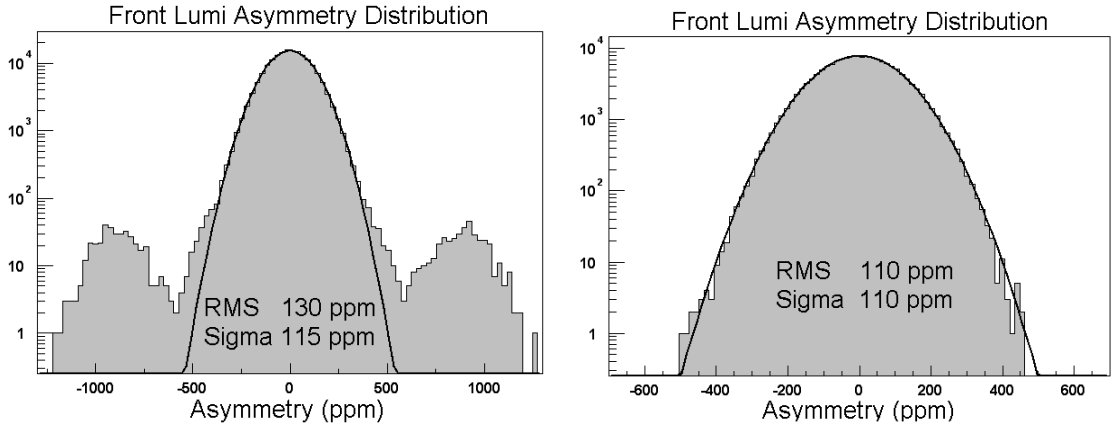

Figure 5.20: The lumi asymmetry distribution without (left) and with (right) a cut after a missing pulse. *RMS* is the statistical width of the distribution, while *Sigma* refers to the width determined from the fit.

This cut renders the data sets of the lumi and Møller detector slightly different. So that the lumi can still serve as a viable systematic cross-check, it was verified that the cut does

not change the mean returned by the Møller detector at a significant level.

5.12 Lumi as a BPM

There are no amplifiers used for the lumi chambers, and all chambers are identical, making the relative gain among the chambers very close to one. An interesting application of this feature allows the lumi to be used as a beam position monitor.

The X and Y positions at the lumi are calculated by weighting the chamber signals S by the chamber spatial positions through

$$X = \alpha_x \frac{\sum_{n=1}^{8} \sin\theta S_n}{\sum_{n=1}^{8} S_n} \tag{5.19}$$

and

$$Y = \alpha_y \frac{\sum_{n=1}^{8} \cos\theta S_n}{\sum_{n=1}^{8} S_n}, \tag{5.20}$$

where θ refers to the azimuthal location of the chamber. By convention, zero degrees refers to the chamber at the top of the lumi ring, and the angle increases in the clockwise direction looking downstream from the target.

The α coefficients are determined by using the beam position in the BPMs upstream of the target and extrapolating to the position at the lumi detector. Several runs were taken with large angular displacement on target during the course of the experiment, allowing for a large lever-arm to determine the α coefficients. Figure 5.21 displays the results obtained utilizing these runs. Each point represents the average position over the course of one full run.

The displacements used in these plots are an order of magnitude greater than would be

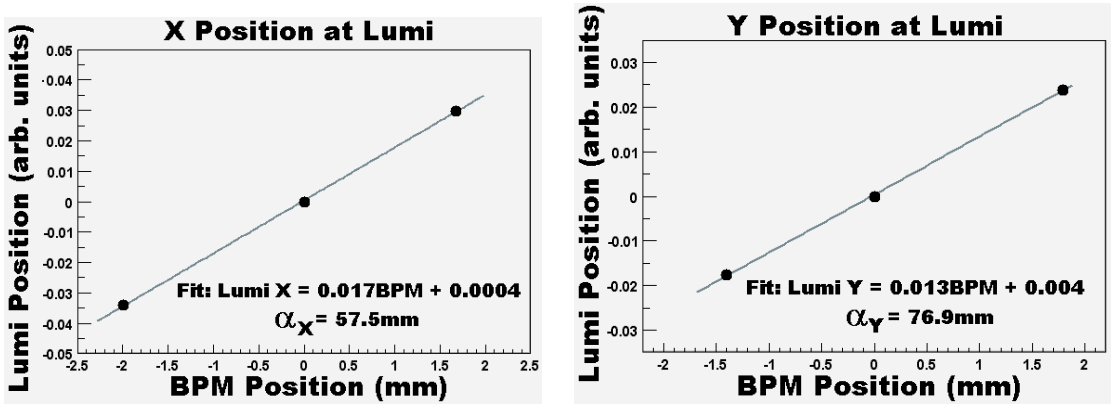

Figure 5.21: Calculated beam position using the lumi, versus position position at lumi figured using angle and position bpms.

expected naturally during a typical data run. It is clear that the lumi response to smaller displacements should be linear. Note that the α coefficients are different for X and Y because the beam was not centered through the detector.

The main utility of using the lumi as a beam monitor is that it provides the beam location at the position of the detectors. Having an effective BPM was particularly useful when adjusting the dipole chicane magnets, which are downstream of the last E158 BPMs. Also, it was simple to create a display that continually updated the position reported by the lumi, so that data takers could quickly see that the beam was well positioned through the detectors. Moreover, since the detector gains were found to be very stable, the lumi proved to be a useful tool for beam re-alignment after long beam-off periods.

Chapter 6

Asymmetry Analysis

This chapter describes the determination of the parity-violating asymmetry A^{PV} from the raw asymmetry A^{Raw} measured with the Møller detector. The effects of background corrections and dilutions are discussed, and the systematic uncertainty on the measurement is estimated. The analysis of the luminosity monitor data is also presented.

6.1 Initial Processing

Before any analysis is performed, an initial pass is made over the data to put it into a usable form. The 0.5 Hz no-beam pulses are used to subtract the pedestal from all detector and beam monitor channels. The subtraction for a given beam pulse utilizes the running average of the preceding 10 pedestal pulses. The data from the Møller detector is also "blinded" with a random offset, such that the asymmetry A from each channel becomes

$$A \rightarrow A + A', \tag{6.1}$$

where A' is a single random number in the range of ± 200 ppb. The value of A' was not revealed until the asymmetry analysis was completed. The offset was included to reduce the potential for human bias in the determination of A^{PV}.

6.2 Detector Channel Weights

The raw pulse-pair asymmetry A^{Raw} measured with the Møller detector is defined as a weighted average of the detector channels, given by

$$A_i^{Raw} = \sum_{j=1}^{30} w_j A_i^j. \tag{6.2}$$

Here A_i^j denotes the asymmetry measured with the j^{th} detector channel for the i^{th} pulse pair, and w_j is the weight for that channel. The weights w_j are constrained by

$$\sum_{j=1}^{30} w_j = 1. \tag{6.3}$$

The sum covers the 30 channels of the Møller detector, comprised of the In and Mid regions (Section 4.1) of the E158 calorimeter depicted in Figure 4.4.

The weights are found on a per-run basis through a minimization method which takes into account inter-channel correlations. The method is employed to maximize the asymmetry resolution of the overall Møller detector. First, the symmetric matrix M_{ij} is defined by

$$M_{ij} = \langle A_i A_j \rangle - \langle A_i \rangle \langle A_j \rangle, \tag{6.4}$$

where A_n denotes the asymmetry measured with channel n. Channel weights are defined by minimizing the sum N, defined as

$$N = \sum_{i=1}^{30} \sum_{j=1}^{30} w_i w_j M_{ij}. \tag{6.5}$$

Note that in the absence of correlations among the channels in Equation 6.4, the weights

reduce to

$$w_i = \frac{\frac{1}{\sigma_i^2}}{\sum_{j=1}^{30} \frac{1}{\sigma_j^2}}, \tag{6.6}$$

the standard statistical weights.

6.3 Regression

The sensitivity of the detectors to beam motion and energy jitter is reduced through a process called regression. Figure 6.1 depicts the raw asymmetry of the Møller detector (Equation 6.2) versus the Y position asymmetry, measured with a BPM just upstream of the target. The strong correlation indicates that asymmetries in the Y position can be manifested in the asymmetry measured with the Møller detector.

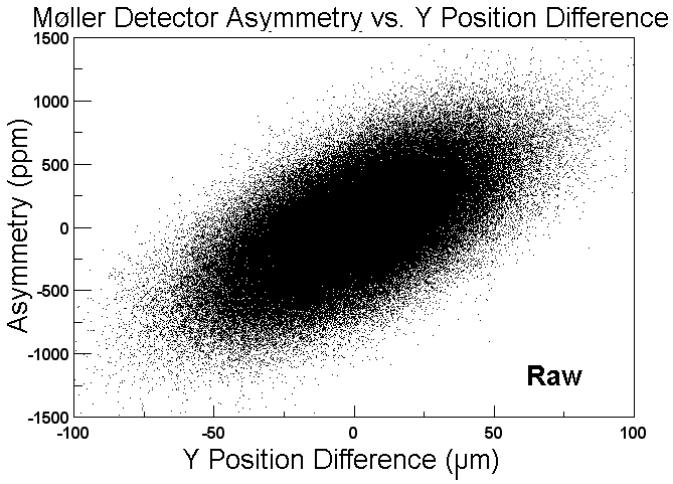

Figure 6.1: Møller detector asymmetry versus Y position asymmetry.

The regression procedure involves calculating the correlation slope seen in Figure 6.1 and removing it on a per-pulse basis. The detector asymmetry A^{Raw} is corrected for the beam asymmetry ΔB_n through

$$A = A^{Raw} - \sum_{i=1}^{6} c_n \Delta B_n, \tag{6.7}$$

where A is the corrected asymmetry, and the sum runs over the beam parameters of charge Q, energy E, X and Y position, and X and Y angle. The regression coefficients c_n are the correlations of the detector asymmetry with the n^{th} beam parameter.

The coefficients are experimentally determined by performing a multidimensional fit of A^{Raw} against the six beam parameters. The covariance matrix B_{ij} is defined as

$$B_{ij} = \langle \Delta B_i \Delta B_j \rangle - \langle \Delta B_i \rangle \langle \Delta B_j \rangle, \tag{6.8}$$

and the vector V_i is

$$V_i = \langle A^{raw} \Delta B_i \rangle - \langle A^{Raw} \rangle \langle \Delta B_i \rangle. \tag{6.9}$$

The coefficients c_n are obtained by inverting the matrix B and multiplying by the vector V.

$$c_j = \sum_{i=1}^{6} B_{ij}^{-1} V_i \tag{6.10}$$

Because the coefficients could change over time, they are determined every 10,000 pulse pairs.

Figure 6.2 depicts the same data presented in Figure 6.1 after the regression correction of Equation 6.7 has been applied. The correlation of the detector asymmetry with the beam asymmetry is greatly reduced.

Regression also enhances detector resolution by reducing the effect of beam fluctuations on the asymmetry distribution measured with the detector. Figure 6.3 depicts the improvement in detector performance with regression. The resolution is improved by $\approx 60\%$.

The different E158 detectors are positioned at different geometries, causing their sensi-

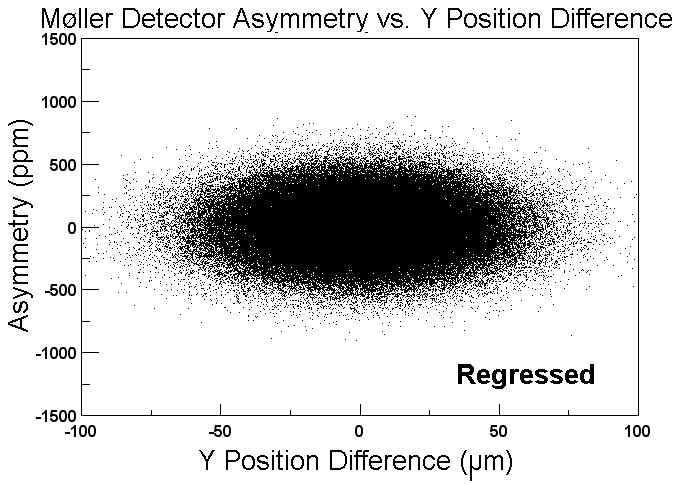

Figure 6.2: Møller detector asymmetry versus Y position asymmetry after regression.

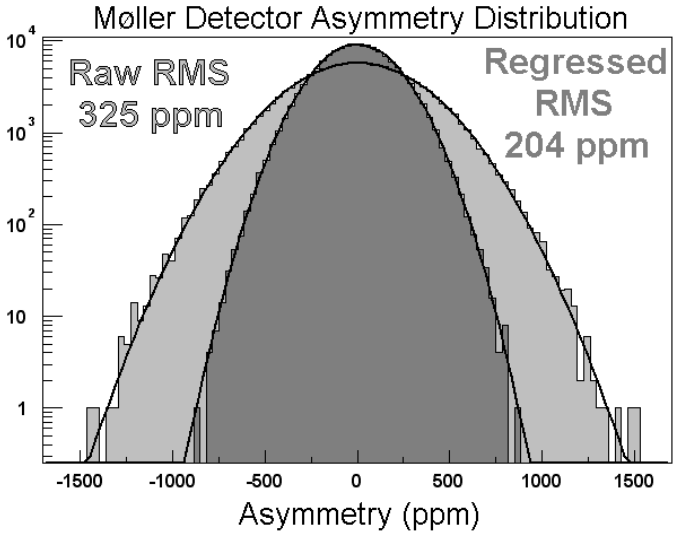

Figure 6.3: Møller detector resolution with and without regression.

tivity to beam parameters to vary greatly. Table 6.1 presents the coefficients of three E158 detectors, averaged over all Run I data. The Out detector is the most sensitive detector for all categories. The large coefficients are due to the large slope in its signal flux profile (Figure 3.25), so that small deviations in beam parameters result in comparatively large changes in the Out detector signal size.

Run 1	Detector		
Coefficient	Møller	Out	Front Lumi
Q (ppm/ppm)	0.005	-0.08	-0.03
E (ppm/MeV)	-25.9	76.2	-5.1
X (ppm/μm)	0.5	6.8	-1.1
Y (ppm/μm)	-1.2	2.0	0.4
dX (ppm/μR)	-66.1	128.2	25.2
dY (ppm/μR)	7.3	65.5	-12.9

Table 6.1: Regression coefficients for Run I.

6.4 Beam Dithering

Beam dithering is an alternative method to regression for correcting detector asymmetries. The coefficients of Equation 6.7 are found by intentionally moving the beam with corrector magnets and observing the detector correlation with the beam monitors. Figure 6.4 depicts

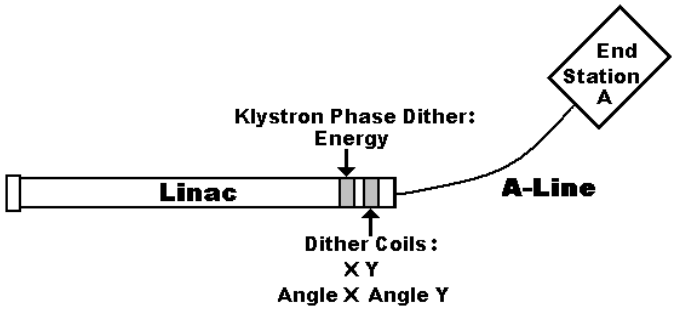

Figure 6.4: Location of components used for beam dithering.

the location of the linac components used for beam dithering. Corrector magnets located in the final sectors of the linac are used to vary both beam position and angle, by an amount several times the natural beam jitter. The energy is varied by adjusting the phase of a klystron in the same region. Figure 6.5 depicts the response of one of the lumi chambers to an x-position dithering cycle[1].

The beam parameters were typically dithered 4% of the time. This data is only used for the determination of correction slopes and is removed from the production data. The

[1]The slowly varying dither cycle depicted in the figure was found to be very disruptive to the beam feedbacks. For the production data, a more rapid dithering style was employed.

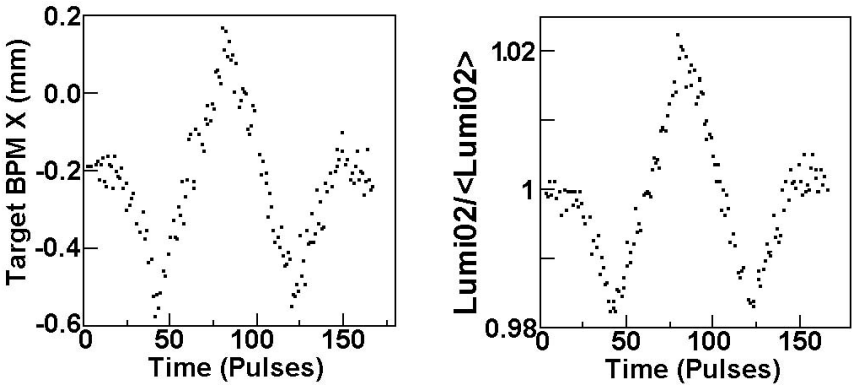

Figure 6.5: A lumi chamber responding to a position dither cycle.

response of the detectors to the dithered beam parameters is found in a manner similar to the regression method, by a multidimensional fit to the data in which dithering is occurring (Equation 6.10). The detector asymmetry is then corrected as in Equation 6.7. Because both the lumi and Out detector require a correction for charge, a regression against charge is done after the other beam coefficients are computed.

In contrast to the regression procedure, dithering varies the beam parameters in a charge independent way. By decoupling the parameters, the dithering results are less prone to systematic effects. However, dithering was not always functional, while the regression procedure can always be performed. Therefore, the main results for the E158 experiment are computed using regression, while the dithering results are used as a cross-check.

6.5 Data Selection

The quality of the data used in the asymmetry analysis is ensured by removing pulses that do not pass predetermined criteria [39]. To avoid biasing the data, many of the data cuts also remove a certain number of pulses before and after an offending pulse. The following paragraphs describe each of the requirements employed in the asymmetry analysis.

General: The primary quality cut is composed of several separate cuts that are always made in the analysis. The first ensures that the beam parameters of charge, energy, X and Y position, and X and Y angle are within six standard deviations of the mean value. The second removes all data with large excursions due to beam dithering. The third cut ensures that the time between beam pulses is the same for each pulse in the pulse pair, to combat possible hysteresis effects. The final cut requires that the agreement of the charge asymmetry measurements of the toroids upstream of the target be within 1000 ppm, roughly 20 standard deviations. Any pulse pair not meeting these criteria is removed, as well as the 50 preceding and subsequent pulse pairs. Overall, this cut retains 90.8% of the data.

Position Jitter: Pulse pairs with position jitter greater than nine standard deviations from zero are removed, as well as the 50 preceding and following pulse pairs. The cut has a 91.9% retention rate.

Energy Stability: The momentary loss of a klystron in the linac is not uncommon. Depending on the phase of the missing klystron, the energy of the beam can either increase or decrease, usually by an amount of $\approx$ 200 MeV. Off-energy pulses are removed by checking for large deviations in the E158 energy BPM. The cut has a window of $\pm$ 50 pulse-pairs, and has a retention rate of 97.7%.

BPM Phase: The resolution of the BPMs decreases when the phase of the local oscillator drifts. This cut uses the Q cavity of each BPM to ensure that the phase is within an acceptable range. The time structure for the phase drifts causes this cut have a window from 5 pulse pairs before the offending pulse to 50 pairs after. The retention rate is 97.4%.

BPM Linearity: Large offsets, on the scale of a few millimeters, cause the BPM response to become non-linear. This cut ensures that the beam position is within a range where the BPMs are linear to better than 99%. The cut window is from two pulse pairs before the offending pulse to 4 pulse pairs after. The retention rate is 97.0%.

Charge: The beam charge is required to be greater than 10^{11} electrons per pulse, about 20% of the normal beam current. Pulses with low charge are fundamentally different from the standard beam pulses, and are excluded. The cut only removes one pulse pair. The retention rate is 98.1%.

Transmission: The transmission from the source to the E158 target is required to be greater than 90%. Like low-current pulses, low-transmission pulses are very different from normal beam pulses and are removed. The retention rate is 99.9%.

Source Voltages: Data in which the CP and PS Pockels cell voltages are improperly set at the source are excluded by this cut. When the voltages are incorrect, the polarization of the beam is unknown. The retention rate is 99.3%.

Timeslot: While the beam repetition rate is 120 Hz, the electric power for the accelerator is at the normal 60 Hz rate. The position of the beam pulses in time relative to the phase of the electric power can therefore assume two states, which are called timeslots. Because it is possible that the two timeslots have different properties, this cut requires that each pulse in a pair occur in the same timeslot. The retention rate is 98.9%.

Slopes: The regression coefficients used to correct the detector asymmetries are calculated in chunks for 10,000 pulse pairs, sorted by timeslot. It is possible that one timeslot can dominate a period of time so that the other timeslot has very few pulses. If the smaller

timeslot has less than 100 pairs, this cut removes that timeslot because its regression slopes would be unreliable. The retention rate is 99.2%.

All Cuts The total data retention rate when all cuts are employed is 73.5%.

Careful studies were done on the Run I Møller detector asymmetry result in which cuts were included or removed to observe their effect on the mean asymmetry. In all cases it was found that the cuts do not bias the data in any discernible way.

6.6 Møller Detector Asymmetry Analysis

The regression corrected Møller detector asymmetry distribution defined by Equation 6.7 is used to determine a mean asymmetry A_i and statistical uncertainty σ_i for each data run consisting of roughly 200,000 pulse pairs. The results of N individual data runs can be combined to compute the average asymmetry $A_{average}$ and uncertainty $\sigma_{average}$, with

$$A_{average} = \frac{\sum_{i=1}^{N} \frac{A_i}{\sigma_i^2}}{\sum_{i=1}^{N} \frac{1}{\sigma_i^2}} \tag{6.11}$$

and

$$\sigma_{average} = \sqrt{\frac{1}{\sum_{i=1}^{N} \frac{1}{\sigma_i^2}}}. \tag{6.12}$$

Figures 6.6 and 6.7 present the results obtained with the Møller detector for all of Run I and Run II, respectively. The data has been averaged into periods of data called "slugs," which are runs with the same beam energy and source halfwave plate setting. (The different energy and halfwave plate states are used to combat systematic effects, and are described in the following section.) Both Run I and Run II are comprised of approximately the same amount of data, though Run II has less systematic reversals.

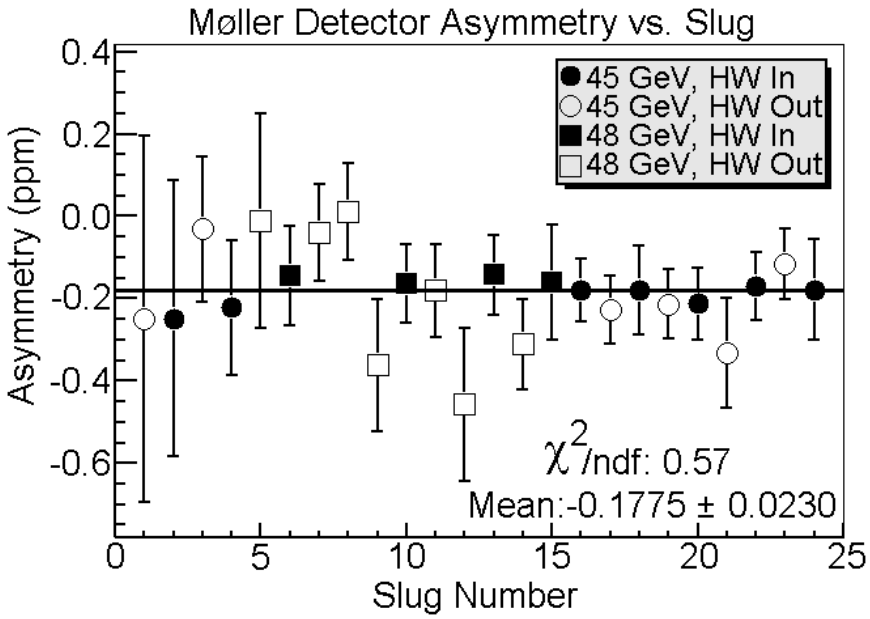

Figure 6.6: Run I Møller detector asymmetry versus slug.

The Run I and Run II plots have reasonable χ^2/ndf and their means agree within statistical fluctuations. The clear asymmetry in both plots represents the first observation of parity violation in Møller scattering.

The data plotted in Figures 6.6 and 6.7 are purely statistical averages that do not include systematic uncertainties such as beam polarization, regression correction uncertainties, and background corrections. These issues are discussed in Section 6.8 to arrive at A^{PV}.

6.6.1 Systematic Reversals

The experiment utilized two distinct methods to reduce sensitivity to helicity-correlated systematic effects [37]. The first involved running with two different source halfwave plate states (Section 3.1.4). Inserting the waveplate reverses the helicity of the laser light hitting the cathode while keeping the rest of the source setup the same. The second method involved running at two separate beam energies, 45 GeV and 48.3 GeV. The difference in these energies represents a 180° g-2 rotation of the electron spin as it traverses the A-Line

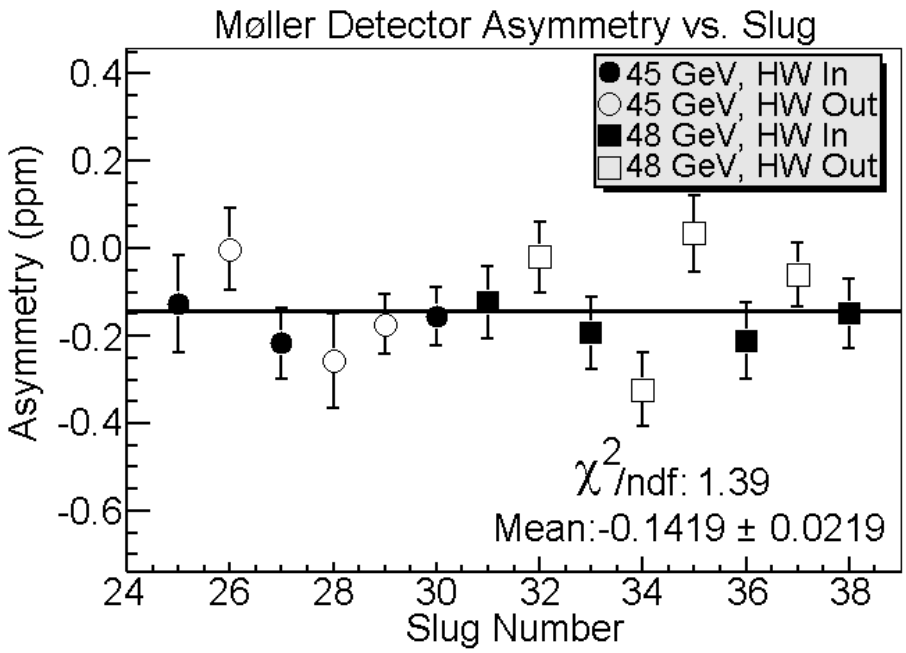

Figure 6.7: Run II Møller detector asymmetry versus slug.

bend leading up to End Station A.

The four possible apparatus configurations combine the physics asymmetry A^{PV} with two types of helicity-correlated systematic effects denoted as A^1_{sys} and A^2_{sys}. The asymmetry A^1 refers to systematic effects that are not affected by the waveplate state, such as electronics cross-talk with the bias voltage of the CP cell at the source (Section 3.1). The asymmetry A^2 refers to effects like residual linear polarization in the laser light at the source that can also reverse sign with the insertion of the source halfwave plate. The four configurations are then given by

$$\begin{aligned} A^{45}_{Out} &= A^{PV} + A^1_{Sys} + A^2_{Sys} \\ A^{45}_{In} &= A^{PV} - A^1_{Sys} + A^2_{Sys} \\ A^{48}_{Out} &= A^{PV} - A^1_{Sys} - A^2_{Sys} \\ A^{48}_{In} &= A^{PV} + A^1_{Sys} - A^2_{Sys}, \end{aligned} \tag{6.13}$$

(6.14)

where $A_{Halfwave}^{Energy}$ denotes the overall asymmetry seen with the Møller detector for each energy and halfwave plate setting. By collecting the same amount of data in each state, systematic effects are minimized. Run II had less systematic reversals than Run I and will be shown to have larger systematic effects, discussed in Section 6.7.2.2.

Figure 6.8 presents the Møller detector asymmetry obtained for each energy-halfwave plate configuration in Run I and Run II. All of the states agree well, indicating that there are no large systematic effects. Figures 6.9 and 6.10 present the same data as the previous plots, but without the systematic reversal sign flips taken into account. They provide another visual indication that systematic uncertainties are below the level of statistical fluctuations for the Møller detector.

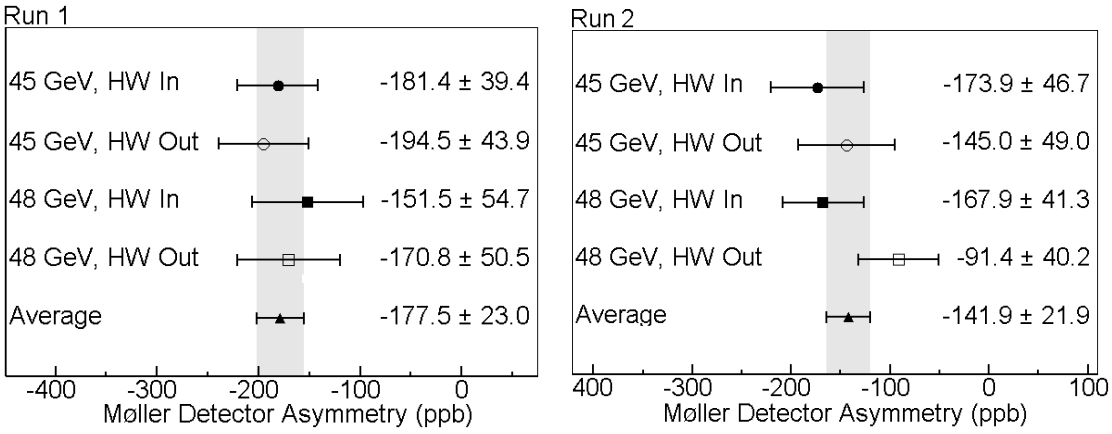

Figure 6.8: Measured asymmetry for each energy-halfwave plate setting.

6.6.2 Beam Corrections

Because beam monitors are used to modify the raw Møller detector asymmetry through Equation 6.7, beam asymmetries lead to a correction of the detector asymmetry. Table 6.2

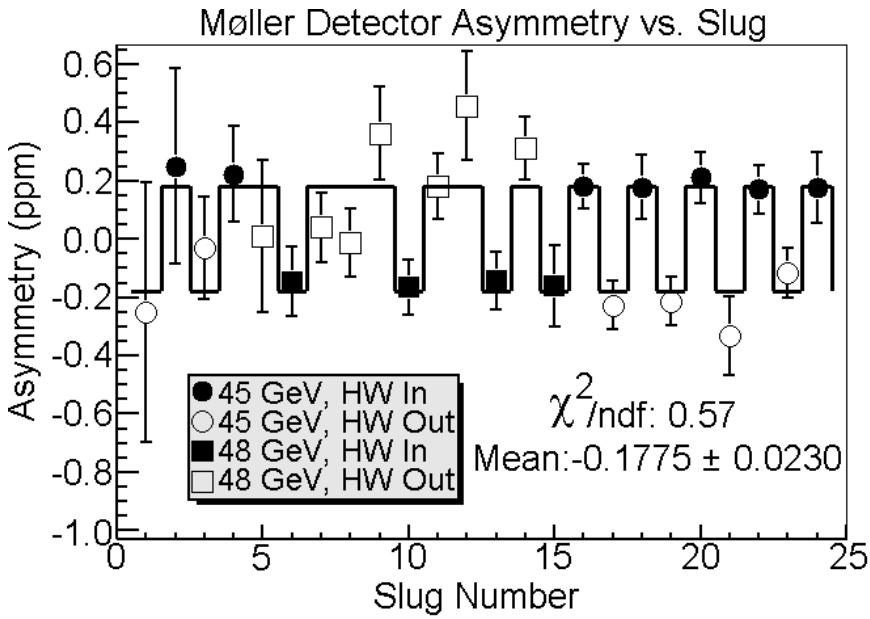

Figure 6.9: Run I Møller detector asymmetry versus slug, sign flips suppressed.

Run I	
Parameter	Correction (ppb)
Charge	0.2
Energy	5.1
X	6.7
Y	0.05
X Angle	23.8
Y Angle	2.0
Total	37.9

Run II	
Parameter	Correction (ppb)
Charge	-1.8
Energy	29.0
X	-3.7
Y	-10.5
X Angle	17.1
Y Angle	-8.9
Total	21.2

Table 6.2: Beam corrections to A^{Raw} of the Møller detector.

lists the beam corrections for Run I and Run II. Note that the corrections have no uncertainty: they are exactly the amount the beam monitors have shifted the raw Møller detector asymmetry. The contribution to the uncertainty on the Møller asymmetry enters through the systematic uncertainty associated with the method itself and is discussed in Section 6.7.2.2.

The agreement between the corrected detector asymmetry obtained with regression and dithering is an important measure of potential systematic uncertainties. Table 6.3 compares the asymmetries obtained with the two methods. The values differ slightly from the

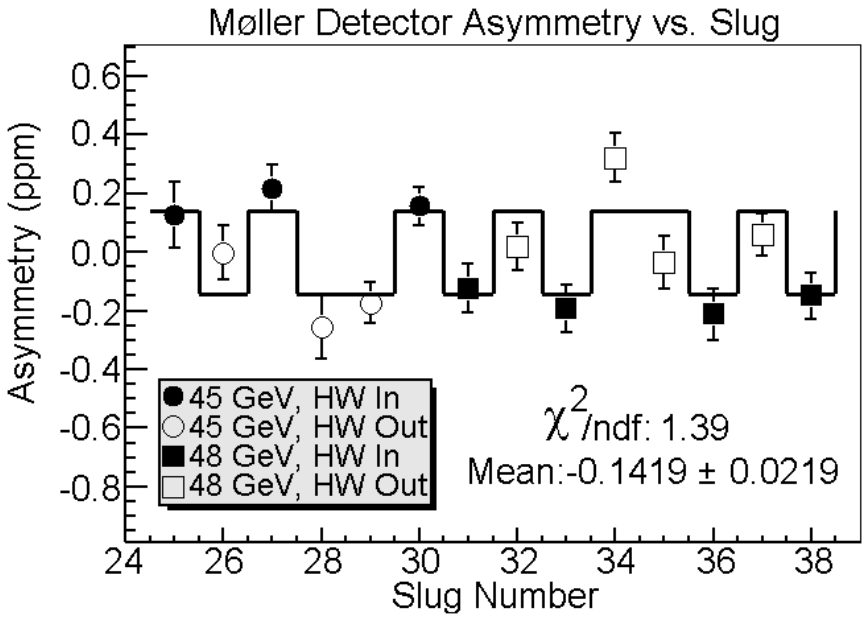

Figure 6.10: Run II Møller detector asymmetry versus slug, sign flips suppressed.

Run I	Asymmetry (ppb)	Correction (ppb)
Regression	-179.1 ± 24.3	30.6
Dithering	-182.2 ± 27.0	27.5
Run II	Asymmetry (ppb)	Correction (ppb)
Regression	-150.0 ± 22.3	11.5
Dithering	-154.8 ± 22.7	6.7

Table 6.3: Comparison of regression and dithering results for the Møller detector asymmetry.

averages shown in Figure 6.6 and 6.7 because only the subset of data in which dithering was functional was used. The improvement in the Møller detector resolution is less for dithering, as indicated by the uncertainty on the asymmetry. The most likely cause is that the dithering correlation slopes are computed less often than the regression slopes. In both Run I and Run II, the methods agree to the level of a few ppb, indicating that systematic differences between the methods are small. However, Section 6.7.2.2 will demonstrate that the total systematic uncertainty contribution to A^{PV} due to beam corrections is dominated by a systematic effect common to both regression and dithering.

6.7 Asymmetry Corrections and Uncertainties

The parity-violating asymmetry A^{PV} is obtained from the beam corrected Møller detector asymmetry $A^{Measured}$ by accounting for contributions from backgrounds and taking into account scale factors. The asymmetries are related through

$$A^{PV} = \frac{1}{P\lambda}\frac{A^{Measured} - \sum_i f_i A_i}{1 - \sum_i f_i}, \tag{6.15}$$

where the sums are taken over all backgrounds. The f_i terms represent the dilution factors of the backgrounds, defined as the ratio of the background signal to the total signal seen in the Møller detector. The helicity-dependent asymmetries of the backgrounds are represented by the A_i terms. The scale factors are the beam polarization P and the linearity of the detector λ. Sections 6.7.1 through 6.7.8 detail the components of Equation 6.15 for the Møller detector. Section 6.8 then uses the results to compute A^{PV} for Run I and Run II.

6.7.1 The Electron-Proton Scattering Correction

The spectrometer (Section 3.7) is designed to provide separation of electron-electron and electron-proton (eP) scattering events. However, the separation is not perfect, and some electron-proton events are registered in the Møller detector. In particular, inelastic eP events are expected to have an asymmetry an order of magnitude larger than A^{PV}. It is therefore crucial to account for the eP background contamination in $A^{Measured}$.

The amount of eP signal in the Møller detector is determined from a Monte Carlo simulation of the E158 spectrometer [43]. The simulation is configured to match the maps of the signal flux versus radius, provided by the profile monitor (Section 4.3). Figure 6.11 depicts a comparison between the simulation and a profile scan with typical running condi-

tions. Figure 6.12 presents a scan with the insertable acceptance collimator (Section 3.7.4) in place. The additional separation of the Møller from the electron-proton scattering events is important for ensuring that the simulation matches the reality of the signal distribution. In both plots, the agreement between the simulation and the actual data is reasonable.

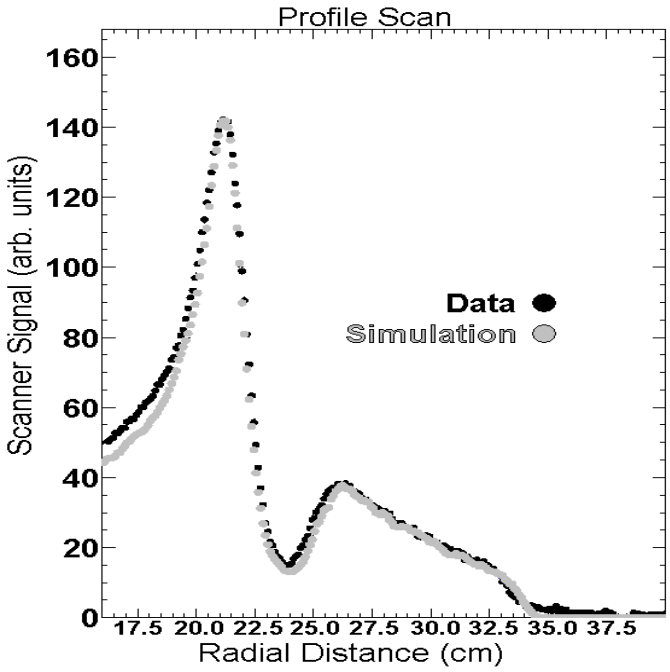

Figure 6.11: Data and simulation comparison with normal running conditions.

Because the difference between the data and the simulation is small, the simulation can be used to quantify the eP contamination in the Møller detector. Figure 6.13 displays a profile scan with the electron-electron and electron-proton contributions separated in the simulation.

Table 6.4 presents the dilution factors f used for determining the correction to $A^{Measured}$ for the electron-proton contribution in Equation 6.15. The ratio of elastic to inelastic events R is also shown. The uncertainty on the results was determined by varying the input parameters of the simulation within a reasonable range.

The Run I and Run II results differ for two reasons. First, the eP collimator (Sec-

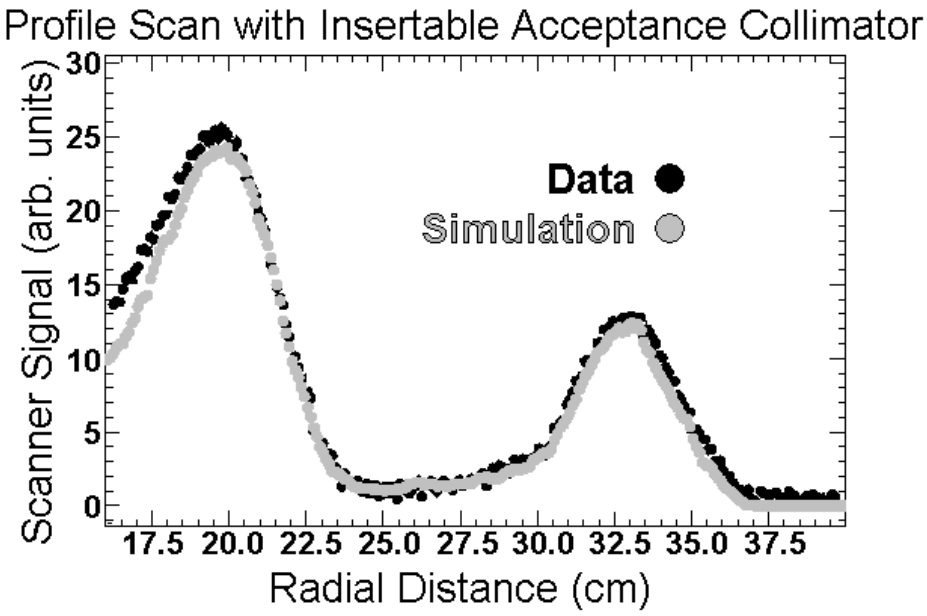

Figure 6.12: Data and simulation comparison with the insertable acceptance collimator in position.

tion 3.7.5) was only used in Run II. The collimator blocks the eP detector and most of the Out ring. Second, the quadrupole magnet settings of the spectrometer were changed between Run I and Run II to de-emphasize the Out ring of the detector.

The value of $A^{Measured}$ must also be corrected for the asymmetry contribution of the electron-proton scattering background. The asymmetry result of the eP detector in Run I is used as an input to the simulation. The flux in the eP detector is approximately 70%

Run I	45 GeV			48 GeV		
Detector	f	σf	R	f	σf	R
In	0.0969	0.0099	7.4	0.0861	0.0087	6.8
Mid	0.0684	0.0079	5.7	0.0610	0.0071	5.1
Out	0.1401	0.0203	4.4	0.1903	0.0261	4.0
Run II	45 GeV			48 GeV		
Detector	f	σf	R	f	σf	R
In	0.0810	0.0095	7.1	0.0780	0.0079	6.1
Mid	0.0540	0.0067	5.8	0.0520	0.0053	5.5
Out	0.1020	0.0143	4.9	0.0810	0.0153	4.4

Table 6.4: Dilution factors f due to background eP scatters. R is the ratio of elastic to inelastic eP signals.

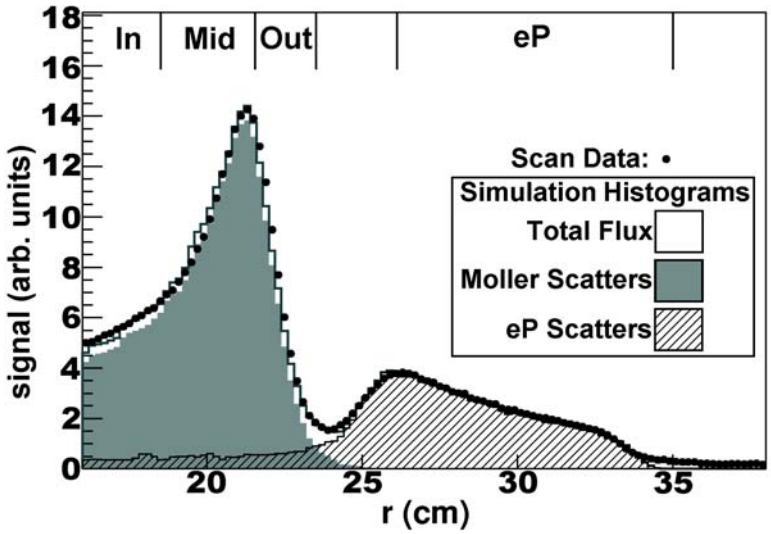

Figure 6.13: Profile scan with the Møller and electron-proton scattering simulation results superimposed.

Run I	45 GeV		48 GeV	
Detector	fA	σfA	fA	σfA
In	-33.4	4.7	-35.5	4.8
Mid	-32.2	5.2	-33.8	5.8
Out	-86.9	22.3	-140.2	33.1

Run II	45 GeV		48 GeV	
Detector	fA	σfA	fA	σfA
In	-29.4	4.6	-33.2	4.6
Mid	-26.5	3.8	-27.5	3.8
Out	-57.5	9.0	-52.4	9.2

Table 6.5: Diluted asymmetries fA due to the electron-proton scattering background. All entries are in ppb.

elastic eP scatters, 27% inelastic eP scatters, and only about 3% Møller scattered electrons. However, the asymmetry associated with the inelastic eP events is roughly 25 times larger than the elastic asymmetry, so these events dominate.

Figure 6.14 depicts the asymmetry measured with the eP detector for Run I. The Q^2 is sufficiently different between the two beam energies that they are averaged separately. The result is consistent with the theoretical estimate [68].

Table 6.5 details the diluted asymmetry fA due to the electron-proton scattering background used to correct $A^{Measured}$. The large uncertainty on the Run I result for the Out ring is dominated by the simulation of the shower sharing with the eP detector. In Run II, the eP collimator greatly suppresses the effect, reducing the systematic uncertainty.

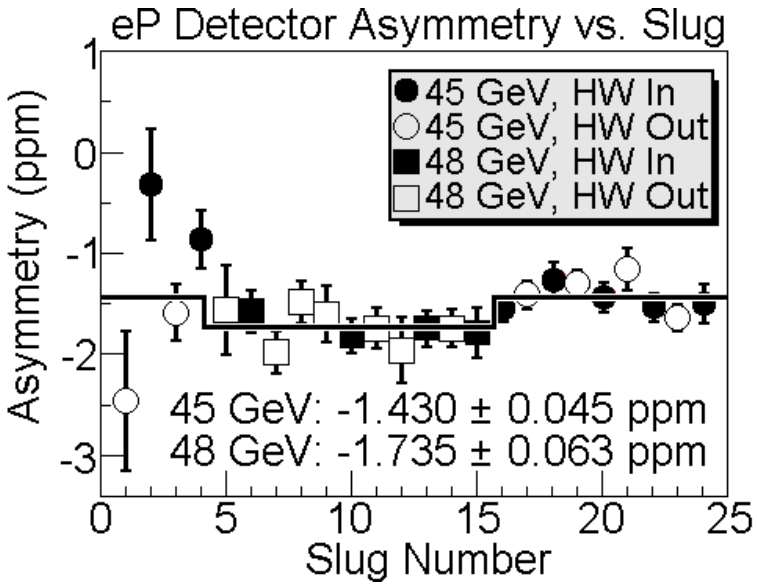

Figure 6.14: Asymmetry result from the eP detector in Run I.

6.7.2 Beam Asymmetry Correction Systematic Uncertainties

The regression corrections given in Equation 6.7 must be assigned a systematic uncertainty contribution to A^{PV}. Examining Equation 6.15, the uncertainty can be accommodated formally as a correction with zero dilution f or asymmetry fA, but with an uncertainty σfA.

The systematic uncertainty estimate is divided into two pieces: first-order and higher-order effects. The following sections will demonstrate that while the In and Mid regions of the detector are fairly insensitive to the beam correction systematic effects, the Out ring is dominated by the higher-order effects. Because of the large uncertainty from this effect, the Out ring is not included with the In and Mid ring in the calculation of A^{PV}.

6.7.2.1 First-Order Beam Correction Systematic Uncertainties

The first-order systematic uncertainty assigned to the values in Table 6.2 is found by enhancing the Møller detector sensitivity to the regression parameters by re-weighting the

Regression Coefficients			
Parameter	Monopole	X-Dipole	Y-Dipole
Q (ppm/ppm)	0.005	0.012	0.005
E (ppm/MeV)	-25.9	-2.6	-10.0
X (ppm/μm)	0.5	-22.1	-0.8
Y (ppm/μm)	-1.2	-1.6	24.0
dX (ppm/μR)	-66.1	-30.8	-31.0
dY (ppm/μR)	7.3	18.9	151.7

Table 6.6: Regression coefficients of three Mid detector weighting schemes.

detector channels. In general, the asymmetry A for any weighting pattern is defined as

$$A = \frac{1}{\sqrt{N \sum_{i=1}^{N} w_i^2}} \sum_{1}^{N} w_n A_n, \tag{6.16}$$

where A_n refers to the asymmetry of channel n, with weight w_n [70]. The sums are taken over the N channels of the detector. The most relevant weighting scheme is the dipole pattern, with weights given by

$$w_n^{Dipole} = \sin(\frac{2\pi n}{N}). \tag{6.17}$$

Assigning $n = 0$ as the top of the detector, this scheme produces enhanced sensitivity to beam motion in the horizontal direction and is known as the X-Dipole pattern. Rotating by 90°, the pattern becomes a Y-Dipole. Table 6.6 displays the regression coefficients of the Mid ring Monopole, Mid X-Dipole, and Mid Y-Dipole weighting schemes.

The monopole weighting scheme is dominated by the energy parameter, while the X and Y dipoles are dominated by the spatial parameters their names suggest. Owing to their increased sensitivity, specific weighting schemes are employed to estimate the systematic uncertainty inherent in the regression method. Table 6.7 relates the patterns that were especially sensitive to each of the beam parameters[2].

[2]The Q parameter is excluded in the first-order systematic uncertainty estimate. It is more relevant for the higher-order uncertainty discussed in Section 6.7.2.2.

Sensitive Weighting Schemes	
Parameter	Detector
E	Møller Monopole
X	Mid X-Dipole
Y	Mid Y-Dipole
dX	Out X-Dipole
dY	Out Y-Dipole

Table 6.7: Sensitive pattern-weighted detectors for the regression beam parameters.

The first order systematic uncertainty on the beam corrections is estimated by using the sensitive monitors in Table 6.7 to compute the relative error ϵ_n on each of the n beam corrections. Two separate sets of data, denoted by the superscripts, are used to determine the relative uncertainty through

$$\epsilon_n = \frac{A_n^1 - A_n^2}{corr_n^1 - corr_n^2} \rightarrow \frac{\partial A_n}{\partial corr_n}, \tag{6.18}$$

where A_n is the mean asymmetry of the detector weighting pattern sensitive to the n^{th} beam parameter, and $corr_n$ refers to the beam correction of A_n. To ensure that first order effects dominate, the two data sets are chosen as the two timeslots in the data slug with the largest difference in the beam corrections.

The first-order systematic uncertainty δ_n for the correction $corr_n$ is the product of the relative uncertainty with the value of the correction:

$$\delta_n = \epsilon_n corr_n. \tag{6.19}$$

Tables 6.8 and 6.8 display the systematic uncertainty calculated for each regression parameter using this method for both Run I and Run II. To be conservative, the value quoted as the relative error is the magnitude of the error found using Equation 6.18, plus one standard deviation. The uncertainty on the total correction is found as the quadrature

Run I			
Parameter	Correction (ppb)	Relative Error ϵ (%)	Uncertainty δ (ppb)
E	5.1	7.0	0.36
X	6.7	8.7	0.58
Y	0.1	10.1	0.01
dX	23.8	3.9	0.92
dY	2.0	22.3	0.45
			Total: 1.2

Table 6.8: Run I first-order systematic uncertainties in the regression corrections to the raw Møller detector asymmetry.

Run II			
Parameter	Correction (ppb)	Relative Error ϵ (%)	Uncertainty δ (ppb)
E	29.0	10.0	2.00
X	-3.7	3.8	0.17
Y	-10.5	2.8	0.31
dX	17.1	3.6	0.69
dY	-8.9	5.7	0.55
			Total: 3.0

Table 6.9: Run II first-order systematic uncertainties in the regression corrections to the raw Møller detector asymmetry.

sum of the individual uncertainties. In both data sets, the total first-order systematic uncertainty is small.

6.7.2.2 Higher-Order Beam Correction Systematic Uncertainties

The plots of the Møller asymmetry versus slug shown in Figures 6.6 and 6.7 have χ^2/ndf near unity, and the systematic reversal plots of Figure 6.8 show no indication that large systematic uncertainties are present. However, when the Out ring is examined in the same manner, it is clear that there are possible systematic effects that need to be addressed.

Figures 6.15 and 6.16 present the Out ring asymmetry data. The Run I slug plot has an elevated χ^2/ndf, but still looks reasonable. The Run I systematic reversal plot appears to have some cancellation of an effect between the 48 GeV-Halfwave Out and 45 GeV-Halfwave Out detector results. In the Run II plots, however, it is clear that there

are systematic effects not removed by the regression method. The degree to which this unregressed systematic effect can influence the Møller detector asymmetry must be assigned a systematic uncertainty.

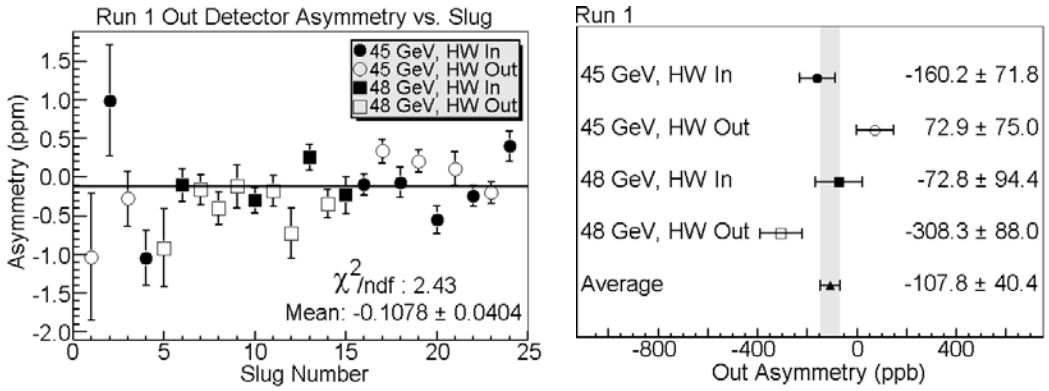

Figure 6.15: Run I Out ring asymmetry data.

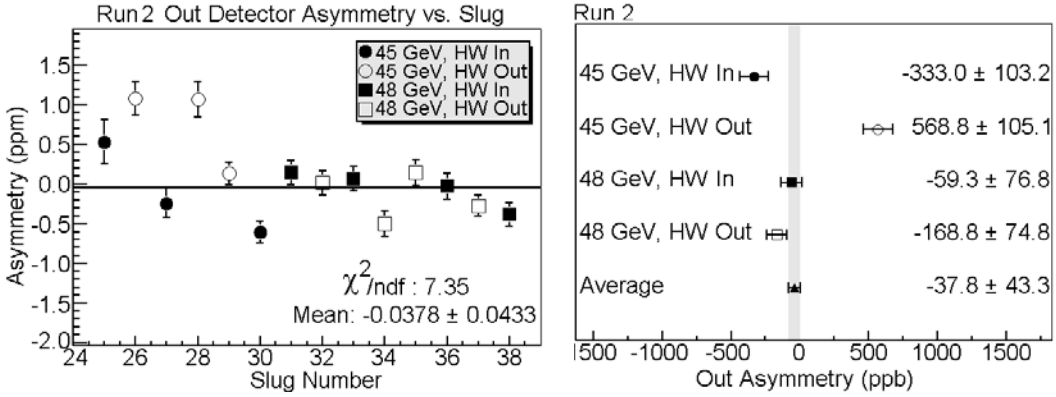

Figure 6.16: Run II Out ring asymmetry data.

The nature of the systematic effect was isolated in Run III of the E158 experiment. In addition to the normal setup, the BPM signals were also "sliced" in time and fed to four different ADC channels. That is, the first quarter of the pulse went to the first channel, and so on. Effectively, this allows for regression against the shape of the beam pulse. The Run III Out ring data look similar to Run II, with poor fits when the normal analysis is employed. However, when regression against the sliced BPM signals is included, the Out

data are greatly improved, with a χ^2/ndf near unity [72]. Therefore, the cause of the Out detector systematic effect is found to be intra-pulse helicity-correlated asymmetries which are not removed by the normal regression procedure in Run I and Run II.

The nature of the effect can be understood by the following simple description. The BPMs measure the average position X of the electron beam pulse[3], given by

$$X = \frac{1}{T}\int_0^T x(t)dt, \tag{6.20}$$

where the integral is over the duration of the pulse T and x is the beam position. The regression procedure then corrects the raw detector asymmetry A^{Raw} by multiplying the beam difference ΔX by a constant coefficient c, as in Equation 6.7. The correction C is then given as

$$C = \frac{c}{T}\int_0^T x_1(t) - x_2(t)dt, \tag{6.21}$$

where the subscripts refer to the beam pulses of the pulse pair. The method is valid unless the detector sensitivity to the beam varies over the course of the beam pulse. In that case, the constant c becomes a function of position, and actually needs to be integrated as

$$C = \frac{1}{T}\int_0^T c(x_1)x_1(t) - c(x_2)x_2(t)dt. \tag{6.22}$$

Effectively, this is what "slicing" the BPM signals does: it allows for the detector sensitivity to vary over the course of the beam pulse.

A possible mechanism for this to occur is known as "tail wagging," where the tail of the beam pulse has large fluctuations due to the passage of the head of the pulse through

[3]Technically, the BPMs measure the charge-averaged position. The formula could be corrected by x(t) $\rightarrow \rho$(t)x(t), where ρ is the charge density. However, for clarity, the charge dependence is omitted.

the linac. This is known as the "wakefield effect," where the electromagnetic "wake" of the head of the pulse disrupts the tail [73, 74]. The effect could be on the scale of hundreds of microns, which would indeed produce large effects in the Out ring, due to its sensitive geometry [75]. If the intra-pulse effects are also helicity-correlated, the asymmetry results are not fully corrected, as seen in the Out ring results in Figure 6.15 and 6.16.

Because there were no "sliced" BPM signals in Run I and Run II, the systematic uncertainty due to higher-order effects can only be estimated. Because the plots of the Møller detector asymmetry versus slug look normal, it is expected that the sensitivity to higher-order effects should be small. First, it is assumed that the measured asymmetry $A^{Measured}$ is related to the real asymmetry A^{Real} through

$$A^{Measured} = A^{Real} + \alpha A^{sys}, \tag{6.23}$$

where A^{sys} is the asymmetry due to beam-related systematic effects, and α is the detector sensitivity to A^{sys} [76]. If two detectors are examined, Equation 6.23 can be used to find

$$\alpha_1 A^{sys} \equiv \sigma^1_{sys} = \frac{\alpha_1}{\alpha_1 - \alpha_2}((A_1^{Measured} - A_2^{Measured}) - (A_1^{Real} - A_2^{Real})), \tag{6.24}$$

where the subscripts denote the detectors and σ^1_{sys} is the systematic uncertainty assigned to detector 1. If we choose the Møller detector as the first detector and the Out ring as the second, we have

$$A_1^{Real} - A_2^{Real} = \Delta eP, \tag{6.25}$$

where ΔeP represents the difference in the correction for the electron-proton scattering background between the two detectors. The only unknown values are then α_1 and α_2,

Systematic Uncertainty Estimates (ppb)		
	Run I	Run II
ΔeP	60.6 $\pm$ 26.1	21.1 $\pm$ 5.6
$A_1^{Measured} - A_2^{Measured}$	-69.7 $\pm$ 46.5	-104.1 $\pm$ 48.5
$\frac{\alpha_1}{\alpha_2}$	-0.064	-0.058
$\sigma_{sys}^{M\o ller}$	**-7.8$\pm$3.2**	**-6.9$\pm$2.7**

Table 6.10: The higher-order systematic uncertainty computed for the Møller detector, comparing the Møller detector (1) and the Out ring (2), assuming Equation 6.26.

which can only be estimated.

One method is to note that the Out ring has a large charge regression coefficient (Table 6.1), between five and ten times larger than would be expected (Section 5.10.1). Because most beam parameters are correlated to charge, it is reasonable to assume that the charge coefficient is a measure of the size of the systematic effect.

As an estimate, it is assumed that the α systematic coefficient is proportional to the charge regression coefficient c_Q. The ratio of the sensitivity to the systematic effect of the two detectors is then

$$\frac{\alpha_1}{\alpha_2} = \frac{c_Q^1}{c_Q^2}. \tag{6.26}$$

With Equation 6.25 and the assumption of Equation 6.26, the systematic uncertainty contribution for the Møller detector can be found with Equation 6.24. Table 6.10 represents the Møller systematic uncertainty found for Run I and Run II using this method.

Because Equation 6.26 is an assumption, it is useful to estimate the ratio $\frac{\alpha_1}{\alpha_2}$ by an alternative method. The uncertainty on $A^{Measured}$ in Equation 6.23 is

$$\sigma^2_{A^{Measured}} = \sigma^2_{A^{Real}} + \alpha^2 \sigma^2_{A^{sys}}. \tag{6.27}$$

Systematic Uncertainty Estimates (ppb)		
	Run I	Run II
ΔeP	60.6 $\pm$ 26.1	21.1 $\pm$ 5.6
$A_1^{Measured} - A_2^{Measured}$	-69.7 $\pm$ 46.5	-104.1 $\pm$ 48.5
$\frac{\alpha_1}{\alpha_2}$	0 $\pm$ 0.062	-0.141 $\pm$ 0.016
$\sigma_{sys}^{M\o ller}$	**0 $\pm$ 8.1**	**-15.5 $\pm$ 6.2**

Table 6.11: The higher-order systematic uncertainty computed for the Møller detector, comparing the Møller detector (1) and the Out ring (2), using Equation 6.29.

Again using two detectors denoted by 1 and 2, the ratio of the α coefficients is

$$\left|\frac{\alpha_1}{\alpha_2}\right| = \sqrt{\frac{\sigma^2_{A_1^{Measured}} - \sigma^2_{A_1^{Real}}}{\sigma^2_{A_2^{Measured}} - \sigma^2_{A_2^{Real}}}}, \tag{6.28}$$

which can be approximated as

$$\left|\frac{\alpha_1}{\alpha_2}\right| = \frac{\sigma_{A_1^{Measured}}}{\sigma_{A_2^{Measured}}}\sqrt{\frac{\chi^2_{ndf1} - 1}{\chi^2_{ndf2} - 1}}. \tag{6.29}$$

Geometry causes the regular regression coefficients for the Møller and Out detectors to be anti-correlated, so it is reasonable to assume that $\frac{\alpha_1}{\alpha_2}$ is negative. When one of the detectors has a $\chi^2_{ndf} < 1$, the method breaks down, because no systematic effects can be discerned. Therefore, it is also useful to calculate the uncertainty on Equation 6.29:

$$\sigma\left(\frac{\alpha_1}{\alpha_2}\right) = \frac{\sigma_{A_1^{Measured}}}{\sigma_{A_2^{Measured}}}\sqrt{\frac{1}{2ndf}}\frac{\chi^2_{ndf1} - 1}{\chi^2_{ndf2} - 1}\sqrt{\frac{1}{(\chi^2_{ndf1} - 1)^2} + \frac{1}{(\chi^2_{ndf2} - 1)^2}}. \tag{6.30}$$

Using Equations 6.29 and 6.30, a table similar to Table 6.10 can be constructed. Table 6.11 presents the results found with this method.

To be consistent with the two methods, the systematic uncertainty estimate for Run I is set to 10 ppb, while for Run II it is 15 ppb. The data in Run III is still being analyzed, but preliminary findings indicate that the results of Table 6.10 and Table 6.11 are an

overestimate of the higher-order beam correction systematic uncertainty for the Møller detector [72].

6.7.3 Dipole Asymmetry

A transversely polarized electron beam scattering off unpolarized electrons produces an asymmetry with azimuthal dependence at the Møller detector. The effect is purely electromagnetic, due to a two photon exchange box diagram [77]. Data taken at 46 GeV, where the beam was measured to be 85% transversely polarized in the horizontal direction, clearly show the effect. Figure 6.17 plots the asymmetry measured in the Mid ring versus channel number for the transverse polarization data.

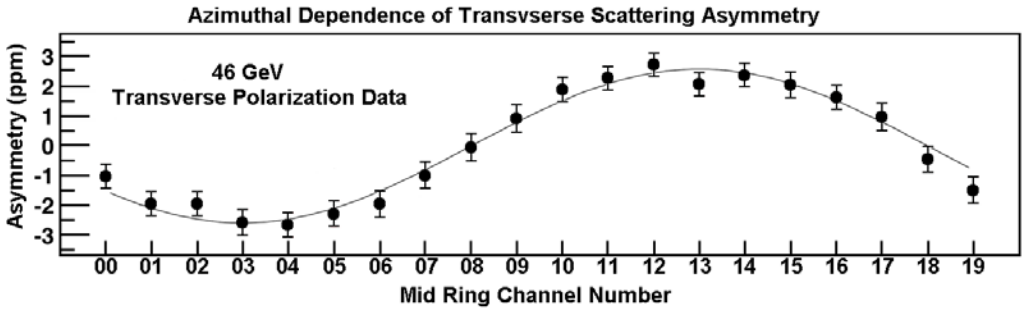

Figure 6.17: Run I asymmetry plotted versus channel number for 46 GeV running.

Production data is taken with a longitudinally polarized beam, though residual transverse polarization at the level of a few percent is possible. Figure 6.18 depicts the asymmetry versus azimuth taken from the production data. Comparing the amplitudes of Figures 6.17 and 6.18 indicates that the beam is $\approx 5\%$ transversly polarized during normal production running, consistent with reasonable expectations.

The effect is purely electromagnetic, and so averages exactly to zero over the full azimuth. However, the Møller channels are statistically weighted, spoiling the azimuthal symmetry of the detector. The dipole pattern of Figure 6.18 can then contaminate the

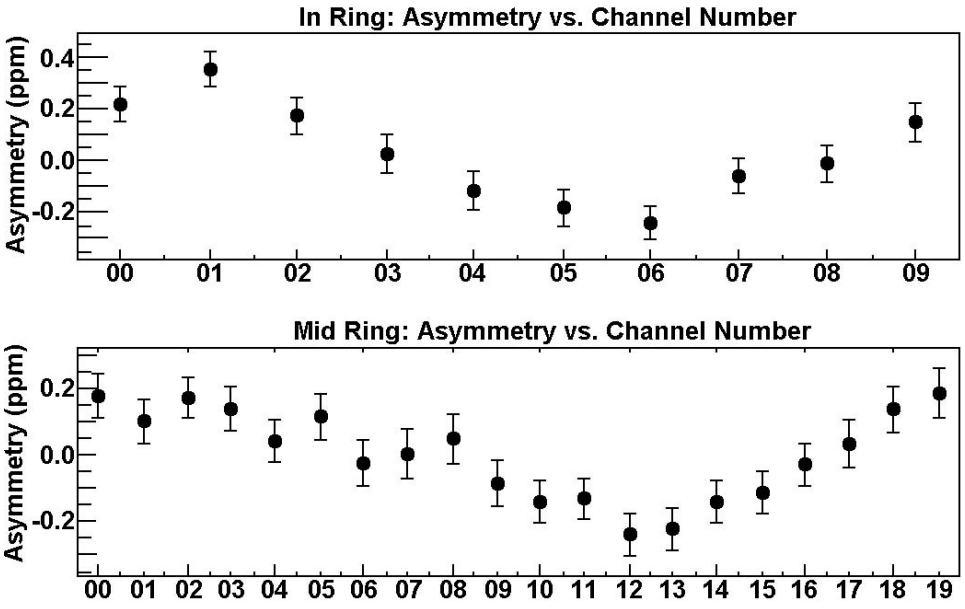

Figure 6.18: Run I asymmetry plotted versus channel number for production data.

Møller asymmetry result. Because the signal flux distribution is well centered on the face of the Møller detector, the degree to which the dipole pattern shifts the asymmetry result of each ring of the detector δ can be quantified by

$$\delta_X = A_X \sum_{i=1}^{N} w_i \sin(\frac{2\pi i}{N}) \tag{6.31}$$

and

$$\delta_Y = A_Y \sum_{i=1}^{N} w_i \cos(\frac{2\pi i}{N}), \tag{6.32}$$

where A refers to either the X or Y amplitude of the oscillation in Figure 6.18, the weights w are defined by Equation 6.2, and the sum is taken over the N channels in the ring. The oscillation in Figure 6.18 is dominated by the Y-dipole, due to the precession of the longitudinal polarization in the horizontal bends of the A-Line. However, the A-Line also has several vertical bends, incorporating a slight X-dipole oscillation into the observed distribution. Table 6.12 gives the shift to the asymmetry measured with the Møller detector

Dipole Shifts (ppb)		
	45 GeV	48 GeV
Run I	-11.7 ± 3.4	-2.9 ± 1.9
Run II	-11.3 ± 3.4	0.4 ± 2.3

Table 6.12: The computed shifts in $A^{Measured}$ due to the dipole amplitude from transverse beam polarization.

due to the dipole oscillation, computed for both Run I and Run II.

6.7.4 Spot Size Sensitivity

The detector sensitivity to beam spot size is quantified by measuring the correlation with the wire array, as described in Section 3.4. For both Run I and Run II, the systematic shift to $A^{Measured}$ due to the spot size asymmetry was found to be consistent with zero. A systematic uncertainty of 1 ppb is assigned to the possible systematic effect, with no correction made.

6.7.5 Pion Background

The pion detector (Section 4.4) is used to estimate the asymmetry and dilution factor due to pions interacting in the Møller detector. The Run I result was found to be contaminated by particles passing through the eP detector portion of the E158 calorimeter. In Run II, the insertable eP collimator blocked this background, making the pion detector result viable. The Run II result will be used for both Run I and Run II. The measured dilution factor f is 0.0014 ± 0.0011 ppb, with an asymmetry correction fA of -0.5 ± 0.8 ppb.

6.7.6 Synchrotron Radiation

The synchrotron light monitor (SLM) is used to determine the vertical polarization of the electron beam (Section 4.5). The vertical polarization, in turn, induces a helicity-dependent

Diluted Synchrotron Asymmetry (ppb)		
	45 GeV	48 GeV
Run I	-1.6 ± 1.2	1.5 ± 1.2
Run II	-1.6 ± 1.2	2.8 ± 2.2

Table 6.13: Synchrotron correction calculated with the SLM.

asymmetry in the synchrotron radiation produced in the E158 spectrometer chicane. The radiation produces a dilution factor f of 0.0015 ± 0.0005 for both Run I and Run II. The radiation also represents an asymmetry correction, shown in Table 6.13.

An alternative analysis computes the vertical polarization of the beam through observing the amplitude of the X-dipole oscillation in the plot of asymmetry versus azimuth in the Møller detector. The oscillation is due to the two photon exchange box diagram, discussed in Section 6.7.3. The method has the advantage that it computes the vertical polarization at the target, whereas the SLM is located in the middle of the A-Line bend. This analysis finds that the asymmetry contribution fA in Run I is 0.0 ± 4.5 ppb, and 0.0 ± 2.3 ppb in Run II. The results are consistent with the SLM analysis, and they are used in the calculation of A^{PV}.

6.7.7 Neutral Backgrounds

Neutral hadrons produced in the E158 calorimeter can penetrate the lead shielding of the PMTs in the detector and produce a signal by directly impacting the photocathodes. Contamination from hadrons produced in the eP detector that make it into the Møller PMTs must be quantified, due to their large asymmetry.

Data was taken with PMTs blinded with aluminum tape, so that they were only sensitive to neutral backgrounds. By comparing data with the quadrupole magnets off and with the insertable eP collimator in place or removed, it was determined that the neutral hadron background from the eP detector represents a dilution factor of 0.003 ± 0.001

for the Møller detector. The asymmetry correction is just the dilution multiplied by the asymmetry measured in the eP detector, yielding -5 ppb ± 3 ppb, with the uncertainty set conservatively [78]. The background is only important for Run I, because it is greatly suppressed in Run II by the eP collimator.

A second neutral background of concern is high-energy photons that bounce from spectrometer collimators into the Møller detector. Data taken with the spectrometer quadrupole magnets off determine that this background represents a dilution factor of 0.004 ± 0.002 [79].

The quadrupoles-off runs also found a large asymmetry in the Møller detector of 2.5 ppm. The most likely cause is electron-Aluminum scattering in the beam pipe. Simulations indicate that the effect is reduced by a factor of three when the quadrupole magnets are on. Assuming a worst-case scenario, where the entire dilution factor of 0.004 is due to this type of background, the asymmetry correction is 2.5 ppm $\times$ 0.3 $\times$ 0.004 = 3 ppb. Due to the large uncertainty in this analysis, a 100% uncertainty is applied to the correction.

6.7.8 Scale Factors

The beam polarization directly scales $A^{Measured}$ into A^{PV}. The polarization was determined with the polarimeter (Section 4.2.4) to be 84.9% ± 4.6% in Run I and 84.4% ± 4.6% in Run II.

Section 5.10.1 demonstrates that the detector linearity will also directly scale the measured value of A^{PV}. The linearity of the Møller detector is found by weighting the linearity of the In and Mid rings (Section 4.1.4) by their statistical power, yielding an overall linearity of 99.0% ± 1.1%, in both runs.

Run I Dilutions and Corrections								
	45 GeV				48 GeV			
	fA	σfA	f	σf	fA	σfA	f	σf
Beam 1st Order	0.0	1.2	0.0000	0.0000	0.0	1.2	0.0000	0.0000
Beam 2nd Order	0.0	10.0	0.0000	0.0000	0.0	10.0	0.0000	0.0000
Dipole Bias	-11.7	3.4	0.0000	0.0000	-2.9	1.9	0.0000	0.0000
eP Correction	-32.7	5.0	0.0795	0.0087	-34.5	5.4	0.0707	0.0077
Spot size	0.0	1.0	0.0000	0.0000	0.0	1.0	0.0000	0.0000
Synchrotron	0.0	4.5	0.0015	0.0005	0.0	4.5	0.0015	0.0005
High-Energy Photons	3.0	3.0	0.0040	0.0020	3.0	3.0	0.0040	0.0020
Neutral eP Leakage	-5.0	3.0	0.0030	0.0010	-5.0	3.0	0.0030	0.0010
Pions	-0.5	0.8	0.0014	0.0011	-0.5	0.8	0.0014	0.0011
Total	-46.9	13.3	0.0894	0.0090	-39.9	13.2	0.0806	0.0081
Scale Factors								
Beam Polarization 0.849 ± 0.046								
Detector Linearity 0.990 ± 0.011								

Table 6.14: The dilution factors f are dimensionless, while the asymmetry corrections fA are given in units of ppb.

6.8 Determination of A^{PV}

The results presented in Sections 6.7.1 to 6.7.8 are used with Equation 6.15 to obtain A^{PV} from $A^{Measured}$. Tables 6.14 and 6.15 contain all of the dilution factors and asymmetry corrections applied in Run I and Run II respectively. Table 6.16 presents the experimentally measured value of A^{PV} at a Q^2 of 0.026 (GeV/c)^2, the primary result of the E158 experiment. The final chapter converts A^{PV} into $\sin^2\theta_W$ for comparison to theory, and uses it to set limits on new physics phenomena.

6.9 Luminosity Monitor Results

The data from the luminosity monitor (Chapter 5) is analyzed in much the same way as the Møller detector [81]. The expected asymmetry in the lumi signal flux is -15 ppb ± 5 ppb, an order of magnitude smaller than A^{PV}. The detector serves as a sensitive null-asymmetry cross-check for the results of the Møller detector. The data presented in this section is

Run II Dilutions and Corrections								
	45 GeV				48 GeV			
	fA	σfA	f	σf	fA	σfA	f	σf
Beam 1st Order	0.0	3.0	0.0000	0.0000	0.0	2.2	0.0000	0.0000
Beam 2nd Order	0.0	15.0	0.0000	0.0000	0.0	15.0	0.0000	0.0000
Dipole Bias	-11.3	3.4	0.0000	0.0000	0.4	2.3	0.0000	0.0000
eP Correction	-27.7	4.1	0.0648	0.0078	-29.7	4.1	0.0707	0.0077
Spot size	0.0	1.0	0.0000	0.0000	0.0	1.0	0.0000	0.0000
Synchrotron	0.0	2.3	0.0015	0.0005	0.0	2.3	0.0015	0.0005
High-Energy Photons	3.0	3.0	0.0040	0.0020	3.0	3.0	0.0040	0.0020
Neutral eP Leakage	0.0	0.0	0.0000	0.0000	0.0	0.0	0.0030	0.0010
Pions	-0.5	0.8	0.0014	0.0011	-0.5	0.8	0.0014	0.0011
Total	-36.5	16.7	0.0717	0.0082	-26.8	16.5	0.0691	0.0067
Scale Factors								
Beam Polarization 0.844 ± 0.046								
Detector Linearity 0.990 ± 0.011								

Table 6.15: The dilution factors f are dimensionless, while the asymmetry corrections fA are given in units of ppb.

A^{PV} (ppb)	
Run I 45 GeV	-183 ± 38(stat) ± 20(sys)
Run I 48 GeV	-158 ± 48(stat) ± 19(sys)
Run I Combined	-173 ± 30(stat) ± 20(sys)
Run II 45 GeV	-159 ± 44(stat) ± 23(sys)
Run II 48 GeV	-131 ± 37(stat) ± 22(sys)
Run II Combined	-143 ± 28(stat) ± 23(sys)
TOTAL	**-158 ± 21 (stat) ± 17 (sys)**

Table 6.16: The parity-violating asymmetry in Møller scattering.

Run 1	Detector		
Coefficient	Channel 00	Channel 02	Full Lumi
Q (ppm/ppm)	-0.55	-0.80	-0.03
E (ppm/MeV)	-20.9	-95.7	-5.1
X (ppm/μm)	-7.9	55.3	-1.1
Y (ppm/μm)	-25.2	-4.1	0.4
dX (ppm/μR)	-389.8	1459.5	25.2
dY (ppm/μR)	-392.8	697.6	-12.9

Table 6.17: Comparison of the regression coefficients for two individual lumi channels and the full detector. Channel 00 is at the top of the lumi ring, while channel 02 is on the right side.

for the front lumi ring only, for simplicity. The back ring has poorer resolution, and is consistent with the front ring in all cases.

The lumi channels are identical ion chambers, which are automatically gain matched. The sensitivity of the detector to beam parameters is greatly suppressed when the channels are added with equal weight, in contrast to the Møller detector in Equation 6.2. The lumi asymmetry A^{Raw} is the average of the individual channel asymmetries A_i, given by

$$A^{Raw} = \frac{1}{8}\sum_{i=1}^{8} A_i. \tag{6.33}$$

The sensitivity suppression is clear in Table 6.17, which compares the regression coefficients for two individual lumi chambers with the coefficients for the whole detector.

Table 6.1 illustrates that the lumi has sensitivity more like the Møller detector than the Out ring, except for the conspicuous exception of the Q coefficient. The inflated Q coefficient again indicates that not all beam parameters are being completely regressed for the lumi. Figures 6.19 and 6.20 plot the lumi asymmetry data for Run I and Run II. The χ^2/ndf is elevated in Run I and very large in Run II, similar to the behavior of the Out ring.

Because the lumi asymmetry is expected to be essentially zero, the mean of the system-

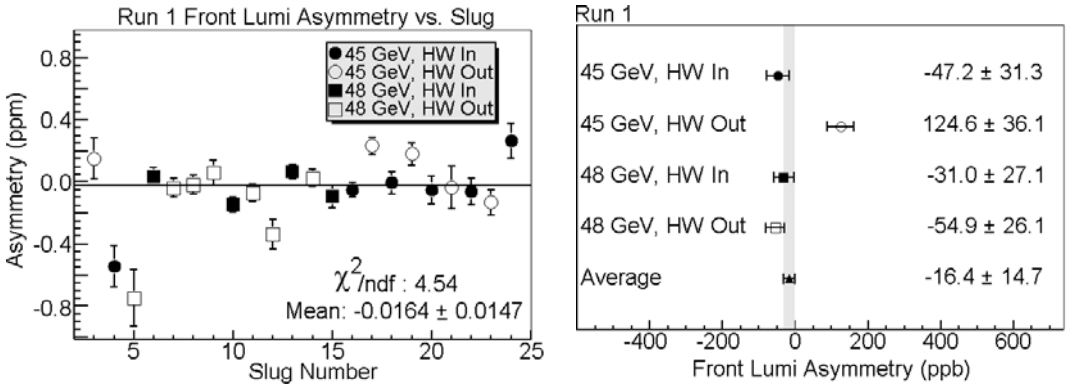

Figure 6.19: Run I lumi asymmetry data.

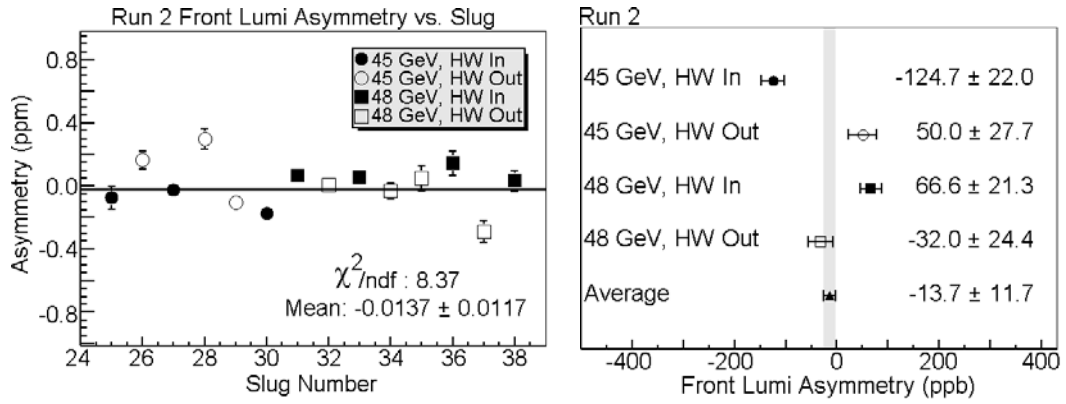

Figure 6.20: Run II lumi asymmetry data.

atic reversal plots, with the sign flips suppressed, is indicative of the size of the underlying systematic effect (Figure 6.21). The Run II reversal plot indicates that the unregressed systematic effect is at the level of 70 ppb. The effect is much smaller in Run I, most likely due to the higher frequency of systematic reversals in the Run I data set.

6.9.1 Lumi Beam Correction Systematic Uncertainty

It is clear from the systematic reversal plots that higher-order beam correction systematic uncertainties are potentially important for the luminosity monitor, though systematic reversals appear to have provided a large suppression factor. Unfortunately, because the lumi and Out ring both have large Q coefficients, the systematic uncertainty estimation methods

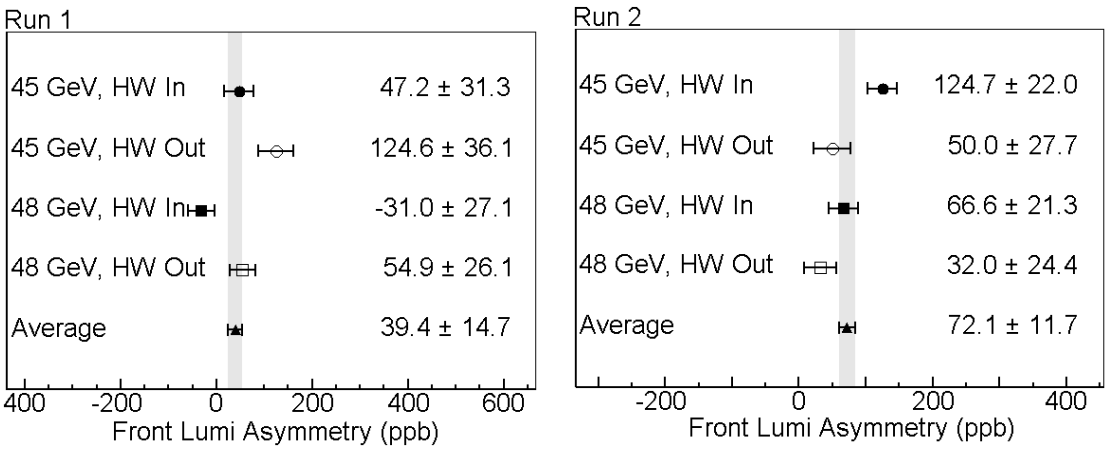

Figure 6.21: Run I and Run II lumi asymmetry with systematic reversal sign flips ignored.

outlined for the Møller detector in Section 6.7.2.2 do not have enough statistical power to set useful limits.

The systematic uncertainty estimate for the beam corrections to the lumi is found through a less direct manner. First, "composite detectors" are defined by combining weighting schemes of various detectors A_i to produce a composite detector C_n that is sensitive to beam parameter n, while insensitive to all others, through

$$C_n = \sum_{i=1}^{N} w_i A_i, \tag{6.34}$$

where the sum is taken over the N detectors used, and the weights w_i are chosen to enhance the sensitivity of the composite monitor to a single beam parameter [80]. Table 6.18 presents a simple example of the enhanced sensitivities of a composite monitor[4]: the Out-Mid combination has an enhanced sensitivity to energy fluctuations compared to the Out or Mid detector alone.

More complicated composite monitors can be constructed to precisely isolate the sen-

[4]The angle parameters have been converted from nRadians to nm to make their relative size with the other beam parameters more clear.

Coefficient Comparison			
Parameter	Mid	Out	Out - Mid
E (ppm/MeV)	-26.6	76.2	102.8
X (ppm/μm)	0.5	6.8	6.3
Y (ppm/μm)	-0.1	2.0	2.1
dX (ppm/μm)	-1.7	3.2	4.9
dY (ppm/μm)	0.6	1.6	2.2

Table 6.18: The composite monitor Out-Mid has enhanced energy sensitivity.

Composite Monitor Coefficients					
	ppb/keV	ppb/nm			
Composite	E	X	Y	dX	dY
C_E	102.3	-0.1	-0.1	0.0	0.0
C_X	-0.1	-22.0	0.0	-0.6	0.4
C_Y	0.0	-0.1	-22.6	0.0	0.0
C_{dX}	-0.1	0.0	0.6	24.1	0.0
C_{dY}	-0.1	-0.1	0.7	0.0	-34.2

Table 6.19: Regression coefficients of the composite monitors C_n.

sitivity to one beam parameter. The composite monitors are made up of combinations of the front lumi, the In, Mid, and Out rings of the Møller detector, and the X and Y dipole weighting scheme for each detector. It is expected that the unregressed systematic effects will be greatly enhanced in the composite monitors.

Table 6.19 details the composite sensitivities achieved with this method. The composite monitors C_n are each composed of roughly seven of the original detectors. The In, Mid, and Out ring are always added in a way to ensure that the physics asymmetry A^{PV} cancels between them, leaving only the difference in the eP corrections.

The asymmetry measured with each composite monitor is calculated and compared to the expected value. The expectation can be non-zero, due to differences in the eP corrections of the Møller detector regions, and the vertical polarization of the beam can induce real dipole asymmetries. The systematic uncertainty δ_n assigned to the regression correction of

Run I Front Lumi Systematic Uncertainty Estimates					
Parameter	Δ	c_{Comp}	c_{lumi}	suppression α	systematic error (ppb)
E	92.3 ± 50.1	102.3	-5.1	-0.050	-4.6 ± 2.5
X	-55.8 ± 26.5	-22.0	-1.1	0.050	-2.8 ± 1.3
Y	-139.2 ± 53.9	-22.6	0.4	-0.018	2.5 ± 1.0
dX	18.2 ± 60.2	24.1	0.6	0.025	0.5 ± 1.5
dY	117.5 ± 70.9	-34.2	-0.3	0.009	1.0 ± 0.6
					TOTAL: -3.4 ± 6.9

Table 6.20: Run I systematic uncertainty estimates for the front lumi. The columns labeled c_{Comp} and c_{lumi} contain the dominant regression coefficient for the composite monitor and the lumi, respectively.

Run II Front Lumi Systematic Uncertainty Estimates					
Parameter	Δ	c_{Comp}	c_{lumi}	suppression	systematic error (ppb)
E	120.8 ± 44.6	67.4	-5.8	-0.086	-10.4 ± 3.8
X	63.8 ± 21.0	-14.6	-1.4	0.096	6.1 ± 2.0
Y	-46.7 ± 41.6	-22.4	-0.8	0.036	-1.7 ± 1.5
dX	123.0 ± 60.2	25.2	2.9	0.115	14.2 ± 6.9
dY	135.2 ± 75.8	-33.4	0.6	-0.018	-2.4 ± 1.4
					TOTAL: 5.8 ± 15.6

Table 6.21: Run II systematic uncertainty estimates for the front lumi. The columns labeled c_{Comp} and c_{lumi} contain the dominant regression coefficient for the composite monitor and the lumi, respectively.

the n^{th} parameter for the lumi is then

$$\delta_n = \alpha_n(C_n^{Measured} - C_n^{Expected}) \rightarrow \alpha_n \Delta_n. \tag{6.35}$$

The coefficient α_n is the ratio of the the n^{th} lumi regression coefficient to the sensitive coefficient of the composite monitor C_n. The ratio expresses the relative sensitivity of the lumi monitor to the composite monitor for beam parameter n. Table 6.20 and Table 6.21 relate the systematic uncertainties calculated for the lumi in this manner for Run I and Run II. The total systematic uncertainty is found by combining the individual systematic uncertainties and errors linearly, to be conservative.

The uncertainty assigned for beam corrections for the front lumi is 7 ppb in Run I and

16 ppb in Run II. The uncertainty is still quite small compared to the variations observed in Figure 6.21. It is clear that the energy and halfwave plate systematic reversals provided large cancellation of the unregressed systematic effect and were critical for the lumi result.

6.9.2 Lumi Dipole Contamination

Unlike the Møller detector, the lumi channels are not weighted in forming the asymmetry of the whole detector, so the dipole contamination shifts in Equation 6.31 and Equation 6.32 from the Møller detector analysis in Section 6.7.3 are identically zero. However, since the lumi is not necessarily aligned with the center of the Møller detector, and hence the beam path, a large position offset at the lumi could still induce a dipole shift. Figure 6.22 displays the individual channel asymmetries for the lumi in Run I. There is no indication of any large offset, since the sinusoid fits well. Therefore, no systematic uncertainty will be assigned to the lumi for this effect.

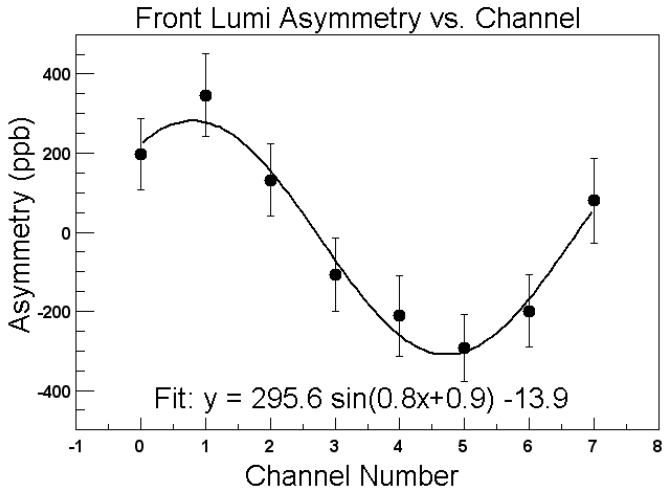

Figure 6.22: Run I lumi asymmetry plotted versus channel number.

6.9.3 Lumi Dilutions and Scale Factors

The measured lumi asymmetry must be corrected for backgrounds and uncertainties through Equation 6.15. The only background for the lumi comes from synchrotron radiation. In Section 5.9, the synchrotron dilution factor f, averaging over the whole detector, is found to be 0.0035 ± 0.0004. The uncertainty is set by the target-out signal seen in the vertical chambers.

The asymmetry correction for the synchrotron background would require a detailed simulation of the lumi to determine its analyzing power for vertical polarization. This analysis is underway, but is not yet completed. However, the result is expected to be very similar to the Møller detector result, so the Møller detector value is taken as an estimate, scaled by the ratio of the dilution factors for the two detectors. In Run I, the synchrotron asymmetry correction is 0.0 ± 10.5 ppb, and in Run II it is 0.0 ± 5.4 ppb.

The only additional asymmetry correction is due to sensitivity to the beam spot size. The spot size systematic was found to be ± 1 ppb for Run I and ± 2 ppb for Run II in Section 3.4.

The lumi has the same two scale factors as the Møller detector: beam polarization and detector linearity. The linearity used is $99 \pm 2\%$, based on the results of Section 5.10.

6.10 Lumi Asymmetry Result

Combining the corrections and systematic uncertainties of Sections 6.9.1 and 6.9.3 with the measured asymmetries in Section 6.9 yields the final luminosity monitor asymmetry. Table 6.22 presents the lumi results. Both the Run I and Run II data are consistent with the predicted value of -15 ppb $\pm$ 5 ppb. The result is a consistency cross-check for the

Luminosity Monitor Asymmetry Results	
Run I	-23.3 ppb ± 17.7 ppb (stat) ± 16.0 ppb (sys)
Run II	-20.1 ppb ± 14.1 ppb (stat) ± 20.8 ppb (sys)
Total	-21.8 ppb ± 11.5 ppb (stat) ± 18.3 ppb (sys)

Table 6.22: Luminosity monitor asymmetry results.

asymmetry measured with the Møller detector.

Chapter 7

The Weak Mixing Angle

This chapter presents the result for $\sin^2\theta_W$ calculated from the SLAC E158 measurement of the parity-violating asymmetry A^{PV} in Møller scattering. The result is then used to set limits on possible extensions to the Standard Model. Finally, future experiments planned to measure the running of $\sin^2\theta_W$ are discussed.

7.1 Extraction of $\sin^2\theta_W$

The QED calculation of A^{PV} is covered in Chapter 2. Using the convention for $\sin^2\theta_W^{eff}$ given in Equation 2.14, the asymmetry is given by

$$A^{PV} = \frac{-G_\mu Q^2}{\sqrt{2}\pi\alpha}\frac{1-y}{1+y^4+(1-y)^4}\mathcal{F}_b(y)(1-4\sin^2\theta_W^{eff}), \tag{7.1}$$

where y is related to the center-of momentum scattering angle θ_{CM} through

$$y = \frac{1-\cos\theta_{CM}}{2}. \tag{7.2}$$

The scale factor $\mathcal{F}_b(y)$ is included to account for bremsstrahlung effects that depend on the geometry of the experiment [82]. The relevant diagrams are depicted in Figure 7.1.

Bremsstrahlung radiation before scattering effectively lowers the beam energy, while radiating afterward affects the experimental acceptance. The overall effect of $\mathcal{F}_b$ was determined to be small, with an average value of 1.01 ± 0.01.

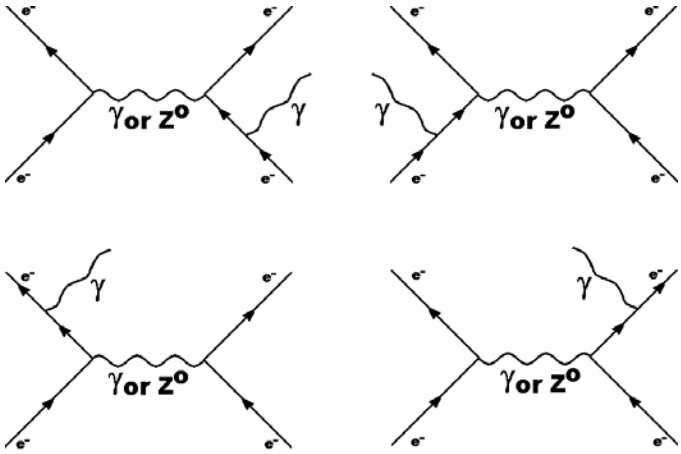

Figure 7.1: Bremsstrahlung diagrams included in $\mathcal{F}_b(y)$. The crossed versions must also be computed, for a total of 16 diagrams.

The analyzing power $\mathcal{AP}$ is defined as the flux weighted average over the kinematic factors in Equation 7.1 so that

$$A^{PV} = \mathcal{AP}(1 - 4\sin^2\theta_W^{eff}). \tag{7.3}$$

The analyzing power is computed using the same Monte-Carlo simulation that was employed for background subtraction in Section 6.7.1. Table 7.1 presents the computed values for $\mathcal{AP}$, where In and Mid refer to particular regions of the Møller detector (Section 4.1). The uncertainty on $\mathcal{AP}$ was found by varying the parameters of the simulation within reasonable bounds. The simulation was also used to determine that the average Q^2 is 0.026 $(\mathrm{GeV/c})^2$.

Analyzing Power (ppm)		
Run I	45 GeV	48 GeV
In	-2.976 ± 0.060	-3.171 ± 0.060
Mid	-3.304 ± 0.053	-3.539 ± 0.042
Run II	45 GeV	48 GeV
In	-3.046 ± 0.061	-3.182 ± 0.060
Mid	-3.372 ± 0.044	-3.537 ± 0.042
Average: -3.298 ± 0.051		

Table 7.1: Analyzing powers computed from simulation. The overall average $\mathcal{AP}$ is determined by weighting the entries with the corresponding uncertainty on A^{PV}.

Combining the average analyzing power from Table 7.1,

$$-3.298 \text{ ppm} \pm 0.051 \text{ ppm}, \tag{7.4}$$

and the measured value of A^{PV} from Table 6.16,

$$-158 \text{ ppb} \pm 21 \text{ ppb (stat)} \pm 17 \text{ ppb (sys)}, \tag{7.5}$$

the weak mixing angle is found to be

$$\sin^{\mathbf{2}} \theta_{\mathbf{W}}^{\mathbf{eff}} = \mathbf{0.2380 \pm 0.0016} \text{ (stat)} \pm \mathbf{0.0013} \text{ (sys)}. \tag{7.6}$$

For comparison, the theoretical prediction is

$$\sin^2 \theta_W^{eff} = 0.2385 \pm 0.0006 \text{ (theory)}. \tag{7.7}$$

It is clear that the agreement between the experimentally measured value and the theoretical

prediction is quite good. The difference between them is

$$\Delta \sin^2 \theta_W^{eff} = -0.0005 \pm 0.0021, \tag{7.8}$$

corresponding to ≈ 0.25 standard deviations.

Equivalently, using the convention for $\sin^2\theta_W(Q^2)$ preferred by theorists (Equation 2.13), the E158 result is

$$\sin^2 \theta_W^{\overline{MS}} = 0.2376 \pm 0.0020. \tag{7.9}$$

Figure 7.2 presents the E158 value for $\sin^2\theta_W^{\overline{MS}}$ on a plot along with the theoretically predicted Q^2 dependence. Figure 7.3 presents the measurements of the weak mixing angle evolved to the Z^0 mass, assuming the Standard Model, to aid in the comparison.

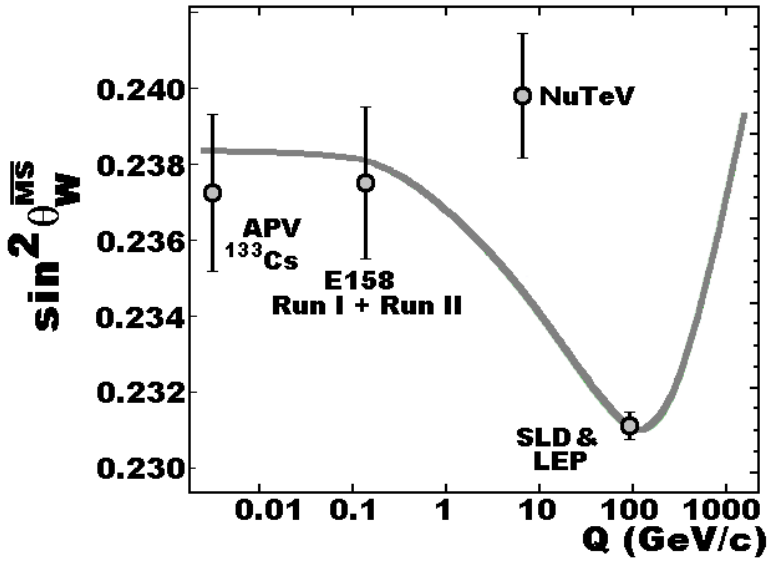

Figure 7.2: Experimental results and the theoretical running of the weak mixing angle.

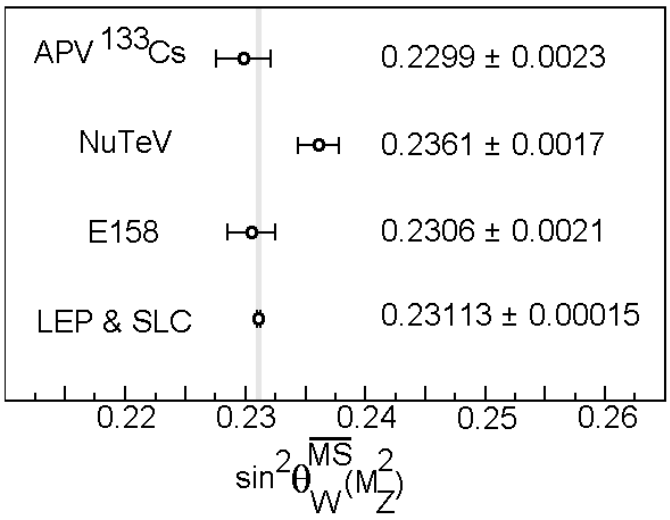

Figure 7.3: The measured weak mixing angle evolved to the Z^0 mass.

7.2 Physics beyond the Standard Model

The deviation of the measured value of $\sin^2\theta_W^{eff}$ from the theoretical predication can be used to set limits on possible extensions of the Standard Model. The following sections use the deviation in Equation 7.8 to set the E158 constraints on new physics.

7.2.1 Electron Compositeness Limit

In the current model of particle physics, the electron is assumed to be a truly point-like particle. However, it is possible that the electron has substructure [83]. In electron-electron scattering, electron compositeness can be cast as a contact interaction, with the general Lagrangian given as

$$\mathcal{L} = \frac{4\pi}{2\Lambda^2}[\eta_{LL}\overline{\psi}_L\gamma_\mu\psi_L\overline{\psi}_L\gamma^\mu\psi_L + \eta_{RR}\overline{\psi}_R\gamma_\mu\psi_R\overline{\psi}_R\gamma^\mu\psi_R + 2\eta_{RL}\overline{\psi}_R\gamma_\mu\psi_R\overline{\psi}_L\gamma^\mu\psi_L]. \quad (7.10)$$

The Λ term parameterizes the energy scale at which the contact interaction becomes important. The indices L and R refer to the chiral components of the interaction, signifying

left or right helicity. The η coefficients are free parameters, with the constraint that the largest member have a magnitude of unity or less. There are no symmetry requirements that the interaction should conserve parity, so the η values are independent.

The Lagrangian produces an amplitude that is purely real, and at low Q^2 there is an interference term with the dominant electromagnetic diagrams. In contrast, at the Z^0 resonance where the dominant amplitude is purely imaginary, no interference term results. Low energy experiments are therefore inherently more sensitive to new physics in the form of Equation 7.10 than the Z^0 pole experiments.

The process described by Equation 7.10 produces a shift in the predicted value of $\sin^2\theta_W$ given by

$$\Delta \sin^2 \theta_W^{eff} = \frac{\pi}{\sqrt{2}G_F}\frac{\eta_{LL} - \eta_{RR}}{\Lambda^2}. \tag{7.11}$$

For parity-violation experiments, it is conventional to set η_{LL} to ± 1 and η_{RR} to zero to obtain limits on $\Lambda^{\pm}_{LL}$. The E158 compositeness constraints are then

$$\Lambda^{+}_{LL} > 8.0 \ \ \mathrm{TeV/c^2} \tag{7.12}$$

and

$$\Lambda^{-}_{LL} > 6.9 \ \ \mathrm{TeV/c^2}, \tag{7.13}$$

at the 95% confidence level.

The present limit on this quantity is from the combined data of the Aleph, Delphi, L3, and Opal detectors at LEP [84]. They report a constraint on compositeness of

$$\Lambda^{+}_{LL} > 8.3 \ \ \mathrm{TeV/c^2} \tag{7.14}$$

and

$$\Lambda_{LL}^{-} > 10.3 \ \text{TeV/c}^2. \tag{7.15}$$

Individual results from these experiments yield constraints in the range of three to five TeV/c^2. The E158 limit is quite competitive with the collider results.

7.2.2 Scalar Doubly Charged Higgs Limit

Møller scattering is uniquely sensitive to s-channel scattering through exchange of an exotic doubly charged scalar Higgs boson. Particles such as this often appear in theories beyond the Standard Model and are not required to respect parity [85]. Figure 7.4 depicts the diagram for this process.

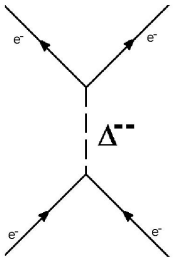

Figure 7.4: Doubly charged Higgs particle exchange diagram.

The mass of the Higgs particle is constrained to be much larger than the interaction energy, so it can be described as a contact interaction in the same formalism as the electron compositeness limit. The process would shift $\sin^2\theta_W^{eff}$ by

$$\Delta \sin^2\theta_W^{eff} = \frac{\sqrt{2}}{8}\left(\frac{g}{M_H}\right)^2 \frac{\eta_{LL} - \eta_{RR}}{G_F}, \tag{7.16}$$

where g/M_H is the ratio of the coupling to the mass of the Higgs particle. Again, η_{LL} is set to ± 1 while $\eta_{RR} = 0$ to obtain the limit on $\left(\frac{g}{M_H}\right)^2_{LL^{\pm}}$. The 95% confidence limits from

the E158 result are

$$\left(\frac{g}{M_H}\right)^2_{LL^+} < 0.017 G_F \tag{7.17}$$

and

$$\left(\frac{g}{M_H}\right)^2_{LL^-} < 0.022 G_F. \tag{7.18}$$

The current limits are set by observing the related process of muonium to anti-muonium conversion [86]. Figure 7.5 depicts the diagram for this process. These experiments place

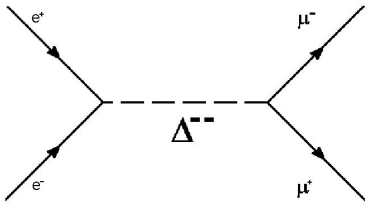

Figure 7.5: Muonium to anti-muonium conversion.

the constraint

$$\left(\frac{g}{M_H}\right)^2 < 0.14 G_F, \tag{7.19}$$

on the doubly charged Higgs parameters, at the 90% confidence level.

The E158 limit represents an order of magnitude improvement. However, it should be noted that the muonium experiments would still be sensitive even in the absence of parity violation.

7.2.3 Extra Z Boson Limit

Many extensions to the Standard Model include new heavy analogues to the Z^0. The new particle is usually denoted as a Z′. Some Grand Unified Theories embed the Standard Model in the group E_6, producing two new Z′ states [87]. The extra Z particles assume the

forms [88]

$$Z_\beta = Z_\chi \cos\beta + Z_\psi \sin\beta \tag{7.20}$$

and

$$Z_{\beta'} = -Z_\chi \sin\beta + Z_\psi \cos\beta. \tag{7.21}$$

The Z_χ state has distinct couplings to different fermions, while the Z_ψ state couples universally to all fermions [89]. The presence of these new particles scales the prediction for A^{PV} [32] by

$$1 + 7\left\{\frac{m^2_{Z^0}}{m^2_{Z_\beta}}\left(\cos^2\beta + \sqrt{\frac{5}{3}}\sin\beta\cos\beta\right) + \frac{m^2_{Z^0}}{m^2_{Z_{\beta'}}}\left(\sin^2\beta - \sqrt{\frac{5}{3}}\sin\beta\cos\beta\right)\right\}. \tag{7.22}$$

The mixing angle β is model dependent. In the SO(10) model, a group of considerable theoretical interest, $\beta = 0$ and Equation 7.22 simplifies to

$$1 + 7\frac{m^2_{Z^0}}{m^2_{Z_\chi}}. \tag{7.23}$$

The weak mixing angle would be modified as

$$1 - 4\sin^2\theta^{eff}_W \rightarrow \left(1 + 7\frac{M^2_{Z^0}}{M^2_{Z_\chi}}\right)\left(1 - 4\sin^2\theta^{eff}_W\right). \tag{7.24}$$

The E158 measurement of the weak mixing angle can then be used to set the limit on the mass of the extra Z particle of

$$M_{Z_\chi} > 410 \ \ \mathrm{GeV/c^2}, \tag{7.25}$$

at the 95% confidence level. The single highest current constraint is provided by CDF which reports $Z_\chi > 595$ GeV/c^2 at the 95% confidence level [90].

7.2.4 Oblique Parameter X Limit

Extensions to the Standard Model could be manifested through radiative corrections to the gauge boson propagators, known as oblique corrections. The standard Peskin-Takeuchi parameters STU were introduced to quantify deviations from the Standard Model due to oblique corrections for energies much greater than M_{Z^0} [91]. This formalism was extended to include new physics effects at the weak scale by the introduction of three new parameters VWX [92].

The running of $\sin^2\theta_W$ from the Z^0 resonance down to low Q^2 can be shown to isolate the X parameter [93]. The $\kappa(0)$ term in Equation 2.8 is modified as [32]

$$\kappa(0) \rightarrow (1 - 0.032X)\kappa(0). \tag{7.26}$$

The shift in $\sin^2\theta_W^{eff}$ is then

$$\Delta \sin^2\theta_W^{eff} = -\rho\kappa(0)(0.032X)\sin^2\theta_W^{\overline{MS}}(M_{Z^0}^2). \tag{7.27}$$

The quantities ρ and κ are defined in the theoretical calculation of A^{PV} in Sections 2.4.4 and Section 2.4.1. Using the E158 result, it is found that the limit on X is

$$X = 0.07 \pm 0.28. \tag{7.28}$$

The value of X based on a global $STUVWX$ fit to world data in 1994 has an uncertainty of 0.58 [94]. The inclusion of the E158 result, and to an equal degree the atomic parity violation result, will produce a substantial improvement.

7.3 Future Experiments

Several upcoming experiments will be conducted to map out the running of the weak mixing angle. Figure 7.6 depicts the proposed experiments and the expected final uncertainties. The following sections give brief descriptions of these experiments.

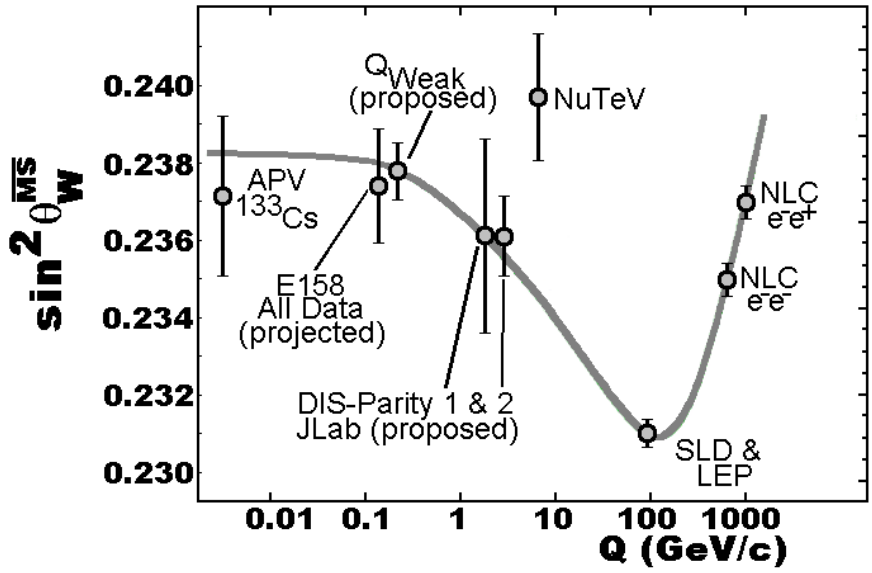

Figure 7.6: Present and future experiments used to map the running of the weak mixing angle.

7.3.1 E158 Run III

The final run of the E158 experiment, Run III, took place in the Summer of 2003. The amount of data collected was approximately equal to the sum of Run I and Run II. The addition of the Run III data is therefore expected to reduce the uncertainty on $\sin^2\theta_W$ by a factor of $\approx \sqrt{2}$. Additionally, the analysis of the "sliced" BPM signals (Section 6.7.2.2) is expected to reduce the systematic uncertainty on the Run I and Run II results. Overall, the E158 result should yield an uncertainty of approximately

$$\delta \sin^2 \theta_W^{eff} = \pm 0.0014. \tag{7.29}$$

7.3.2 Q_{Weak}

The Q_{Weak} experiment has been approved to run in Hall C at Jefferson Lab, beginning in 2007 [95]. It will operate at a Q^2 of 0.03 (GeV/c)^2, almost identical to the E158 experiment. Q_{Weak} will employ a 1.2 GeV longitudinally-polarized electron beam on a 35 cm liquid hydrogen target to observe the parity-violating asymmetry in elastic electron-proton scattering.

In the limit of a small scattering angle, the asymmetry A^{PV}_{QWeak} is given by

$$A^{PV}_{QWeak} = \frac{-G_F}{4\pi\alpha\sqrt{2}}\left[Q^2(1-4\sin^2\theta_W) + Q^4 B(Q^2)\right] \approx -300 \text{ ppb}. \tag{7.30}$$

The term $B(Q^2)$ is due to the electromagnetic and weak form factors of the proton, and contributes roughly 1/3 of the total asymmetry. It will be determined from the results of other experiments, including HAPPEX and SAMPLE.

The goal is to perform a 4% measurement of A^{PV}_{QWeak}, which would correspond to a 0.3% measurement of $\sin^2\theta_W$. The dominant sources of systematic uncertainty on A^{PV}_{QWeak} are anticipated to be a 2% uncertainty coming from the determination of $B(Q^2)$ and a 1.5% uncertainty from the beam polarization measurement.

7.3.3 DIS-Parity at JLab

The DIS-Parity experiment has been proposed to run in Hall A at Jefferson Lab [96]. The experiment will use a longitudinally-polarized electron beam on a 15 cm liquid deuterium target, to measure the parity-violating asymmetry A_{DIS} in deep-inelastic scattering. The Q^2 will be 2.0 (GeV/c)^2, placing it between the NuTeV and the E158 results. The parity-

violating asymmetry is given by

$$A_{DIS} = (109\,\mathrm{ppm})Q^2\left[\left(\frac{-3}{2}+\frac{10}{3}\sin^2\theta_W\right)+YR_v\left(\frac{-3}{2}+6\sin^2\theta_W\right)\right]\sim -100\ \mathrm{ppm}, \tag{7.31}$$

where $Y \approx 1$ contains kinematics information and $R_v \approx 1$ depends on quark distributions.

The goal of the first run of the experiment will be a determination of $\sin^2\theta_W$ to $\approx 1\%$ using a 6 GeV beam. If a large deviation from the Standard Model prediction is observed, a second run is planned that would employ the 12 GeV upgraded beam at JLab and run at a larger scattering angle [97].

7.3.4 The Large Hadron Collider

The Large Hadron Collider (LHC) at CERN is expected to become operational in 2008 [98]. It is designed to produce proton-proton collisions with an energy of 14 TeV. By observing a large number of Z^0 decays, it is expected that $\sin^2\theta_W(M^2_{Z^0})$ will be measured to a precision of $\pm$ 0.0001. Also, the large energy scale will allow for direct searches of extra Z bosons, superseding all indirect constraints. In particular, the Z_χ in the SO(10) model will be constrained at the level of 4.5 TeV, an order of magnitude improvement.

7.3.5 Next Linear Collider

The high-energy lepton-lepton collisions of the proposed "Next Linear Collider" (NLC) would be required to measure the weak mixing angle for Q^2 much larger than $M^2_{Z^0}$ [99]. If the machine is ever constructed, it is expected that collision energies in the range of 1 to 1.5 TeV will be achieved, as shown in Figure 7.6 [100].

7.4 Conclusion

The E158 result represents the first measurement of parity violation in Møller scattering. The observed value of $\sin^2\theta_W^{eff}$ at a Q^2 of 0.026 $(\mathrm{GeV/c})^2$ is in agreement with the Standard Model prediction for the running of the weak mixing angle. The success of the E158 experiment demonstrates the technical feasibility of measuring small parity-violating asymmetries, setting the stage for future challenging parity violation experiments that will further probe the Standard Model of particle physics.

Bibliography

[1] H. Becquerel, p. 52 of *Nobel Lectures, Physics 1901-1921*, (Elsevier Publishing Company, Amsterdam, 1967).

[2] J. Chadwick, Verh. d. D. Phys. Ges. **16**, 383 (1914).

[3] W. Pauli, "Letter to Tübingen Conference," Pauli Archive at CERN (1930).

[4] E. Fermi, Nuovo Cim. **11**, 1 (1934).

[5] T. D. Lee *et al.*, Phys. Rev. **75**, 905 (1949).

[6] T. D. Lee and C. N. Yang, Phys. Rev. **104**, 254 (1956).

[7] C. S. Wu *et al.*, Phys. Rev. **105**, 1413 (1957).

[8] S. L. Glashow, Nucl. Phys. **22**, 579 (1961).

[9] S. Weinberg, Phys. Rev. Lett. **19**, 1264 (1967).

[10] A. Salam, p. 367 of *Elementary Particle Theory*, (Almquist and Wiksells, Stockholm, 1969).

[11] F. J. Hasert *et al.*, Phys. Lett. **B46**, 121 (1973).

[12] C. Y. Prescott *et al.*, Phys. Lett. **B77**, 347 (1978).

[13] C. Y. Prescott *et al.*, Phys. Lett. **B84**, 524 (1979).

[14] G. Arnison *et al.*, Phys. Lett. **B122**, 103 (1983).

[15] K. Hagiwara *et al.*, Phys. Rev. **D66**, 010001 (2002).

[16] G. P. Zeller *et al.*, Phys. Rev. Lett. **88**, 091802 (2002).

[17] S. C. Bennett and C. E. Wieman, Phys. Rev. Lett. **82**, 2484 (1999).

[18] E. A. Paschos and L. Wolfenstein, Phys. Rev. **D7**, 91 (1973).

[19] G. P. Zeller *et al.*, Phys. Rev. **D65**, 111103 (2002).

[20] K.P.O. Diener *et al.*, hep-ph/0310364v1 (2003).

[21] S. A. Blundell *et al.*, Phys. Rev. **D45**, 1602 (1991).

[22] W. J. Marciano and J. L. Rosner, Phys. Rev. Lett. **65**, 2963 (1990).

[23] S. J. Pollack and M. C. Welliver, Phys. Lett. **B464**, 177 (1999).

[24] A. Derevianko, Phys. Rev. Lett. **85**, 1618 (2000).

[25] V. A. Dzuba *et al.*, Phys. Rev. **A63**, 044103 (2001).

[26] A. Derevianko, Phys. Rev. **A65**, 012106 (2001).

[27] M. G. Koslov *et al.*, Phys. Rev. Lett. **86**, 3260 (2001).

[28] V. A. Dzuba *et al.*, Phys. Rev. **D66**, 076013 (2002).

[29] M. Y. Kuchiev and V. V. Flambaum, hep-ph/0305053 (2003).

[30] E. Derman and W. J. Marciano, Annals Phys. **121**, 147 (1979).

[31] T. Kinoshita and A. Sirlin, Phys. Rev **113**, 1652 (1959).

[32] A. Czarnecki and W. J. Marciano, Phys. Rev. **D53**, 1066 (1995).

[33] W. J. Marciano and A. Sirlin, Phys. Rev. **D22**, 2695 (1980).

[34] T. B. Humensky *et al.*, "Setup of Longpulse Laser System for E158," E158 Source Document (2001).

[35] T. B. Humensky *et al.*, Nucl. Inst. Meth. **A521**, 261 (2004).

[36] T. Maruyama *et al.*, Nucl. Inst. Meth. **A492**, 199 (2002).

[37] R. Carr *et al.*, SLAC-Proposal-E-158 (1997)

[38] D. Whittum and Yu. Kolomensky, Rev. Sci. Instrum. **70**, 2300 (1999).

[39] P. Mastromarino, "Beam Asymmetry Analysis for E-158 Run 1," E158 Technote 34 (2003).

[40] M. Woodley and M. Woods, "Skew Quad SQ27.5," E158 Technote 25 (2001).

[41] J. G. Weisend *et al.*, "The Cryogenic System for the SLAC E158 Experiment," E158 Technote 11 (2001).

[42] J. Gao *et al.*, Nucl. Inst. Meth. **A498**, 90 (2003).

[43] C. G. Arroyo *et al.*, "eP Inelastic Scattering Asymmetry Correction," E158 Technote 33 (2003).

[44] M. Woods *et al.*, "Synchrotron Background Analysis for Run I," E158 Technote 39 (2003).

[45] A. E. Bondar and E. L. Saldin, Nucl. Inst. Meth. **195**, 577 (1982).

[46] I. Younus, "E158 Calorimeter," E158 Technote 47 (2003).

[47] D. Relyea, "Møller Electronics Specifications," E158 Technote 26 (2001).

[48] M. Cooke, "Probing Møller Detector Linearity with the Polarized Iron Foil and Light Filters," E158 Technote 48 (2003).

[49] H. L. B. Gould and D. H. Wenny, Elec. Eng. (Amer. Inst. Elec. Eng.) **76**, 208 (1967).

[50] C. Møller, Ann. Phys. (Leipzig) **14**, 532 (1932).

[51] N. M. Shumeiko and J. G. Suarez, J. Phys. **G26**, 113 (2000).

[52] E. Chudakov, "E158 Polarimetry, New Detector," E158 Technote (2003).

[53] E. Chudakov, "Polarimetry, Run I," E158 Technote 43 (2002).

[54] L. G. Levchuk, Nucl. Inst. Meth. **A345**, 496 (1994).

[55] C. Arroyo, "Profile Detector Analysis of E158 Run," E158 Technote 19 (2001).

[56] D. L'huillier, "Pion Detector Analysis," E158 Technote 42 (2003).

[57] D. L'huillier, GEANT3 simulation for E158 (unpublished) (2002).

[58] B. T. Tonguc and M. Woods, "Report on Synchrotron Radiation Analysis," E158 Technote 17 (2001).

[59] S. A. Belomesthnykh, Nucl. Inst. Meth. **227**, 173 (1984).

[60] B. Tweedie, "The GEANT3 Simulation of E158," E158 Technote 37 (2003).

[61] L. Keller, "LUMI Asymmetry and Acceptance as a Function of Transverse and Angular Displacement at the Target," E158 Technote 28 (2001).

[62] C. Arroyo, "Data/Simulation Comparison of Cherenkov Detector Scans for Run I," E158 Technote 41 (2003).

[63] D. Relyea, GEANT Simulation for E158 (unpublished) (2001).

[64] C. Field, EGS4 Simulation for E158 (unpublished) (2001).

[65] J. D. Jackson, Rev. Mod. Physics **48**, 417 (1976).

[66] I. P. Karabekov and R. Rossmanith (Jefferson Lab), CEBAF-PR-93-014 (1993).

[67] A. V. Zarubin, Nucl. Inst. Meth. **A283**, 409 (1900).

[68] P. Bosted, "Radiative Corrections for E158," E158 Technote 23 (2003).

[69] D. Relyea, "Run I Asymmetry Analysis," E158 Technote 53 (2003).

[70] G. M. Jones, "E158 Run I Luminosity Monitor Asymmetry Analysis," E158 Technote 38 (2003).

[71] K. Bega, "Run II: Summary of Møller Unblinded Results," E158 Technote 52 (2002).

[72] A. Vacheret, "Run III Higher Orders Systematic Studies," E158 Technote 59 (2003).

[73] J. Farrell, "Characterization of the E158 Beam," E158 Technote 57 (2003).

[74] J. T. Seeman, "Linear Collider Accelerator Physics Issues Regarding Alignment," p. 257 of *Stanford 1989 Accelerator Alignment Proceedings*, (1989).

[75] P. Bosted, "Predicted Dithering Response for E158," E158 Technote 49 (2003).

[76] Y. Kolomensky, "Higher Order Asymmetry Systematics," E158 Technote 56 (2003).

[77] L. Dixon and M. Schreiber, hep-ph/0402221 (2004).

[78] L. Kaufman and K. Kumar, "Neutral Backgrounds in the Møller Detector," E158 Technote 44 (2003).

[79] K. Kumar, "Update on Neutral Backgrounds," E158 Technote 55 (2003).

[80] M. Woods *et al.*, "Run I Systematic Error for Beam Asymmetry Corrections," E158 Technote 45 (2003).

[81] G. M. Jones, "Lumi Asymmetry Analysis, All Data Runs," E158 Technote 54 (2003).

[82] V. A. Zykunov, Yad. Phys. **66** (2003).

[83] E. J. Eichten *et al.*, Phys. Rev. Lett **50**, 811 (1983).

[84] K. Hagiwara *et al.*, Phys. Rev. **D66**, 010001 (2002).

[85] N. G. Deshpande *et al.*, Phys. Rev. **D44**, 837 (1991).

[86] V. A. Gordeev *et al.*, Physics of Atomic Nuclei **60**, 1164 (1997).

[87] D. London and J. Rosner, Phys. Rev. **D34**, 1530 (1986).

[88] W. J. Marciano, "Spin and Precision Electroweak Physics," *Proceedings of the 21st SLAC Summer Institute*, (1993).

[89] P. Langacker *et al.*, Phys. Rev. **D30**, 1470 (1984).

[90] F. Abe *et al.* (CDF Collaboration), Phys. Rev. Lett **79**, 2192 (1997).

[91] M. E. Peskin and T. Takeuchi, Phys. Rev. **D46**, 381 (1991).

[92] I. Maksymyk *et al.*, Phys. Rev. **D50**, 529 (1993).

[93] A. Kundu and P. Roy, Int. J. Mod. Phys. **A12**, 1511 (1997).

[94] C. P. Burgess *et al.*, Phys. Lett. **B326**, 276 (1994).

[95] D. S. Armstrong *et al.*, hep-ex/0308049 (2003).

[96] J. Arrington *et al.*, "Parity Violating Deep Inelastic Scattering at CEBAF 6 GeV, Letter of Intent to Jefferson Lab PAC-24," Jefferson Lab internal document (2003).

[97] J. Arrington *et al.*, "Hall A 12 GeV Upgrade Pre-Conceptual Design Report," Jefferson Lab internal document (2003).

[98] G. Azuelos *et al.*, hep-ph/0003275 (1999).

[99] A. Czarnecki and W. J. Marciano, Int. J. Mod. Phys. **A15**, 2365 (2000).

[100] S. Kuhlman *et al.*, "Physics and Technology of the Next Linear Collider," hep-ex9605011 (1996).